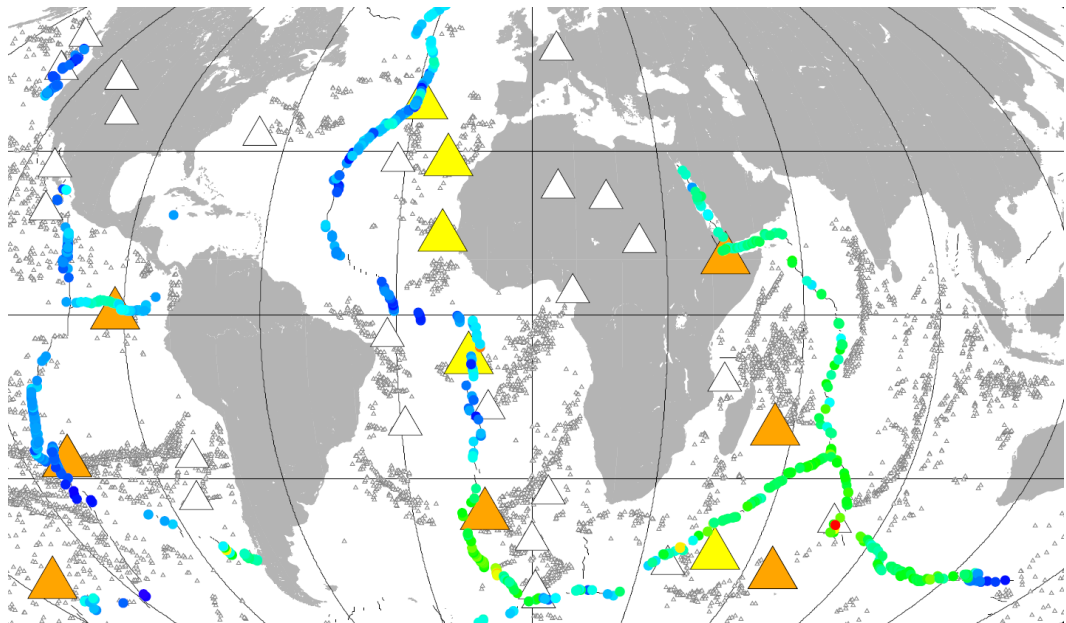**Master Thesis, Department of Geosciences**

Global geochemical variation of mid-ocean ridge basalts

Hermann Drescher

UNIVERSITY OF OSLO

FACULTY OF MATHEMATICS AND NATURAL SCIENCES

Global geochemical variation of mid-ocean ridge basalts

Hermann Drescher

Master Thesis in Geosciences

Discipline: Geology

Department of Geosciences and Centre for Earth Evolution and

Dynamics

Faculty of Mathematics and Natural Sciences

University of Oslo

August 2014

Acknowledgements

Abstract

The asthenosphere beneath the global network of spreading ridges is continuously sampled by partial melting, generating mid-ocean ridge basalts (MORB). Zero-age basalts and associated abyssal peridotites along the spreading axes have been sampled and published for the past decades, generating a wealth of systematic along-along axis data sets of element abundances and isotope compositions. Published geochemical analyses of the MORB samples have been compiled for this study. The compilation also includes water depth, associated geophysical parameters and the derived crustal thickness. After moderate data filtering (mainly removal of evolved samples with <6 wt% MgO, >53 wt% SiO_2), selected major and trace element abundances and ratios, as well as various isotope ratios, have been displayed on global and regional maps, as along-axis profiles for the various ridge segments and in selected two-component variation diagrams. Because the supply of deep mantle material to the sub-ridge mantle by plumes is an important process of asthenospheric evolution, filtering of ridge areas affected by nearby plumes have not been done.

The investigations involve an assessment of the degree of partial melting (degree of "fertility" of the MORB) and the relative distribution of the main enriched (fertile) mantle components on regional and global scales. The main fertile components include the HIMU-type (high-μ, high U/Pb-ratio) component: recycled oceanic crust (ROC) and the EM1-type (EM: enriched mantle) components: lower continental crust (LCC) and subcontinental lithospheric mantle (SCLM). The geochemical MORB compositional data hardly allow an assessment of the regional and global distribution of the volumetrically minor EM2-like component, upper continental crust, introduced into and recycled through the mantle via pelagic sediments.

On a broad scale, increasing degree of partial melting is reflected by a minor increase in the fractionation-corrected Ca/Al ratio, which in turn is positively correlated with the spreading rate in the sequence from the South-West Indian Ridge (SWIR, full spreading rate < 20 mm/a) Mid-Atlantic Ridge (MAR), the Central Indian Ridge (CIR), the South-East Indian Ridge (SEIR) and the East Pacific Rise (EPR, > 80 mm/a). The crustal thickness and water depth are broadly correlated (positively and negatively, respectively) with the degree of melting (F), although limited ridge segments without oceanic crust along the ultra-slow Gakkel Ridge and the SWIR are not as deep as the Mid-Cayman Rise. In the global context, Kolbeinsey Ridge (high F) and Mid-Cayman Rise (low F) are the shallowest and deepest ridges, respectively.

Other proxies, like low La/Sm and high $^{143}Nd/^{144}Nd$ ratios characterize MORB formed by large degree of melting and or from refractory source compositions. The Sr-Nd-isotope relation is a suitable indicator for the variable proportions of refractory to fertile components in MORB. The EPR basaltic range is more restricted and with a more refractory composition than the Indian and Atlantic MORB

range. The further separation of basalts dominated by either the HIMU-type ROC component or the EM1-type LCC and SCLM components is facilitated by the Nd-Pb-isotope relations (e.g. $^{143}Nd/^{144}Nd$ versus $^{206}Pb/^{204}Pb$) and by derivative parameters like $\Delta7/4$, $\Delta8/4$ and $\Delta\varepsilon Hf$. The HIMU and EM1-type (LCC and SCLM) components are characterized by low $\Delta8/4$ and $\Delta\varepsilon Hf$and high$\Delta8/4$ and $\Delta\varepsilon Hf$, respectively (e.g. Hanan et al., 2004; Goldstein et al., 2008). Based on these relations, the restricted EPR compositions are characterized by high proportions of ROC, whereas the "DUPAL"-type composition of the Indian Ocean and the south Atlantic has a high EM1/HIMU ratio (Hart, 1984). Whereas a broad negative correlation between $^{187}Os/^{186}Os$ and $^{176}Hf/^{177}Hf$ or$^{143}Nd/^{144}Nd$ in the Indian Ocean MORB suite indicates that the Indian DUPAL signature can be largely ascribed to LCC, the situation is less clear for the south Atlantic DUPAL. Class and Le Roex (2011) suggested convective supply and mixing of the DUPAL components into the asthenosphere by the deep plumes in the south Atlantic. In contrast, the Indian Ocean DUPAL components were most likely convectively introduced by continental rifting of Pangea and the following plate movements across the current Indian Ocean domain (e.g. Escrig et al., 2002; Hanan et al., 2004; Torsvik et al., 2013). The NE Atlantic and Arctic (especially the Mohns, Knipovich and western Gakkel ridge segments) are characterized by high SCLM proportion (e.g. Goldstein et al. 2008; Salters et al. 2011). The Reykjanes Ridge and most of the MAR between 53 N and 30 S have high ROC/SCLM proportion ratio. A high proportion of SCLM, however, may be present south of the Azores, near the intersection between the MAR and the Oceanographer Fracture Zone.

The compositional difference between the asthenospheres of the Pacific and the Atlantic and Indian Oceans can mostly be ascribed to the large scale Earth structure and recent evolution. The current Pacific domain and its precursor, Panthalassa, have been mostly devoid of continents after 340 Ma, and the location above the Pacific Large Low Shear-wave Velocity Province (LLSVP) during this period (Torsvik et al. 2014) has provided a constant convective supply, largely by plumes, of deep mantle material with low EM1-contents. The current Atlantic and Indian Ocean asthenospheric domain, however, has been largely covered by continents in the same period, providing sources of convective erosion and mixing of SCLM and LCC from the continental roots.

Table of contents

1. Introduction

1.1. A brief introduction to MORB and mantle geochemistry

The mid ocean ridges (MORs) are the Earth's longest mountain chain and are present at all divergent plate boundaries. At the MORs the lithosphere that gets recycled into the mantle at the subduction zones, their plate tectonical counterparts, gets replaced with passively upwelling mantle material and undergoes partial decompression melting generating new basaltic oceanic crust visible on the surface as sea floor spreading. Due to the large amount of newly emplaced lithosphere this process is responsible for the vast majority of magmatic activity on the Earth's surface with almost the complete global volume of melt production being tied to MORs. Due to its vast geographical extent and volume mid ocean ridge basalt (MORB) generation is the most common geochemical sampling mechanism of the upper mantle.

The chemical composition of MORB can be related to geophysical features on the MORs as both are controlled by the properties of the underlying asthenospheric mantle, i.e. its temperature and chemical composition, and their derivatives such as density or mechanisms and extent of melt production. MORB geochemistry and geophysics together can therefore trace geochemical inhomogeneities in the upper mantle.

Inhomogeneity in the upper mantle is the result of a complex history of locally varying melt extraction, metasomatism and recycling accompanied by convective stirring. These processes have led to the formation and distribution of chemically, physically and isotopically distinct mantle heterogeneities ranging from sub-grain to ocean basin scale. Not only these passive heterogeneities, but also hotspots providing hot mantle material containing recycled components by locally confined upwelling, therefore have a geophysical as well as a geochemical impact on MORs and MORB generation.

Mantle geochemistry has always had the purpose to contribute to an improved understanding of evolution, dynamics and structure of the Earth's interior in cooperation with geophysics and classical field geology. This is achieved with the study of major and trace element compositions and most prominently isotope systems that reflect the chemical composition of the mantle and its differentiation history. Different elements have different affinities to minerals and liquid phases resulting in fractionation of elements into different phases. Isotope systems reflect the same mechanisms as well due to the different properties of the mother and daughter isotopes. Additionally they allow constraining the timing of events like melt extraction by assessing the ratios of radiogenic and non-radiogenic isotopes of isotope systems such as Rb-Sr, Sm-Nd, U-Pb or Th-Pb.

1.1.1. Basic terms

The terms compatible and incompatible elements refer to the elements partitioning into crystal structures relative to coexisting melts. Compatible elements are elements that have higher affinity for the crystal structure of the minerals in the mantle compared to a partial melt. Therefore, compatible elements are concentrated in residual mantle minerals, whereas incompatible elements are enriched in the extracted partial melts and consequently also in the crust.

Enrichment generally refers to an increase of incompatible elements in a geochemical reservoir (often relative to a chondritic or bulk silicate earth composition). This term is equivalent to geochemical fertility. Depletion (i.e. melt depletion) describes the opposite process of partial melting and melt extraction from a geochemical reservoir leaving a refractory residual. Recycling of crustal material, formed originally by melt extraction from the mantle, can (re-)enrich (or fertilize) depleted reservoirs.

These processes are not the only processes in the Earth´s mantle and can be overshadowed by other mechanisms. For example enrichment can be overshadowed by high degrees of melting which not only extract the most incompatible portion of the source but also the more refractory depleted parts. In this case the enriched component in the melt can be diluted significantly. Also metasomatic processes in the upper mantle can change the composition in other ways than melt extraction.

In a more specific use enrichment and depletion are used to refer to single elements which may behave differently from the incompatible elements referred to in the "unspecific" use of the term. Elements can be enriched in the residual by melt extraction (those that during melt extraction exclusively remain in the depleted source). Thus an enrichment in a certain element is not necessarily equivalent to a general enrichment.

It is also important to keep in mind that at low degrees of melting the fertile (i.e. enriched) components are preferentially sampled, because they fractionate stronger into the melt, while during higher degrees of melting more depleted components also contribute to the melt. This means partial melting of the same source with a high degree of melting will cause the melt to be less enriched than the extraction of only a small melt fraction would.

1.1.2. Inhomogeneity in the Earth's mantle

The mantle comprises 83 volume% and 67 mass% of the Earth (Dziewonski and Anderson, 1981). Insights into its structure, materials and dynamics are therefore essential for understanding the evolution of the Earth.

The range of chemical and isotopic compositions of oceanic basalts (MORB and OIB) and peridotites have been interpreted differently over time, resulting in various models for mantle evolution. Processes creating mantle heterogeneities include early- and late-stage cumulate formation during magma ocean crystallization, extraction, transport, deposition and fractional crystallization of partial melts, metasomatism of the uppermost mantle and recycling of oceanic lithosphere by subduction (Hofmann, 1997). Such lithosphere contains a sizeable proportion of basaltic ocean crust and minor amounts of pelagic sediments, which have sampled the average upper continental crust. The subducted material is variably processed by fluid extraction in the Benioff zones, where large-ion lithophile elements (LILE) and base metals are largely removed, whereas the high field-strength elements HFSE are mostly retained in the subducted slab. Also sub-continental mantle lithosphere (SCLM) and even lower continental crust (LCC) may be detached or tectonically eroded and recycled into the mantle if they are sufficiently dense. These components seem to be identifiable in basalts derived from mantle plumes, as well as from the asthenospheric sources of MORB. The common long-term stability of deep continental roots in relatively cool mantle regions enables multi-stage metasomatism by carbonatitic or kimberlitic melts and hydrous fluids to influence the composition of SCLM before detachment and recycling.

The mantle is heterogeneous on all scales from sub-grain to global scale. At sub-grain scale mineral zonation occurs in crystals with low diffusion rates. On the grain scale refractory OsIr alloy nuggets and sulphides, that potentially carry low μ signatures, are present as inclusions and interstitial grains. Isotopic heterogeneity on mineral grain scale has implications on the isotopic equilibrium between oceanic basalts and their source, respectively the residue as it is the case with especially Os isotopes of MORB, which are not in equilibrium with the source peridotite due to the incompatibility of Os in silicate phases (Burton et al., 2000; Hofmann, 2003; Burton et al., 2012). On a scale from few cm to 10m fertile veins formed by melt percolaton or metasomatism can be found, while on the next bigger scale of ca. 10 to 100m fertile streaks and bands as well as lenses or pods related to potentially basaltic recycled oceanic material (ROC) occur. Inhomogeneity at this intermediate scale such as the "marble-cake" mantle structure proposed by Allègre and Turcotte (1986) was difficult to prove until in later studies it was shown that mantle heterogeneities are the most viable way to explain the extreme variations in isotopic and REE compositions of melt inclusions (Sobolev et al., 2000) as well as by the occurrence of plume basalts with MORB like characteristics in Hawaii, Iceland and few other places (Regelous et al., 2002). Presumably large dense reservoirs at the bottom of the mantle that are

potentially composed of basaltic or Fe-rich peridotitic composition occur in sizes up to the two LLSVPs. Other large scale heterogeneities in the lower mantle are the ULVZs, which are possibly partially molten and rich in ROC (Andrault et al., 2014). Large strongly depleted refractory peridotitic domains with high viscosity are potentially present in all parts of the mantle as they are resistant to deformation and stretching out by mantle convection. These domains are potential reservoirs for high ^{3}He/^{4}He compositions. Large domains in the asthenosphere with distinct isotopic signatures and clear boundaries have been recognized in several studies (Dupré and Allègre, 1983; Goldstein et al., 2008; Klein et al., 1988; Meyzen et al., 2007).

Mantle convection is driven by heat flow from the outer core and from internal heat generation and will generally tend to erase mantle heterogeneities. The fact that inhomogeneities on all scales exist in the mantle despite the convection counteracting them was a mystery for some time until studies pointed out that minor rheological differences could preserve distinct bodies during convection (e.g. van Keken et al., 2003) and therefore rather than full homogenizing of the inhomogeneities the convection of the mantle causes narrow geochemically distinct striations to form. Heterogeneities involving intrinsic density contrasts (chemical, rather than thermal) can also act as a driving force for convection. Some of the late-stage magma ocean cumulates and early melt products enriched in iron that crystallized in the transition zone or upper mantle might therefore have initiated convective flow while sinking to the core-mantle boundary.

Some of the early isotope geochemical studies, predating global seismic tomography, inferred an upper depleted and a lower primordial mantle (e.g. DePaolo and Wasserburg, 1976). There are still indications of near-primordial domains in the lower mantle that might be sampled by some of the large LIP-forming plumes (Jackson et al., 2010; Jackson and Carlson, 2011). The 660 km discontinuity caused by the bridgmanite-forming reaction with a negative Clapeyron slope was later recognized to have an inhibiting effect on the transport of cold material from the transition zone to the lower mantle (e.g. Christensen and Yuen, 1985). Seismic tomography has become a useful tool to image and evaluate the dynamics of subducting slabs descending through the transition zone and lower mantle (e.g. Fukao et al., 2001; van der Meer et al., 2009; Sigloch and Mihalynuk, 2013). A general picture of regional differences with variably stagnant slab material near the 660 km discontinuity has emerged. After periods of conductive heating (thermal equilibration) the bridgmanite-forming reaction can proceed, providing the required density excess for further sinking of the slab material. Based on the imaging of 28 slab remnants at different depths and their temporal and spatial relations to the reconstructed subduction zones at the surface, van der Meer et al. (2009) estimated an average sinking rate of 12 mm/year. A slab remnant would therefore traverse the entire mantle (2900 km) to the core surface in about 240 Ma, including the delay near the 660 km discontinuity.

Heterogeneity of the upper mantle is not only characterized by the convection-induced striations but also by the presence of plumes that introduce recycled material with different enrichment signatures from the lower parts of the mantle. The plumes do vary in their compositions both amongst different plumes and within a single plume. Shorttle et al. (2013) have shown intra-plume heterogeneity on the example of the Iceland plume and conclude that continuous mixing gradients in the isotopic signal of plume derived magmatism require strong provinciality (i.e. spatially and compositionally distinct mantle areas) of the source regions.

Mantle heterogeneities are reflected by the compositions of oceanic basalts, mantle xenoliths and abyssal peridotites. Peridotite samples can potentially reveal the original heterogeneities on very small scales (e.g. μm-m scale), whereas sampling by melt extraction from a wide source region homogenizes small- to intermediate-scale heterogeneities. Local to regional heterogeneities are most accurately reflected in MORB compositions where the melt supply is low and the time scale between melting and eruption is short (Rubin et al., 2009).The combined melt inclusions in primitive olivine phenocrysts or xenocrysts will generally sample a much wider spectrum of the primary melt compositions compared to the homogenized host lava (e.g. Maclennan et al., 2003a, 2003b; Shorttle and Maclennan, 2011). Sampling of basalts along the MORs, mostly performed by dredging, will reduce the spatial resolution further.

Large- to intermediate-scale mantle heterogeneities created by sinking oceanic slab material or extensive melt extraction, e.g. in the Hadean and early Archean, are folded, flattened and stretched by convective flow (e.g. van Keken et al., 2003). The extent of flattening and stretching depends on the rheological properties (e.g. viscosity contrasts) and the convective vigor. Highly viscous blobs may resist extensive stretching and preserve heterogeneities that could persist throughout Earth's history.

Inversion of geophysical data indicate a radial mantle viscosity structure with about 1-2 orders of magnitude higher values in the lithosphere and lower mantle than in the upper mantle, transition zone and D" zone (e.g. Mitrovica and Forte, 1997; Hager and Richards, 1989; Peslier et al., 2010). A downward viscosity increase from 10^{22} to 10^{23} Pa s in the 1000-2500 km depth range suggested by Steinberger and Calderwood (2006) might favor the preservation of heterogeneities and possibly also near-primordial mantle regions in the lower half of the lower mantle.

The recording and modeling of scattered seismic waves in the mantle indicate the presence of streaks and heterogeneities with dimensions of 8 to 50 km (Olson et al., 1984; Allègre and Turcotte, 1986; Hedlin et al., 1997; Ryberg et al., 2000; Helffrich and Wood, 2001; Helffrich, 2002). A detailed geochemical transect (Hf and Pb isotopic composition) with 5-10 km sampling distance along the SE Indian Ridge axis has also detected a bimodal compositional distribution with a period of about 20 km (Graham et al., 2006; Hanan et al., 2013). A recent study of $^3He/^4He$ in the same area (Graham et al.,

2014) confirms the presence of both enriched, i.e. pyroxenite or eclogite bearing, peridotite and more depleted peridotite in alternating heterogeneities of scales related to regional mantle flow (ca. 1000 km), "mesoscale" mantle flow (ca. 100 km) and by local variation of streaks and pods (ca. 30 km). The 30 km scale is very similar to the scale of variation in Hf and Pb isotopes in the same area (e.g. Hanan et al., 2013) and supports the evidence of heterogeneous small scale streaks and pods in the upper mantle. This pattern is interpreted as regularly spaced convective streaks. The cause for this "marble cake" mantle structure with widespread presence of relatively narrow and sharply defined streaks despite the convective stirring in the mantle are the differing viscosities of chemical heterogeneities, while other types of heterogeneities, such as thermal heterogeneities, are being eliminated by the convection within relatively short time, in the order of 75-200 Ma (Olson et al., 1984; van Keken et al., 2003). The remains of primordial heterogeneities, ancient melting events, mixing of different recycled components as well as lithological variations in the mantle source (Andres et al., 2004; Graham et al., 2006) have been discussed as possible origin of these widespread small scale heterogeneities.

1.2. The behavior and systematic of isotope systems and elements in the mantle

1.2.1. Isotopes and REE as geochemical tracers of mantle processes

Several of the common isotopic systems used in geosciences are tracers for specific processes in the mantle and help to identify different geochemical components of the mantle (for more detailed background information see Faure and Mensing, 2005).

The Rb-Sr isotopic system consists of two similar lithophile elements, with Rb being more incompatible in mantle minerals than Sr. Higher relative concentrations of radiogenic ^{87}Sr (^{87}Sr/^{86}Sr ratio) therefore indicate a time-integrated melt enrichment. Because the Sr isotope signal can easily be influenced by seawater alteration, it is important to avoid altered samples when analyzing Sr isotopes. Removal of easily accessible Sr-rich secondary minerals like carbonates by acid leaching is standard procedure before Sr isotope analysis of oceanic basalts.

The Sm-Nd system is governed by the similar behavior of the incompatible lithophile REEs Sm and Nd. Unlike in the Rb-Sr system, the radiogenic daughter Nd is more incompatible than the parent Sm. This leads to a reversed behavior with respect to melt-solid separation, with higher 143/144Nd ratio in the time-integrated depleted residue. Thus negative ε_{Nd} values are typical for enriched crustal rocks while depleted mantle has positive values (relative to CHUR with $\varepsilon_{Nd}=0$).

6

The Lu-Hf system also consists of two lithophile elements, but shows a stronger fractionation during melt extraction with the HREE Lu being less incompatible than Hf. Lu is even compatible in garnet, whereas Hf partitions strongly to uncommon mantle accessories like zircon or baddeleyite. Mantle-derived basaltic melts have therefore a lower Lu/Hf ratio than its residue which will acquire a higher ^{176}Hf/^{177}Hf ratio. ε_{Hf} is analogous to ε_{Nd} and the $\Delta\varepsilon Hf$ (delHf) index describes the distance of a given sample to the mantle array regression in an ε_{Hf}-ε_{Nd} space (as discussed by Andres et al., 2004). $\Delta\varepsilon Hf$ is a useful indicator of old melt depletion, characterizing SCLM with time-integrated high Lu/Hf ratios (Section 1.2.3).

The Re-Os isotope system is unique for the strongly different behavior compared to the previously described isotope systems with both elements being siderophile and Re being more incompatible to mantle minerals. Both elements are immobile in reduced environments and mobile in oxidizing environments. Highly refractory peridotite residues from early extensive melt extraction are characterized by very unradiogenic ^{187}Os/^{188}Os ratios as a consequence of Os-rich alloys, sulfides and oxides (e.g. Pearson et al., 2007; Burton et al., 2012).

The different radiogenic Pb isotopes originating from the decay of ^{238}U, ^{235}U and ^{232}Th indicate in general the enrichment of the mantle source with incompatible elements. Both U and Th are lithophile elements associating with Zr and REE. The differences in behavior of U, which is mobile in oxidizing environments and, and Th, which is much less mobile, have consequences for hydrothermal processes causing a fractionation with Th being enriched in the residual altered rock. Pb on the other hand is chalcophile and behaves as LILE. In addition the different half-lives of these three decay systems can be used to assess the timing of certain processes in some cases. The U-Pb isotope systems are not very useful for determining mantle components as they vary strongly depending on multiple factors such as age and metasomatism of the source mantle.

The $\Delta 7/4$ and $\Delta 8/4$ (here also referred to as del7/4 and del8/4, due to scripting issues with dynamical data extraction) indexes were defined by Hart (1984) as the deviation in ^{207}Pb/^{204}Pb and ^{208}Pb/^{204}Pb from an arbitrarily defined Northern Hemisphere reference line (NHRL) in a ^{207}Pb/^{204}Pb-^{206}Pb/^{204}Pb space and ^{208}Pb/^{204}Pb-^{206}Pb/^{204}Pb space respectively. They are reflecting somewhat different aspects of the isotopic system by excluding the imprint of enrichment and depletion. The large difference between the half-lives of ^{235}U and ^{238}U resulting in a faster relative growth of ^{207}Pb than of ^{206}Pb may provide information on the timing of former mantle differentiation events (e.g. recycling of oceanic crust or melt depletion) via the $\Delta 7/4$ parameter. This can however require additional parameters to assess properly as e.g. low $\Delta 7/4$ values can indicate both ancient depletion, where ^{235}U was extracted before much ^{207}Pb could form, as well as young enrichment, where little radiogenic Pb has formed yet. In contrast, $\Delta 8/4$ is a tracer of the time-integrated Th/U ratio of the source.
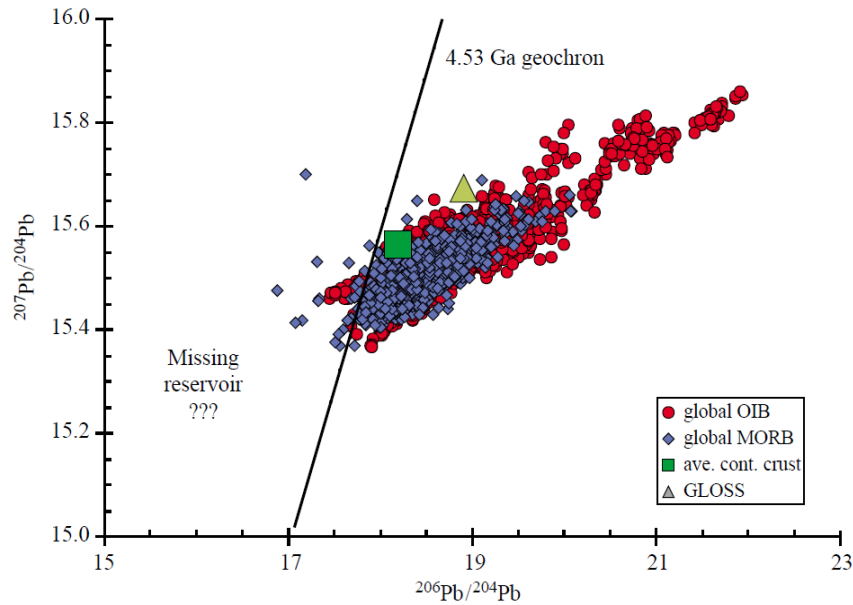
Figure 1: Illustration of the first Pb paradox: Crustal rocks contain more radiogenic Pb isotope compositions than the bulk Earth. To compensate this a "hidden" reservoir with very unradiogenic Pb isotope compositions must exist (from Hofmann, 2003).

The so called first lead paradox has been a major problem in isotope geochemistry since Allègre (1968) observed that the lead isotope composition in both MORB and OIB, as well as in upper continental crust, is more radiogenic than the assumed bulk silicate Earth. The location of the upper continental crust and primitive upper mantle (depleted MORB-mantle) to the right of the geochron (Figure 1) calls for an unradiogenic "missing lead" reservoir. The radiogenic character of the lead in MORB is particularly discordant with the basic theory of the upper mantle source of the MORB being depleted in extremely incompatible elements such as uranium due to the production of the crust by partial melting (Hofmann, 2003).

According to Burton et al. (2012) the highly radiogenic lead composition of the silicate phases of crust and mantle can be counterbalanced by the presence of sulphides with unradiogenic Pb isotopic compositions in the mantle. These sulphides, both interstitial grains and inclusions, are situated within (and therefore shielded) by refractory mantle domains and thus under most conditions prevented from contributing to melts. The lower continental crust and subcontinental lithospheric mantle are chemically diverse and often strongly affected by melt infiltration and metasomatic processes. A large fraction of the xenoliths and volcanic rocks originating from these domains, however, are also characterized by low U/Pb and U/Th-ratios, resulting in time-integrated (current) positions on the left side of the geochron and with high delta-8/4 (e.g. Hofmann, 2003; Wittig et al., 2010; Yang et al., 2012; Xu et al., 2012). This is due to the higher compatibility of Pb relative to U leading to a preferential enrichment of the lower crust in Pb and of the upper crust in U.

8

The second Pb paradox, also referred to as the kappa conundrum ($\kappa=^{232}$Th $/^{238}$U), describes the discrepancy between the κ values and the observed higher than predicted ^{208}Pb/^{206}Pb ratios in MORB and the upper mantle. The most viable explanation for this is the continuous preferential recycling of U relative to Th: While Th gets enriched and fixated in the continental crust, U is being recycled continuously, as it is fluid mobile as U^{6+} in oxidizing environments in the form of uranyl (Elliott et al., 1999). This allows for the U, which is also enriched in the continental crust, to be extracted from the crust and transported to the sea where it is refixated in the oceanic crust as U^{4+} by hydrothermal processes in more reducing environments. In this non-fluid mobile form U can then be subducted with the oceanic crust and can subsequently contribute to a high μ ($\mu=^{238}$U/^{204}Pb) component in the mantle (Section 1.2.3 for more details).

REE as incompatible elements with similar but slightly differing chemical properties and compatibility are good geochemical tracers for enrichment and can to a certain degree indicate the presence of some minerals, such as garnet or pyroxenes, in the source. Especially low HREE concentrations visualized in high Sm/Yb and Gd/Yb indicate garnet in the source mantle that holds back these highly garnet compatible elements. La/Sm and Ce/Sm are general tracers of source enrichment.

1.2.2. Crust-mantle differentiation followed by plate tectonics and the resulting element patterns

The chemical differentiation of the Earth into the core, mantle (possibly with several distinct domains), crust and fluid spheres has strongly influenced the major and trace element concentrations (Hofmann, 1997; 2003). The light to intermediate elements experienced some isotopic fractionation during these processes, and over time the various reservoirs have developed distinct radiogenic isotope ratios according to the fractionated ratios of parent to daughter elements.

The mantle is depleted in the incompatible elements that were extracted by the formation and growth of the continental crust, mainly by partial melting and successive ascent of the melt. This governs the chemical and isotopic characteristics of MORB. The compatibility (respectively incompatibility) of elements is controlled largely by their ionic radius and charge. The elements with ionic characteristics similar to the main constituents in the mantle minerals are compatible during melt extractions whereas those with different charge/radius ratios, particularly the large ion lithophile elements (LILE) become enriched in the melt phase (Hofmann, 2003). Another process contributing to the depletion of the mantle in incompatible elements is subduction related metasomatism with subsequent partial melting of the metasomatized mantle regions (Elliott et al., 1997).

A simple model viewing crust formation as extraction of partial melts from the mantle can explain the abundances of many trace elements. The simple melt extraction mechanism applies in particular to the

formation of the basaltic oceanic crust in the MOR environment. The subduction zone magmatism, responsible for a considerable fraction of continental crustal growth is more complex with the slab devolatilization efficiently transferring the LILE, e.g. the alkali metals, and various base metals to the mantle wedge undergoing partial melting to form arc magmas. In contrast, the HFSE, like U, Th, Nb, Ta, Ti, Zr and Hf are stabilized in eclogite and garnetite phases and transferred to the deep mantle, leading to the high-µ (HIMU) component of recycled oceanic crust (ROC) (Miller et al., 1994; Hofmann, 2003).

The generation of a HIMU-signature in ROC is further promoted by riverine transportation of U as dissolved uranyl from the upper continental crust to the ocean. During deep hydrothermal circulation near the MORs U tends to be fixated in the oceanic crust and lithosphere. In contrast, the same activity dissolves the base metals, including Pb, from the fresh magmatic rocks of the oceanic crust and deposits them as sulphides, as part of "black smoker" activity. Such sulphide deposits are easily remobilized in subduction zones. Intra-crustal melt extraction in the evolving arc crust above subduction zones also seem to leave much of the Pb behind in the resulting lower continental crust and thus allowing the possiblility of recycling (White and Duncan, 1996).

As the differentiation processes between crust, enriched and depleted mantle can be explained to a large extent by partial melting of an "ancient mantle", a simple mass-balance equation can be used to roughly describe it. This model assumes complete equilibrium within the mantle to start with and thus neglects local and "mesoscale" heterogeneities (as discussed above).

1.2.3.   The reservoirs of the mantle: Trace element and isotope signatures as tracers

A simplistic model with a depleted and a primitive part of the mantle comprises two distinct reservoirs within the mantle. Estimating the mass fractions of these postulated reservoirs has been attempted by many authors (e.g. Jacobsen and Wasserburg, 1979; O'Nions et al., 1979; Allègre et al., 1983) and the results range from 30 to 80% for the depleted reservoir. The most suitable elements for calculating mass balances are the highly incompatible elements, because their abundances in the depleted mantle are extremely low and thus errors have only relatively little influence on the calculation. Other elements are much more difficult to estimate.

An additional problem with estimates on mantle reservoirs is the question how the ~50% portion of the mantle evolved that was, from a mass balance point of view, not needed for the production of the continental crust. It may have stayed a homogeneous primitive reservoir, but it might also be differentiated into enriched and depleted reservoirs (Hofmann, 2003).

The variations of the mantle's chemistry are commonly interpreted as a mixture of four specific components, which are isotopically distinct parts of the mantle (Zindler and Hart, 1986): Depleted MORB mantle (DMM or DM), HIMU and two kinds of enriched mantle (EM 1 and EM 2). Later studies have added, and subsequently modified or redefined, the intermediate focal zone (FOZO) component to the canon (Hart et al., 1992; Stracke et al., 2005). The common component (C) and the prevalent mantle (PREMA) are more or less equivalent to FOZO in the way that they represent a general intermediate composition that is common in most of the mantle signal and can be represented by a mixture of the other endmember components.

The HIMU or high μ component is defined by high $^{238}U/^{204}Pb$ ratios ($\mu=^{238}U/^{204}Pb$) and consequently the most radiogenic Pb isotope signal. In addition HIMU-basalts are characterized by enrichments of the HFSE like Th (and U), Nb, Ta, Hf and Zr relative to average primitive mantle or BSE. In oceanic basalts (MORB and OIB) it is characterized by high $^{206}Pb/^{204}Pb$ (>20.5) and relatively low $^{87}Sr/^{86}Sr$ (<0.703) (Zindler and Hart, 1986; Hart, 1988). The origin of this component is either recycling of oceanic crust that has lost Rb and Pb during alteration (oceanic crust is enriched in U and Th) and subduction processes or metasomatized oceanic lithospheric mantle (Stracke et al., 2005).

A "young HIMU" component was proposed by Thirlwall (1997) to account for HIMU like compositions with negative $\Delta 7/4$ Pb values that are accompanied by relatively low $^{206}Pb/^{204}Pb$ values. This is implying that these represent HIMU compositions generated later than the "classical" HIMU composition and thus the decay of U isotopes has not progressed as far in them.

EM 1 and EM 2 representing the isotopically "enriched" components are characterized by higher $^{87}Sr/^{86}Sr$ and $^{208}Pb/^{204}Pb$ as well as lower ε_{Nd} and $^{176}Hf/^{177}Hf$ values than the other components, while the Pb isotopes are in range of the non-enriched mantle endmembers (DM and FOZO/PREMA) (Zindler and Hart, 1986; Stracke et al., 2005; Stracke et al., 2011). EM 1 has relatively lower $^{87}Sr/^{86}Sr$ values (0.705-0.706) and $^{143}Nd/^{144}Nd$ (ε_{Nd} < -4) compared to EM 2 ($^{87}Sr/^{86}Sr$ = ca. 0.707; ε_{Nd} = ca. 0 to -1). EM 2 is also more enriched in radiogenic Pb. The EM components are most likely related to continental material recycled for example as marine sediments (which have high Th/U and low (U,Th)/Pb ratios). Possibly EM 1 represents recycled subcontinental lithosphere (SCLM) and lower continental crust while EM 2 is related to recycled pelagic sediments formed from upper continental crust (UCC) (Hofmann, 1997; Stracke et al., 2005; Stracke et al., 2011). Alternative models have suggested metasomatism of DM as origin of the EM components but did not explain the related trace element patterns well (Workman et al., 2004). Because of the unclear source contributions to EM 1 and EM 2, in this study other more source specific terms (as discussed below) will be used preferably for the description of the enriched components. The growth of the dataset of oceanic basalts over time has provided diverse compositions in the array between EM 1 and EM 2, supporting the existence of a

continuous array of EM compositions instead of just two endmembers (Willbold and Stracke, 2006, 2010; Stracke et al., 2011).

Recycled oceanic crust (ROC) is being processed at least twice during the recycling process: via initial hydrothermal alteration at the MOR, during subduction where fluid mobile elements such as Pb are extracted from it and commonly during decompressional carbonatitic melting and related metasomatism that may refertilize the the upper mantle with parts of the ROC (Rohrbach and Schmidt, 2011; Cottrell and Kelley, 2013). ROC in the mantle is characterized by low $\Delta 8/4$ (i.e. high time-integrated U/Th) and low $\Delta\varepsilon Hf$. Therefore the signature of ROC resembles the HIMU. The age and recycling history of ROC controls the actual signature in MORB. The recycling of relatively recently subducted material can lead to a HIMU-like signature without the highly radiogenic Pb isotopes ("young HIMU" as proposed by Thirlwall, 1997), while more highly radiogenic Pb isotope compositions can either be generated by carbonatitic melt extraction from old oceanic crustal material that contains high radiogenic Pb compositions or by or by old carbonatitic melt extraction from ROC followed the growth of the radiogenic Pb signature over time.

Upper continental crust (UCC), probably represented by the EM2 component (e.g. Jackson et al. 2007), is present in the mantle as recycled pelagic sediments.Lower continental crust (LCC), which is characterized by low μ and therefore unradiogenic Pb compositions, has high $\Delta 8/4$ and $\Delta\varepsilon Hf$ values as well as radiogenic Os isotope compositions.

The presence of subcontinental lithospheric mantle (SCLM) as opposed to lower crustal lithospheric components is indicated by highly unradiogenic Os isotope ratios ($^{187}Os/^{188}Os$=ca. 1.2) as Os is highly compatible in Os-Ir-alloys and sulfides and therefore stays in the residue during melt extraction (as discussed by Burton et al. (2012). SCLM is also indicated by high $\Delta 8/4$ and $\Delta\varepsilon Hf$ as well as radiogenic $^{87}Sr/^{86}Sr$. In most SCLM the Hf and Nd isotope systems are not correlated due to melt depletion succeeded by carbonatitic metasomatism and enrichment of LREE (Escrig et al., 2004; Ionov et al., 2005; Simon et al., 2007; Salters et al., 2011). Due to the occurrence of partial melting and metasomatism at the root of continents, for example related to subduction, SCLM varies in its composition and can be present in a depleted form as well as enriched (Wittig et al., 2010; Xu et al., 2012; Yang et al., 2012). SCLM metasomatically enriched by carbonatitic melts as discussed by Wittig et al. (2010) has elevated concentrations of incompatible elements and Sr, Nd and Hf isotope ratios shifted towards HIMU as well as a raised $^{232}Th/^{238}U$ ratio.

The FOZO component is an intermediate mantle component argued to be a mixture of the other mantle components. It possesses moderate HIMU-like characteristics, such as a relatively radiogenic Pb isotope signature and more radiogenic Sr isotope ratios (206Pb/204Pb = 19.4, 87Sr/86Sr = 0.7030–0.7032) (Workman et al., 2004; Stracke et al., 2005).

12

In OIB (Ocean Island Basalt) the four mantle endmembers DMM, HIMU, EM 1 and EM 2 are reflected not only in their isotopic and trace element signatures but also by distinct main element compositions (Jackson and Dasgupta, 2008), such as high CaO/Al_2O_3 and FeO_T in HIMU basalts which is also reflecting their oxygen fugacity (Cottrell and Kelley, 2013). Also a plot of CaO/Al_2O_3 vs. K_2O/TiO_2 perfectly resolves the four mantle end member lavas for OIB (Jackson and Dasgupta, 2008). MORBs are dominated by the depleted mantle endmember and consequently have much less extreme compositions and therefore also less distinct signatures of mantle components.

1.3. MORB geochemistry

1.3.1. Why can we use MORB to talk about its source?

Several mechanisms are being discussed as key factor to govern MORB composition, the most likely of them being variation of the melt fraction induced by changes in mantle potential temperature and variation of mantle source composition. Geochemical variation of MORB has long been seen to reflect partial melting of an inhomogeneous "marble-cake" upper mantle (Allègre et al., 1984; Morgan and Morgan, 1999; Stracke et al., 2005). Although some studies have argued for the source composition as only important factor (Shen and Forsyth, 1995; Niu and O'Hara, 2008) while others have argued for temperature variations within a homogeneous asthenosphere alone to be able to explain the range of MORB compositions (Klein and Langmuir, 1987; Langmuir et al., 1993) it is most likely that both factors together are controlling the composition of MORB in a correlated way (Dalton et al., 2014) as high heat flux and geochemical enrichment are generally related to mantle upwelling. Compositional variations alone cannot explain geophysical observations like the heat flow on MORs, the velocity of seismic shear waves or the depth variation of the ridges, while temperature variation fails at explaining the different isotopic signatures, REE compositions and abundances of trace elements present in MORB. On top of that the abyssal peridotites themselves show that the upper mantle is heterogeneous (e.g. Salters and Dick, 2002; Seyler et al., 2003).

Due to the size of the area contributing to the melts forming MORB the smallest heterogeneities of the mantle are not sampled by it (Stracke, 2012). This naturally evens out the much higher small scale variability of mantle peridotites (Compare section 1.1.2).

Hofmann (2003) reasons that the MORB variations of highly incompatible elements and the ratios between these are only weakly affected by initial fractional crystallization, because subtraction of minerals like olivine and Cr-rich spinel will rather uniformly elevate the incompatible element concentrations in the melt. Some of the incompatible element ratios may be affected by fractionation of plagioclase and clinopyroxene, but the great majority of MORB is undersaturated with latter phase.

Therefore, most obvious explanation of variations in the incompatible element ratios in MORB is source heterogeneity.

MORB is formed from partial melts of the upper mantle and therefore only partially reflects its mantle source. The more enriched components on all scales of the local source mantle, ranging from lenses and streaks of enriched material to incompatible elements in zonated mineral grains, are melting at lower temperatures than the more refractory depleted components and thus are more strongly reflected in MORB. Therefore the presence of refractory material in local inhomogeneities can only be confirmed with the study of abyssal peridotites.

On top of that, the melts forming MORB are potentially experiencing magma mixing, assimilation of local rocks and fractional crystallization during their ascent. For MORB only fractional crystallization plays a significant role. Fractional crystallization is strongly affecting the composition of main and compatible elements, but mathematical formulas exist to normalize MORB to a comparable degree of fractionation which provides information about the source composition.

The quantity of local MORB generation as well as its geochemical signature can be strongly influenced by hotspots, depending on the proximity of a hotspot to a MOR and the strength of the hotspot, indicated by its magmatic activity, which in turn is depending on the temperature and fertility of the plume material (Vlastelic et al., 1998; Hekinian et al., 1999; Maia et al., 2011). Often the strongest isotopic effect of hotspots is in the more distal parts of its influenced area, where smaller degrees of fractional melting occur and different melts generated from different sources (Hart et al., 1973; Schilling, 1973; Thirlwall et al., 2004; Nicolaysen et al., 2007). Plume material can be deflected horizontally over several hundreds of km at sub-lithospheric depths (French et al., 2013) as well as in the asthenosphere near and along MORs (Thirlwall et al., 2004). Due to this mobility of plume material it is possible that relatively isolated occurrences of enrichment (such as to the east of Réunion; section 3.2.3) are caused by deflected hotspot material.

Zindler and Hart (1986) acknowledge the problem of isotopic ratios depending not only on the initial composition but also on the age of the material. In this study only young MORB samples have been used to minimize the effect of the rock age. The influence of different ages of source material on the other hand can still be reflected in the MORB and can help with distinguishing different mantle reservoirs. Another complication when attempting to correlate mantle source and MORB compositions is the possibility of contamination of the melts and of the MORB itself by the influence of seawater and metasomatism.

Hofmann (2003) reasons that variations of highly incompatible REE compositions in MORB are only weakly controlled by the degree of fractional crystallization in the magma as it cannot explain the

14

relative variability of the abundances of elements with very similar chemical behavior. The most obvious explanation of these variations is source heterogeneity.

Salters et al. (2011) explain the subparallel Hf-Nd arrays with a variation of a highly depleted residual mantle component in the upper mantle. Heterogeneities of this depleted component could be a cause of the bad correlation of ε_{Nd} and ε_{Hf} in MORB. Alternatively the lack of sampling resolution could be the cause. Unlike in OIB, the Hf and Nd isotopes in MORB are not well correlated. This is most likely the result of heterogeneities in the upper mantle, with ancient highly depleted material being mixed with the other mantle components (Salters et al., 2011). It has alternatively been attributed to varying garnet contents in the source rocks (Salters and Hart, 1991) and to disequilibrium melting inducing isotopic disequilibrium on the grain scale (Blichert-Toft et al., 2005).

Limitations of the use of isotope systems as geochemical tracers arise when trying to identify components with very similar (isotopic) compositions but different history or genesis. This is for example a problem for answering the question if the DUPAL signature of the southern Atlantic is related to shallow detached or deep recycled continental material (Class and Le Roex, 2011). A further complication is caused by the complex heterogeneities, age variations and intricate metasomatic or metamorphic histories of components such as SCLM or recycled lower continental crust (LCC). According to Class and Le Roex (2011) certainty of the source of a recycled component can only be gained by comparing it with samples of potential source regions (in that case continental cratons and belts).

Isotope fractionation does occur in chemical processes due to the mass differences between isotopes. It has a significant influence on the behavior of light elements such as sulfur and oxygen, but its effects are negligible for heavy elements, as for heavy elements the relative mass difference between isotopes is small. For the studied isotopic systems such as U-Pb, Sm-Nd and Re-Os the latter is the case and the fractionation between the mother and daughter isotopes, which have different chemical properties, is much stronger than the effects of the different isotopes of the same element.

The age of a rock has a strong influence on many isotopic ratios, but nearly zero-age MORBs as studied here have radiogenic isotope compositions (involving the common long-lived decay systems) that are practically identical to their accumulated (weighed) mantle source contributions.

The influence of the sampling resolution (Salters et al., 2011; Hamelin et al., 2012) on biasing the data set towards wrong tendencies is a potential problem with the relatively scarce datasets such as the Hf and Os isotope data.

The definition and use of "standard" MORB compositions (N-MORB, E-MORB etc.) to compare and categorize the abundance of rock composition is not helpful in the context of this work and in most other applications as there are no typical MORB compositions. Instead there is a continuum of variations both in main and trace element composition and in isotope ratios (compare Hofmann, 2003).

1.3.2. Isotope ratios in MORB

Due to their half-lives, which are greater than the age of the Earth, the "common" long lived decay systems based on the radioactive isotopes ^{147}Sm, ^{87}Sr, ^{186}Hf, ^{187}Re and ^{232}Th have a nearly linear accumulation of their daughter isotopes. This makes them more straightforward to understand than the U decay chains contributing to the complex signal of the lead isotopes with their shorter half-lives. Strontium neodymium and hafnium isotopes all correlate well amongst each other. They correlate poorly with ^{206}Pb/^{204}Pb or ^{208}Pb/^{204}Pb with the exception of Indian ocean MORB which does not show any significant correlation. The ratio of radiogenic lead ^{208}Pb*/^{206}Pb* on the other hand does correlate with neodymium isotopes in all MORBs. These global correlations show that lead behaves in a different way than the coherently behaving elements neodymium, strontium, hafnium, thorium and uranium (compare section 1.2.1 and 1.2.2; Hofmann, 2003).

Also along the spreading ridges large scale isotopic differences occur and indicate the existence of source heterogeneities. These large scale heterogeneities were first described by Dupré and Allègre (1983). The anomaly in Indian Ocean MORB was named DUPAL anomaly by Hart in 1984. The age of this isotopic anomaly was estimated to be at least 1.5 Ga old (Rehkämper and Hofmann, 1997). This is important evidence for the long term stability of heterogeneities within the mantle and against the homogenization of the mantle by convective circulation.

The global spectrum of MORB forms distinct "local" subparallel, non-overlapping Hf-Nd-isotopic arrays indicating distinct domains of the upper mantle which are composed of a component with radiogenic Nd and Hf, one with unradiogenic Nd and Hf, and possibly additional components (Salters et al., 2011). According to Salters et al. (2011) the MORB trends indicate an enriched component with a composition similar to OIB ("within or extension of OIB array"), while HIMU is of minor importance. A contribution of SCLM, which is depleted in Hf and therefore develops low time-integrated ^{176}Hf/^{177}Hf ratios, to the oceanic lithosphere could potentially be responsible for its present broad range in Hf isotopic compositions (Salters et al., 2011).

The Re-Os isotope system is still not as well understood and there is fewer data available than for the previously discussed systems. Osmium is a compatible element, while Re is incompatible. Thus this system behaves differently to the previously discussed ones with the "daughter" Os remaining in the mantle while the "mother" Re is extracted from the mantle by partial melting (Hofmann, 2003). A

16

problem with Os analyses is that the Os concentrations are often at sub ppb concentrations. That means even small contaminations with seawater or material altered by seawater can significantly affect the isotope signal. Additionally it is a challenge that Os is distributed very heterogeneously within the sampled rocks, being mainly incorporated in the mostly refractory non-silicate phases. This may lead to the effect that the analyzed Os rich phases are not representing the whole sample. A third problem with Re-Os isotopes is that the isotope ratios of peridotites and MORB are very different, implying the Os isotopes in MORB do not necessarily represent the source (Hofmann, 2003). It is possible that this problem can be resolved with local mantle heterogeneities: enriched pyroxenitic material is providing a high Re/Os endmember and depleted peridotite is providing low Re/Os endmember.

1.3.3. Trace elements in MORB

According to the simplified "standard" model of Earth, the upper mantle is depleted in incompatible elements. MORB as a partial melt derived from this depleted source can still be enriched in incompatible elements when compared to primitive mantle but it still shows a relative depletion of highly compatible elements compared to moderately incompatible elements.

The significant variability of trace element abundances in MORB depends on various factors, with the source composition, the degree of melting and assimilation (contamination) and fractional crystallization (AFC) of the melt. The governing process for MORB chemistry is most likely the source composition. This is implied by the fact that MORB generated close to hot spots showing distinct trace element patterns (O'Hara, 1977; Hofmann, 2003). Also peridotites from those areas imply a higher than "usual" degree of melting of an initially more enriched source (Johnson et al., 1990).

The trace element abundances of MORB vary highly in the most incompatible elements, while they are much more uniform when it comes to the more compatible elements. This phenomenon can be explained by the equation $C_1 \approx \frac{C_0}{F}$ for highly incompatible elements (F is melt fraction) and $C_1 \approx \frac{C_0}{D}$ for compatible elements (D is partition coefficient). These equations show that the concentration of highly incompatible elements in the melt is inversely proportional to the melt fraction, while compatible elements with D close to 1 are buffered by the source. This means the variability of trace elements depends on their partition coefficient (Hofmann, 1988; 2003).

1.3.4. The main element systematics of MORB

The main elements, as the trace elements, vary in compatibility and therefore behave differently during the extraction of partial melts. During partial melting in equilibrium with the source ("batch melting") the equation $\frac{C_L}{C_0} = \frac{1}{D(1-F)+F}$ describes the behavior of an element depending on its bulk distribution coefficient D (with C_L: concentration in liquid; C_0: starting concentration; D: bulk distribution coefficient; F: melt fraction) while during fractional melting $\frac{C_L}{C_0} = \frac{1}{D}(1-F)^{\left(\frac{1}{D-1}\right)}$ applies. In both cases incompatible elements, which are defined by D<1, are enriched in the melt relative to the source. D varies with differing mineralogical composition, pressure P and temperature T. Most importantly for MORB Fe is being enriched in basaltic melts relative to the source mantle while Mg is more compatible and gets enriched in the residual. The concentrations of some incompatible elements such as Na as well as the Ca/Al ratio in a basaltic melt are independent from P and can be used as indicators of the extent of melting F (Jaques and Green, 1980; Klein and Langmuir, 1987).

During the ascent of the melt also fractional crystallization takes place and the elements that are compatible in the crystallized minerals are being extracted from the melt. Fractional crystallization follows relatively predictable paths of relative enrichment and extraction of elements. In order to derive some information about the source composition it is therefore possible to execute a fractionation correction to a hypothetical primary melt composition in equilibrium with the upper mantle (section 2.2).

As the main element chemistry of MORB is governed the extent of partial melting of the source mantle, which in turn depends on the potential temperature and the fertility of the source region, the main elements in MORB are not the best and most straight forward to use tracers of the mantle source composition. Unlike for the isotopic signal and the concentrations of incompatible trace elements, several studies (Klein and Langmuir, 1987; Dalton et al., 2014) have shown that source heterogeneity is not necessary to explain the global main element variation of MORB, but the correlation of mantle temperature, ridge depth and MORB main element composition suggests a variation of the temperature of the upper mantle by 250°C alone is sufficient to explain it. Other authors (e.g. Niu and O'Hara, 2008) argue for the source mantle variation as the sole important factor and consider temperature variation of more than 50°C outside of the influence of hotspots as unlikely.

1.4. Aim of study

The mechanisms of subducted oceanic crust and lithospheric mantle sinking down into the lower mantle are well understood thanks to seismological and mineralogical studies. Its counterpart, the upwelling of material from the lower to the upper parts of the mantle is less understood. The roles of deep as opposed to shallow origin of the asthenospheric material and of punctual plume flux as opposed to general upwelling of the ambient mantle are debated. The MORBs offer the largest accessible geochemical mantle signal available. The asthenosphere below the MORs does not only reflect the composition of the upwelling mantle, but is also potentially affected by the input of continental material, such as SCLM or LCC, through shallow processes such as a general convective erosion of the lithosphere and crust or specificdetachment related to rifting and continental breakup.

To investigate the provenance of the asthenosphere on length scales, it is necessary to discriminate the different refractory and fertile components in the asthenosphere responsible for the MORB variability. These include the residual (depleted) upper mantle (depleted MORB mantle, DMM), possible lower mantle of depleted or primordial nature, as well as the enriched components ROC (HIMU), SCLM and LCC (EM1-type) and upper continental crust (UCC), recycled as pelagic sediments (EM2-type).

2. Methods

2.1. Data collection, evaluation, processing

The global MORB dataset used in this study was acquired from the PetDB database (2014). The complementary database GEOROC was not used, because it contains only a small amount of samples from the MORs that cover only areas already well reflected in the PetDB samples. The initial criteria used for the database search were sample class: "igneous", "mafic", "volcanic", Alteration: "fresh" (i.e. unaltered) and tectonic setting: "spreading center". Multiple analyses of identical samples were compiled as one entry.

These samples were reduced to those actually from active MORs by excluding those older than 10 Ma with the help of the sea floor age grid by Müller et al. (2008) and excluding back arc basins (i.e. Lau Basin, W-Pacific). Samples containing "outliers", i.e. extreme compositions, in the dataset were carefully cross checked with the original publications and if possible wrong or missing records in the data from PetDb were corrected accordingly (most notably Blichert-Toft et al., 2005). Extreme outliers have only been deleted or corrected if the same sample had newer data available for the same parameters (CHR0098-008) or if the data was incorrect in respect to the original publication. Some of the Nd isotope data from Sims et al. (2002) that contained obviously mismatching ε_{Nd} for the reported 143Nd/144Nd in the original publication was excluded as it was impossible to tell which of these were correct. As many samples with unusual compositions as possible were kept to preserve possible unusual geochemical signatures in the dataset. This includes as most extreme case the sulfide rich high Fe-Ti basalts from the Galapagos rise. Unlike in other studies samples from shallow ridges and near hotspots have not been excluded. Also the completeness of the total dataset has been valued higher than the completeness of single samples, i.e. also data points with very incomplete chemical information have been kept instead of focusing on the highest quality data points only.

To avoid the loss of comparability of samples with very different degrees of fractionation highly fractionated samples with Mg<6 wt. % and SiO_2 >53 wt. % (similar to Niu and O'Hara, 2008; Brandl et al., 2013) were excluded from this study.

Unlike in numerous other studies (e.g. Niu and O'Hara, 2008; Dalton et al., 2014) the data was not averaged for ridge segments or similar regional or local areas as those areas with inhomogeneous compositions may have bimodal distributions of the varying samples. In this case an averaging would not have represented any real composition and would have taken away information about multiple sources in these regions.

A correction for Sr loss by sea water alteration has not been performed, as only fresh samples were chosen from the database for this study.

To provide some overview over the dataset and a better comparability of the different ocean basins, all data points have been assigned to one of five regions (Figure 2): (1) the Atlantic south of Iceland, (2) the Arctic Ocean and the Atlantic north of Iceland, (3) the Pacific Ocean, (4) the Indian Ocean and (5) the Caribbean (Cayman trough). Sub-regions for the more detailed discussion were chosen with the practicability for along ridge plots in mind.
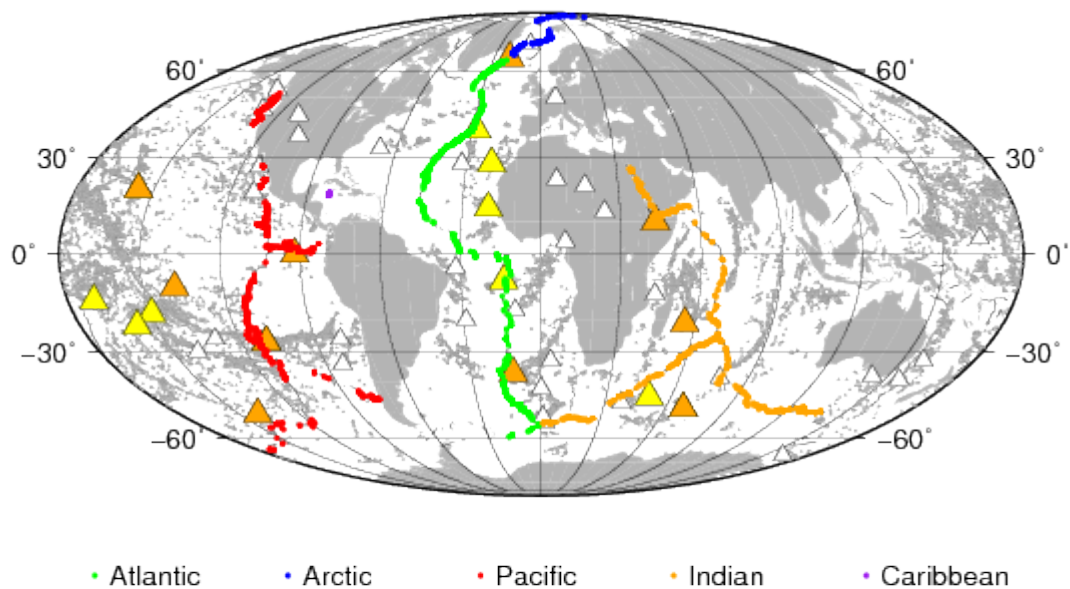
Figure 2: Global distribution of MORB samples, colored according to the main regions defined for use in this study. Hotspots are marked by triangles, colored as follows: Orange: likely deep hotspots according to Courtillot et al. (2003); yellow: additional potentially deep sourced hotspots according to Montelli et al. (2006) and Courtillot et al. (2003); white: other hotspots from Courtillot et al. (2003). Seamounts (Wessel, 2001) are indicated by tiny grey triangles.

2.1.1. Additional data

The hotspots shown on the maps and taken in consideration in the further analysis were selected in a similar way as in Burke et al. (2008). Hotspots certainly or likely related to deep plumes were chosen after Courtillot et al. (2003) with additional deep seated hotspots added to the list from Montelli et al. (2006). Other hotspots, i.e. occurrences of not necessarily deep sourced intra-plate volcanism, were taken from Courtillot et al. (2003). The Amsterdam hotspot was added to complete the list (from Maia, 2011) as it has a strong signature on the MORB signal. Seamount locations are from Wessel (2001).

Additional geophysical and geographical data used were the crustal thickness grid CRUST1 (Laske et al., 2013) for a model of the thickness of the oceanic crust without overlaying sediments, which for regional maps (Appendix 1) was cut out to values of less than 10 km to make smaller variations of the thin oceanic crust more visible, ETOPO1 (Amante and Eakins, 2009), with which waterdepths for every data point have been generated to create a consistent dataset and to be able to also use data with missing waterdepth information from the database, and the GOCE gravity anomaly grid (Knudsen and Andersen, 2010).

2.2. MORB normalization

Fractionation correction calculations of MORB have the purpose of providing comparable standardized compositions for hypothetical primary melts in equilibrium with, and therefore representing, the source mantle. Additionally the behavior of Na which is an established element for estimating the degree of melting for MORB production allows the standardization of the MORB compositions to a certain fraction of melting for a comparison of their source chemistry.

In this study a selection of key oxides were corrected for low P fractionation according to the procedures developed by Klein and Langmuir (1987). The calculations were done following Kelley et al. (2006) with the expressions by Klein and Langmuir (1987) for the calculation of Na8 and Fe8 and those by Taylor and Martinez (2003) for $TiO_2$8. Also in accordance to Kelley et al. (2006) Na8.5, Fe8.5 and $Ti_2$8.5 corrected to 8.5 wt% MgO have been calculated from the values corrected to 8 wt% MgO following the olivine + plagioclase cotectic with the algorithm of Weaver and Langmuir (1990). For the correction to 8 wt% MgO only samples with MgO>7 wt% have been used while for the correction to 8.5 wt% MgO samples with MgO up to 8.5 wt% have been included as well.

Niu and O´Hara (2008) claimed that the fractionation correction to a fixed MgO composition does not reflect the variability of the melts of a given Mg# and that Na8 and Fe8 are not in equilibrium with a primitive enough olivine to represent the mantle source. They also claimed that Na8 and Fe8 vary in the same way as the uncorrected data. They proposed a correction calculation to Mg#=0.72 (in

equilibrium to olivine of $Fo_{89.6}$) as an alternative method. The results of this are virtually identical to the corrections to equilibrium with an olivine of Fo_{90} as executed by Kelley et al. (2006) or Dalton et al. (2014). In order to compare it to the fractionation correction to a given concentration of MgO Si72, Ti72, Al72, Fe72, Mg72, Ca72, Na72, K72 and P72 have been calculated following the method of Niu et al. (1999) used by Niu and O´Hara (2008). In the discussion (Section 4.1.2) this method is compared to the corrections to 8 wt% MgO and to 8.5 wt% MgO.

Limitations of all fractionation correction calculations arise from the fact that they are based on simplifications and assumptions and even if they provide a realistic composition for the primary magma, it is at best a possible solution and never a definitive solution that can be achieved. Due to the necessary simplifications all the models used for the calculations have problems with reflecting variations in the source mantle. For example they assume a more or less homogeneous source mantle by correcting to a fixed MgO content or a fixed Mg# and consequently a fixed olivine composition to equilibrate the hypothetical primary melt with: Niu and O´Hara (2008) account for the variation of Fe and MgO at a fixed Mg# while the other methods allow the variation of Mg# at a fixed MgO content.

3. Data presentation and discussion

3.1. The global MORB data set: An overview

To set up a framework for the regional discussion the global dataset has been characterized in respect to a selection of the commonly used geochemical tracers of mantle composition and processes explained in chapters 1.2 and 1.3. As in the following regional discussions $^{87}Sr/^{86}Sr$, ε_{Nd}, ε_{Hf}, $^{206}Pb/^{204}Pb$, $^{207}Pb/^{204}Pb$, $^{208}Pb/^{204}Pb$, $\Delta7/4$, $\Delta8/4$, $\Delta\varepsilon Hf$, Ca_{72}/Al_{72}, Fe_{72} and La/Sm were selected. Further discussion of major and minor element variation will follow in the regional (Section 3.2) and the global geochemical discussion (Section 4).

The major element systematics of MORB in relation to geophysical features are well established (e.g. Klein and Langmuir, 1987; Niu and O'Hara, 2008; Dalton et al., 2014) and follow globally applicable rules with crustal thickness, ridge depth (i.e. elevation) and gravity anomaly patterns generally being correlated to fractionation corrected main element abundances, such as Ca_{72}/Al_{72} or Fe_{72}. It is therefore only of interest to investigate their relations on a smaller scale to see if deviations occur.

Generally enrichment indicated by $^{87}Sr/^{86}Sr$, ε_{Nd}, ε_{Hf}, $^{206}Pb/^{204}Pb$, $^{207}Pb/^{204}Pb$ and $^{208}Pb/^{204}Pb$, particularly in the more extreme cases, is present in areas near plumes. Not all plumes have identical signatures though, and some are depleted with respect to certain isotope systems. Although the isotopic systems as well as REE ratios exemplified by La/Sm usually correlate, in some settings decoupling can occur. E.g. Hf and Nd isotopic ratios are usually correlated, except for Iceland and the AAD (Blichert-Toft et al., 2005; Hanan et al., 2004; Meyzen et al., 2007).

The Sr isotope signal (Figure 3) is globally dominated by low 87/86 Sr ratios <0.703. Higher ratios occur exclusively near some hotspots (Amsterdam, Marion/Crozet, Louisville, Baja, Bouvet; less pronounced: Azores, Tristan, Afar; Jan Mayen, East of Reunion) and on the eastern SEIR (135°E). High ratios (>0.705) can be found at the Amsterdam hotspot, the AAD and most extremely on the eastern Galapagos Ridge (86°W).

$^{143}Nd/^{144}Nd$ (and therefore also ε_{Nd}) show a pattern very similar but not identical to the reversed Sr isotope signal. High $^{143}Nd/^{144}Nd$ ratios (>0.51255) are prevalent globally and more pronounced (>0.513) in the areas of the Pacific and Atlantic not close to hotspots (Figure 4). The close vicinities of most hotspots are characterized by lower Nd-ratios (0.51255-0.513) than those of the wider surroundings. Ratios lower than 0.5126 are only present at the Amsterdam hotspot, between the Marion and Crozet hotspots, between the Tristan and Bouvet hotspots (Southern Atlantic 48-49°S) and near the Azores.

The global variation of the ^{176}Hf/^{177}Hf ratio (and thus ε_{Hf}) divides the MORs into two large domains with the Atlantic north of ca 15°N having predominantly high ratios, whereas the southernmost Atlantic, the Indian Ocean and the Pacific are dominated by relatively low ratios (Figure 5). The lowest values are to be found (<0.2830) in the southernmost Atlantic between the Tristan and Bouvet hotspots and at the Amsterdam hotspot while ratios higher than 0.2833 occur in the Atlantic north of 20°N, in the vicinities of the Ascension hotspot and the Crozet hotspots, as well as in isolated locations on the eastern margin of the Easter micro-plate and at the AAD at 125°E on the SEIR. Whereas most hotspots such as Galapagos, Tristan, Bouvet/Meteor, Amsterdam and Marion are related to local and regional minima in ^{176}Hf/^{177}Hf, Ascension forms a maximum. The Azores, Iceland (including Jan Mayen), Easter and Crozet hotspots show both high and low ratios in their surroundings with the low ratios being dominant.

The global dataset for ^{187}Os/^{187}Os is far from complete, but shows a remarkable picture with almost all the available ratios between 0.125 and 0.145 except for one location on the western SWIR near the Marion and Crozet hotspots that has a uniquely high ratio of ca. 0.34 (Figure 6).

The global ^{206}Pb/^{204P}b, ^{207}Pb/^{204}Pb and ^{208}Pb/^{204}Pb patterns in MORB are very similar, but not identical, to the geographical extent and intensities of minima and maxima varying and not all features being represented by all systems. The decoupling of the different Pb isotope systems in some regions can be attributed to the different behavior of U and Th during recycling (as discussed in Section 1.2.1).

Globally, the ^{206}Pb/^{204}Pb ratios in MORB range from 16.6 to 20.1 with high ratios (>19) being mostly tied to hotspots and the most extreme ratios occurring in the equatorial central Atlantic near the Fernando Hotspot and at the Azores (Figure 7). Low ratios (<18) are mostly present in the Indian Ocean, most notably on the SWIR, but also occur near Ascension, the Louisville Hotspot, in the Arctic and the northern Atlantic.

The ^{207}Pb/^{204}Pb ratios cover the range between 15.31 and 15.73 with high ratios (>15.55) generally occurring near hotspots (Figure 8). The highest ratios occur near the Bouvet hotspot, the Azores, the Afar hotspot, in the Red Sea, on the Eastern Chile ridge and near the Fernando Hotspot. High ratios in areas not in the closer vicinity of hotspots occur not only on the Chile ridge, but also on the eastern SEIR (135°E), on the central EPR (ca. 12-15°S), the MAR near 12°N and the southern CIR (ca. 16°S; potentially related to Réunion hotspot) while other areas where high ratios are present are close to hotspots. Also some hotspots do not show high 207Pb/204 Pb ratios in MORB in their vicinities, such as the Iceland (although slightly elevated ratios occur near Jan Mayen) hotspot, as well as the Crozet and Marion hotspots near the SWIR. Particularly low ratios are dominating the Arctic Ocean, the adjacent northernmost MAR, the northernmost CIR, the SEIR at the AAD (118-126°E) and the eastern third of the SWIR.

The ^{208}Pb/^{204}Pb ratios range from 36.9 to 39.7 and their pattern shows fewer pronounced maxima than visible in ^{207}Pb/^{204}Pb (Figure 9). Most prominently the Bowie, Cobb, Tristan, Easter, Baja and Socorro hotspots have much less pronounced signatures. On top of that the ^{207}Pb/^{204}Pb maximum on the central EPR (ca. 12-15°S) is not represented in ^{208}Pb/^{204}Pb. Compared to ^{207}Pb/^{204}Pb also additional areas with extremely low ratios are visible, such as the MAR north of the Tristan hotspot (2-5°N), the SWIR near the Marion and Crozet hotspots and the SEIR between the Amsterdam hotspot and the AAD. In very few segments, such as on the central EPR (ca. 12-15°S) and the northern Red Sea, the two Pb isotope systems are completely decoupled and high ^{207}Pb/^{204}Pb ratios coexist with low ^{208}Pb/^{204}Pb ratios

The $\Delta\varepsilon$Hf values show the position of samples relative to the mantle regression line in ε_{Nd}-ε_{Hf} space (positive $\Delta\varepsilon$Hf imply a position above the regression line, with high relative ε_{Hf}). The $\Delta7/4$ and $\Delta8/4$ values are the positions of samples relative to the Northern Hemisphere Reference Line in the diagrams with ^{207}Pb/^{204}Pb versus ^{206}Pb/^{204}Pb and the ^{208}Pb/^{204}Pb versus ^{208}Pb/^{204}Pb, respectively. The $\Delta\varepsilon$Hf and $\Delta8/4$ are generally high in recycled old SCLM, whereas high $\Delta7/4$ might characterize very old and strongly melt depleted (lower) mantle.

The global $\Delta 7/4$ pattern (Figure 10) generally reflects the ^{207}Pb/^{204}Pb pattern. The parameters are positively correlated throughout the Pacific and most of the Atlantic, but not in the Indian Ocean. A lack of correlation or negative correlation characterized the MAR north of Iceland and in the equatorial Atlantic region. The DUPAL region of the south Atlantic and Indian Ocean is characterized by rather high $\Delta7/4$ throughout, but the ^{207}Pb/^{204}Pb ratios are generally lower in most of the Indian Ocean.

The $\Delta8/4$ signal (Figure 11) shows a clear division of the globe into geochemical provinces. High values (20-140) occur almost exclusively and extensively in the Indian Ocean west of the AAD and in the southern Atlantic south of 30°S, the classic DUPAL province (Hart, 1984). The very highest values are present near some hotspots in this area, particularly the Amsterdam hotspot, between the Marion and Crozet hotspots and between the Tristan and Bouvet hotspots. The other major province of high $\Delta8/4$ is formed by the Atlantic and Arctic ridges north of Iceland. Smaller and less pronounced domains with high $\Delta8/4$ are present at the Arctic and Atlantic ridges north of Iceland and the eastern Chile ridge. Outside these areas values above 10 are tied to hotspots, namely Ascension, Louisville, Galapagos, Baja, Azores and potentially Great Meteor. The remaining hotspots close to MORs do not show elevated $\Delta8/4$ values in their vicinities. Particularly low values (-30 to -60) occur in three "outlier" points in the central Reykjanes Ridge, at the Azores and at the northern end of the Easter microplate.

$\Delta\varepsilon$Hf (Figure 12) indicates the presence of SCLM with values >5 in the Atlantic north of Iceland, near the Azores and on the central Reykjanes Ridge. Negative $\Delta\varepsilon$Hf values hinting at a stronger influence

of ROC than SCLM are dominant in most of the Southern Hemisphere, i.e. the South Atlantic Ridge, the eastern and western ends of the SWIR, the eastern SEIR and most consistently in all the ridges of the Pacific.

Fractionation corrected Fe abundances indicate deeper melting and are usually correlated with a higher degree of melting. Fractionation corrected CaO/Al_2O_3 ratios (Figure 13) are correlated with the degree of melting (Jaques and Green, 1980; Niu and O'Hara, 2008) as well as the presence of a HIMU component (Jackson and Dasgupta, 2008). CaO/Al_2O_3 are elevated near hotspots and at the fast spreading East Pacific Rise, i.e. places where a relatively high degree of melting is expected.

The maxima, i.e. values higher than the background of the vast majority of points analyzed, of all REE ratios, exemplified by La/Sm (Figure 14) are in the vicinities of enrichment related to hotspots with the exception of the eastern part of the Chile Ridge and the central MAR at ca. 15°N.
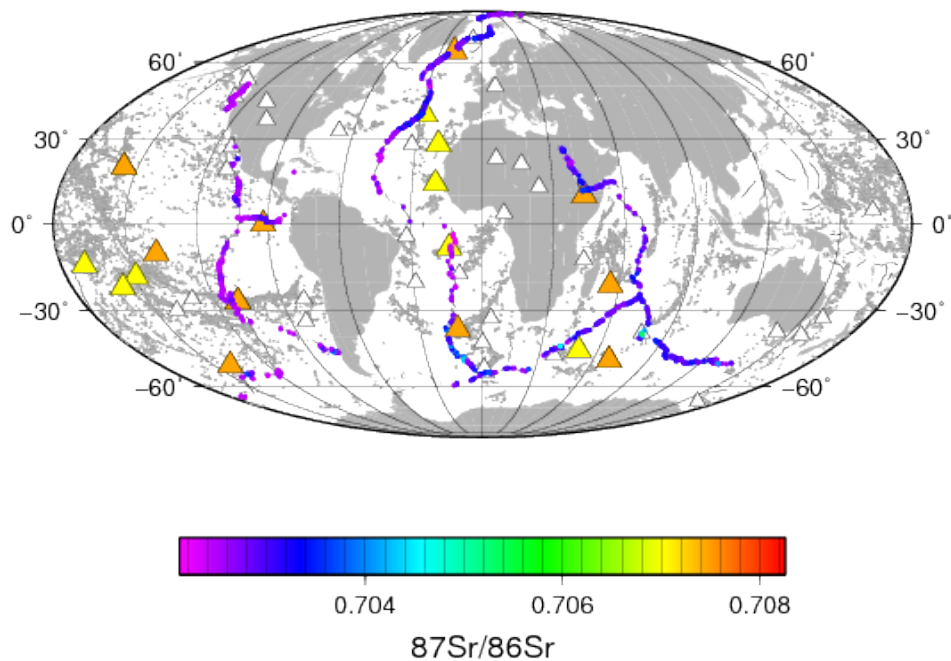
Figure 3: Global variation of $^{87}Sr/^{86}Sr$ in MORB. Hotspots and seamounts as in Figure 2.
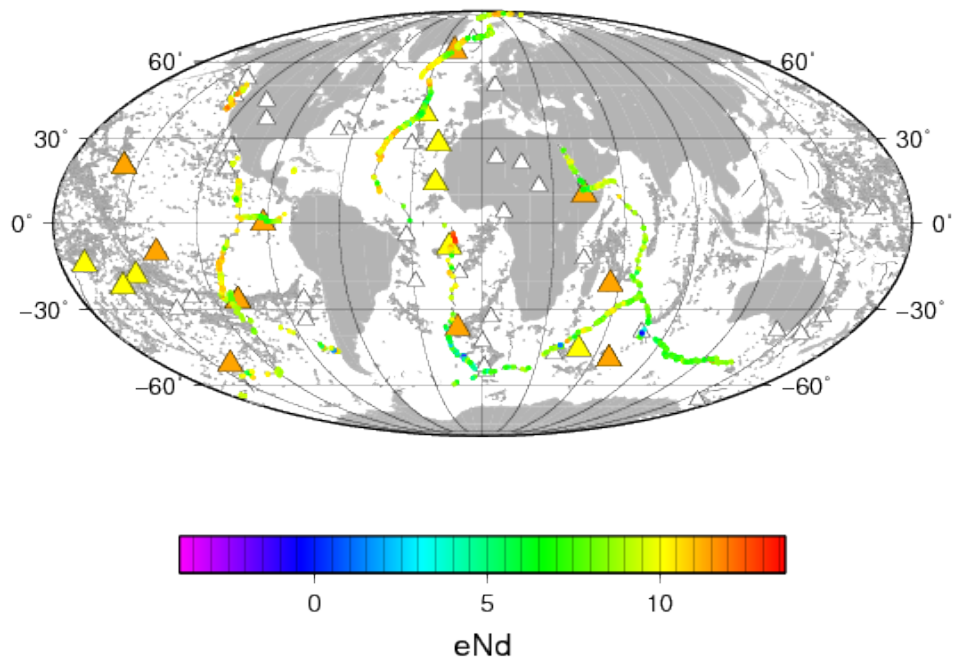
Figure 4: Global variation of ε_{Nd} in MORB. Hotspots and seamounts as in Figure 2.
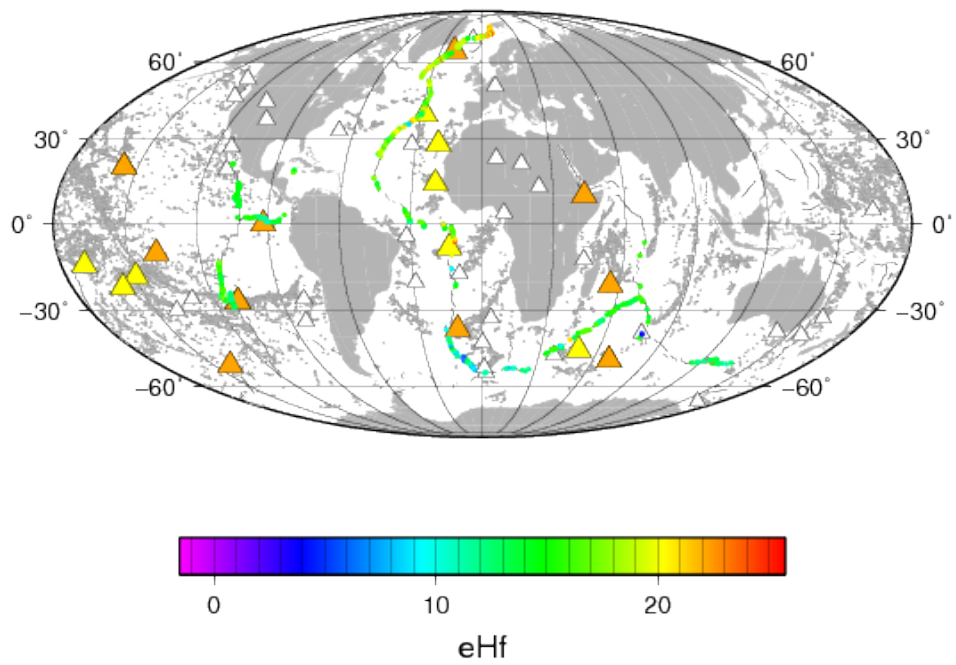
Figure 5: Global variation of ε_{Hf} in MORB. Hotspots and seamounts as in Figure 2.
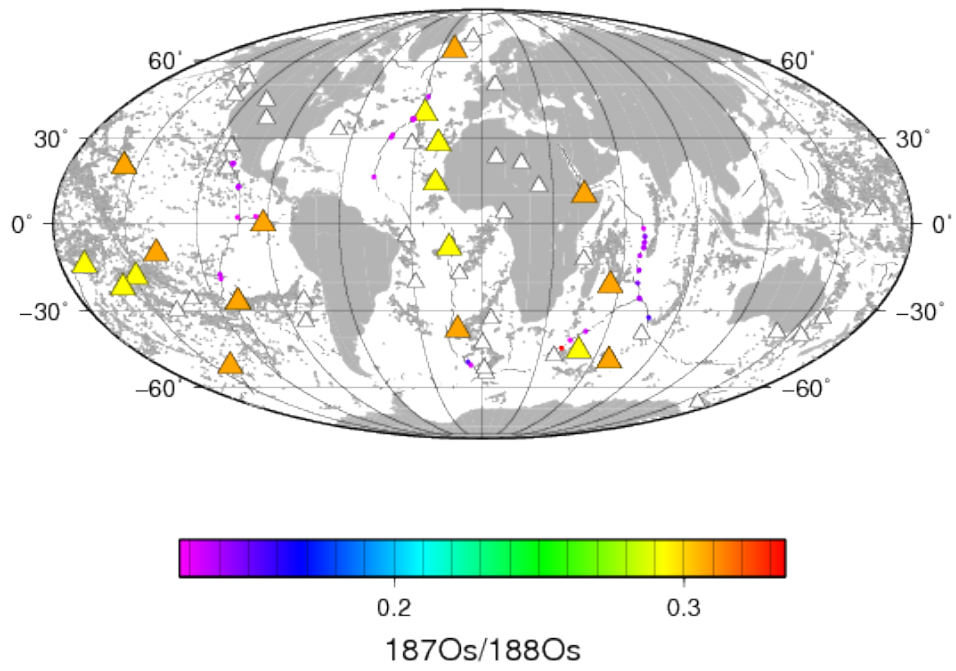
Figure 6: Global variation of $^{187}Os/^{188}Os$ in MORB. Hotspots and seamounts as in Figure 2.
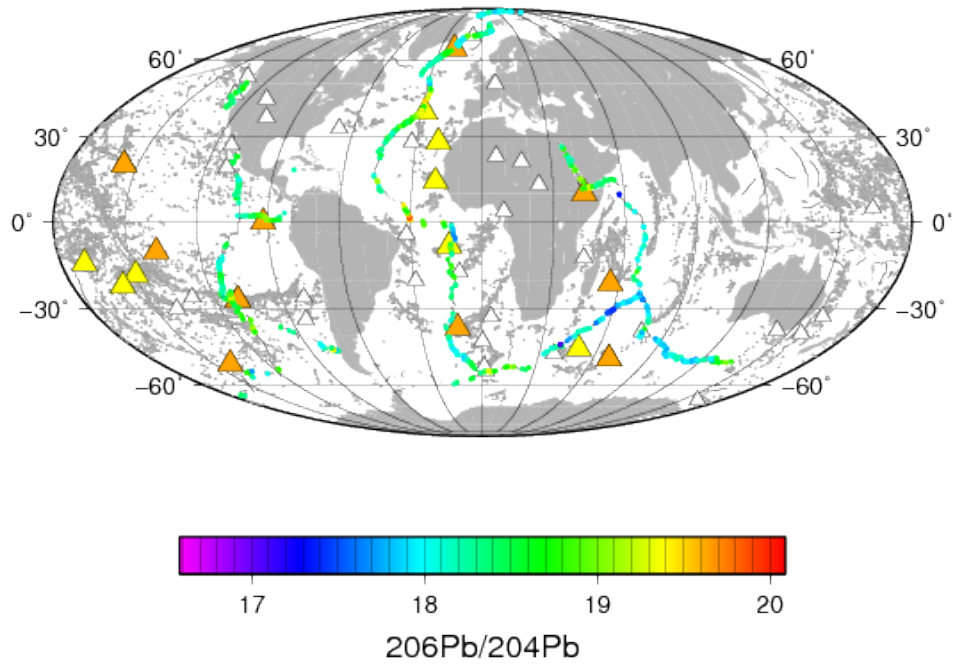
Figure 7: Global variation of $^{206}Pb/^{204}Pb$ in MORB. Hotspots and seamounts as in Figure 2.
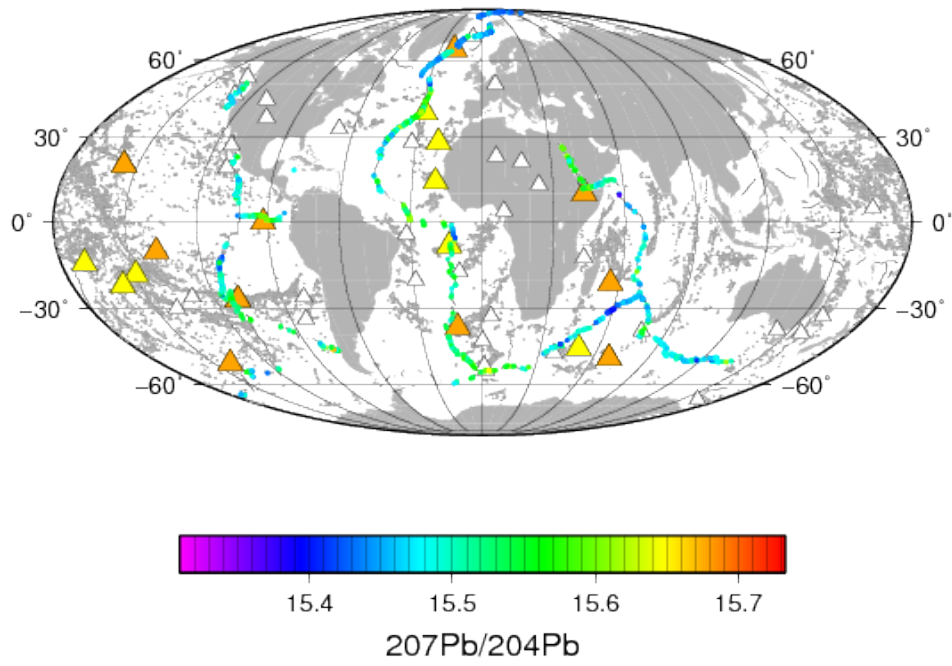
Figure 8: Global variation of [207]Pb/[204]Pb in MORB. Hotspots and seamounts as in Figure 2.
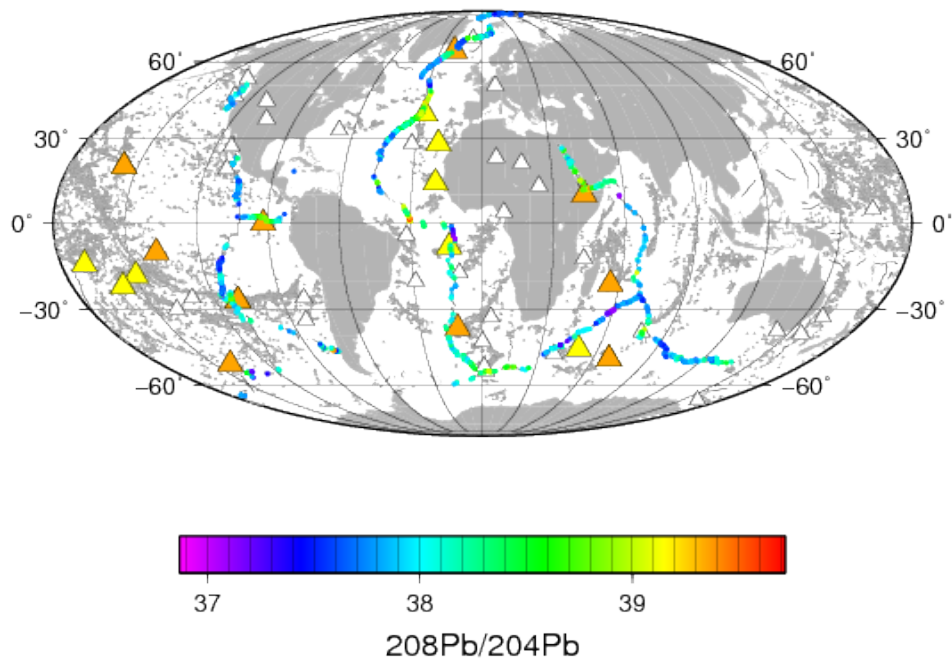
Figure 9: Global variation of [208]Pb/[204]Pb in MORB. Hotspots and seamounts as in Figure 2.
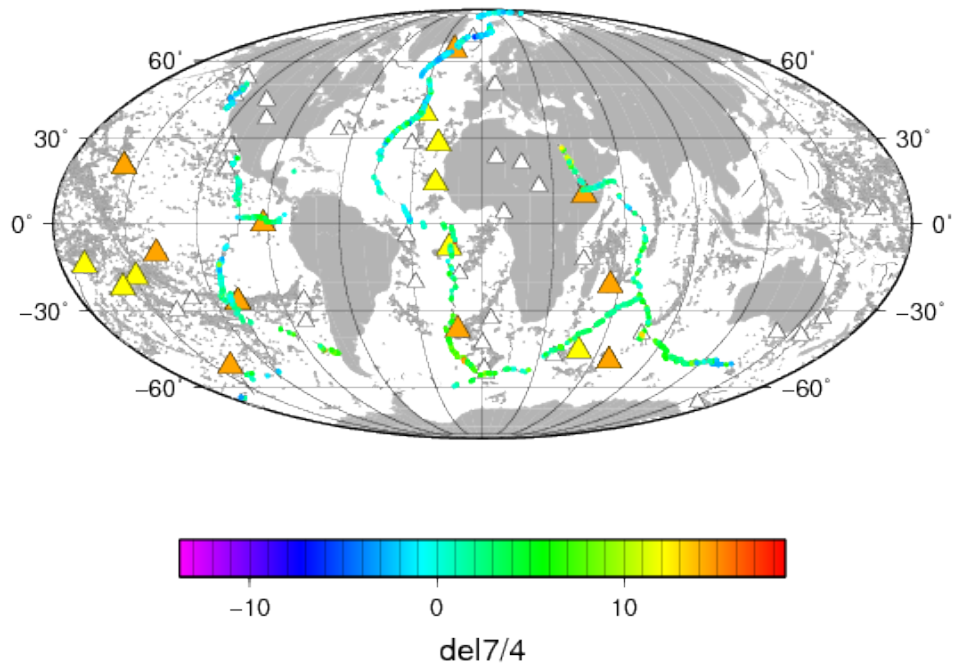
Figure 10: Global variation of Δ7/4 (Hart, 1984) in MORB. Hotspots and seamounts as in Figure 2.
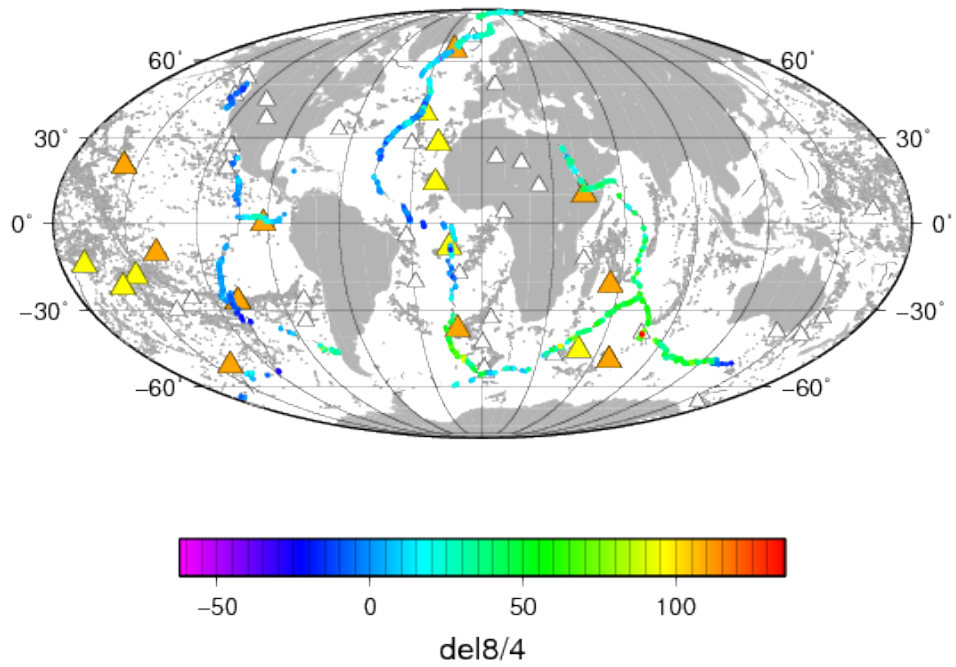
Figure 11: Global variation of Δ8/4 (Hart, 1984) in MORB. Hotspots and seamounts as in Figure 2.
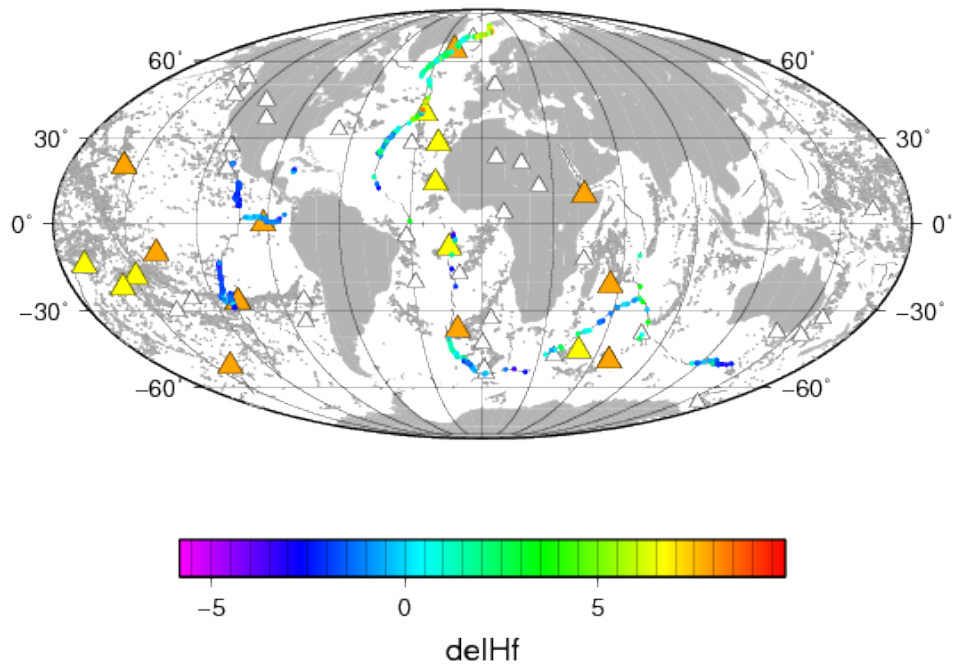
Figure 12: Global variation of ΔεHf (Andres et al., 2004) in MORB. Hotspots and seamounts as in Figure 2.
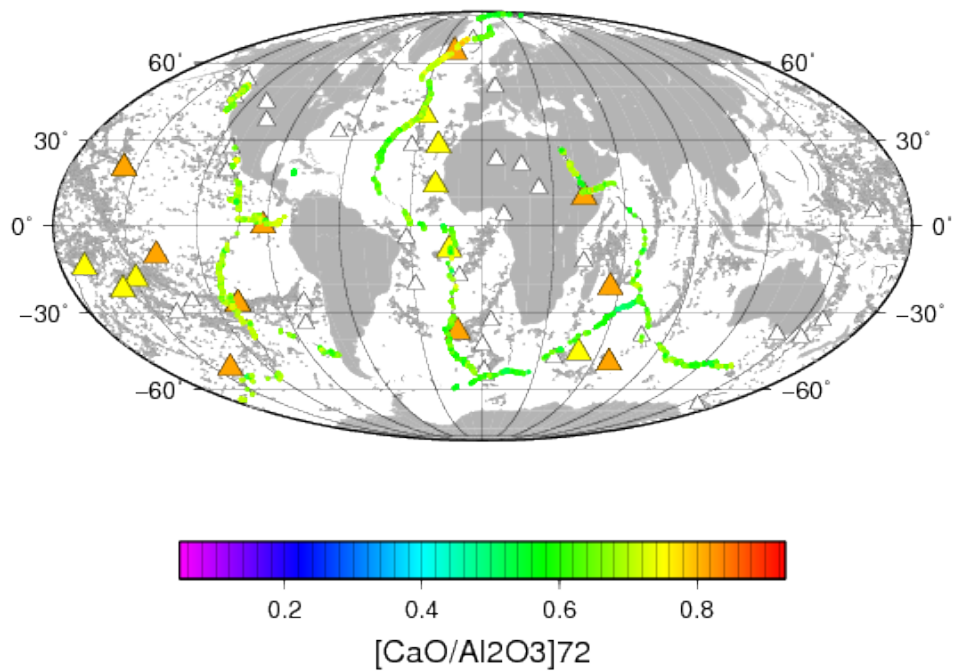
Figure 13: Global variation of fractionation corrected CaO/Al_2O_3 in MORB with fractionation correction to Mg#=72 according to the procedures of Niu and O'Hara (2008), a melt with Mg#=72 corresponds to a mantle residue olivine composition of $Fo_{89.6}$. Hotspots and seamounts as in Figure 2.
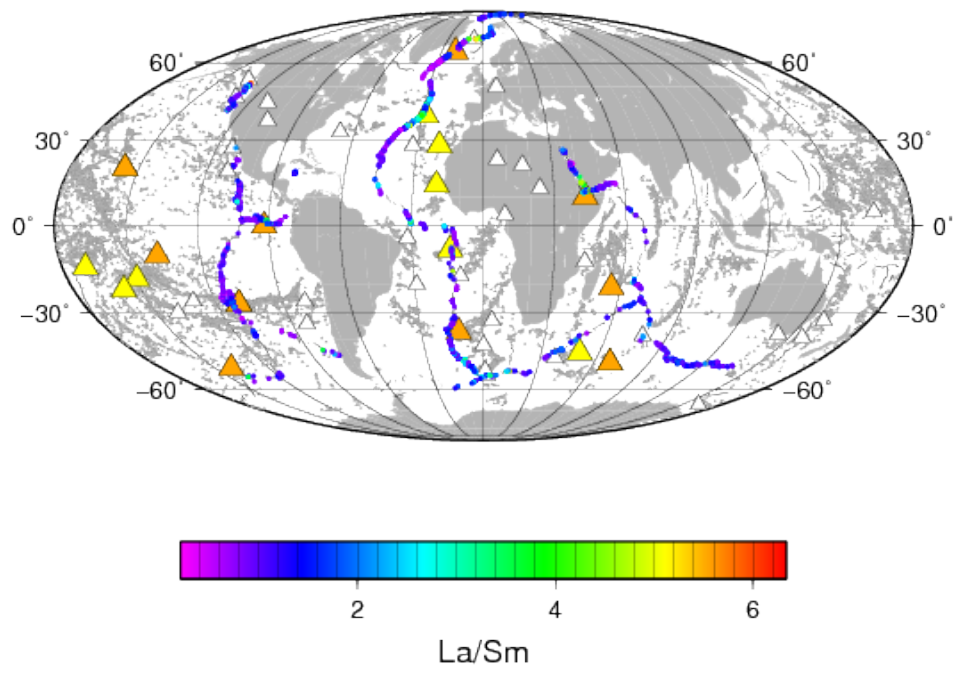
Figure 14: Global variation of La/Sm in MORB. Hotspots and seamounts as in Figure 2.

3.2. A discussion of main oceanic basins and mid ocean ridges

For the further discussion of the global data, five regions have been defined according to the ocean basins and geographical position: (1) the Arctic Ocean and the Atlantic north of Iceland, (2) the Atlantic south of Iceland, subdivided in two sections at the Equator by the Romanche Fracture Zone, (4) the Indian Ocean, subdivided into the Central Indian Ridge and its continuation until the Red Sea Rift, the South West Indian Ridge and the South East Indian Ridge, (3) the Pacific Ocean, subdivided into the East Pacific Rise, the Chile Ridge, the Galapagos Rise and the Juan de Fuca Ridge, as well as (5) the Caribbean Cayman trough. This categorization of the global MORB data has been used for a comparison of the major regions to establish a context for a more detailed regional and global discussion.

The following discussion focus on each of the main segments of the global oceanic ridge system: Atlantic and Arctic ridges north of Iceland, the Atlantic south of Iceland, the Southwest Indian Ridge (SWIR), the Southeast Indian Ridge (SEIR), the Central Indian Ridge (CIR) with its northwards continuation into the Red Sea and the East Pacific Rise (EPR) with branching ridges (Chile Ridge and Galapagos Ridge) as well as the Juan de Fuca Ridge (including the Gorda and Explorer Ridges). For each of the main segments fifteen-panel figures show the along-axis variation in ridge depth (D_R as negative elevation), crustal thickness (Th_C), gravity anomaly, $^{87}Sr/^{86}Sr$, ε_{Nd}, ε_{Hf}, $^{206}Pb/^{204}Pb$, $^{207}Pb/^{204}Pb$, $^{208}Pb/^{204}Pb$, $\Delta7/4$, $\Delta8/4$, $\Delta\varepsilon Hf$, Ca_{72}/Al_{72}, Fe_{72} and La/Sm. Additional figures show the $^{87}Sr/^{86}Sr$ versus $^{143}Nd/^{144}Nd$, $^{143}Nd/^{144}Nd$ versus $^{206}Pb/^{204}Pb$, and $\Delta\varepsilon Hf$ (Andres et al., 2004) versus $\Delta8/4$ (Hart, 1984).

High Ca_{72}/Al_{72}-ratios in MORB may be due to a combination of high degree of partial melting (see the parameterization of experimental data by Niu and O'Hara, 2008) and high proportion of the enriched HIMU-component relative to the EM-components (Jackson and Dasgupta, 2008). High Fe_{72}-values (for a given source composition) generally indicates a high average melting pressure, i.e. high potential temperature, large degree of melting and large vertical melting column (Niu and O'Hara, 2008). Variations in the mantle potential temperature and resulting melt productivity causes a strong inverse correlation between ridge depth and crustal thickness along nearly all the MOR segments. The gravity anomaly is also positively correlated with the ridge depth. Only the crustal thickness variation is therefore discussed for each of the ridge segments below. The same applies for the major element compositions, which can be correlated to the waterdepth.

A further discussion of major and minor element variation will follow in the global geochemical discussion (Section 4). Separate collections of regional maps and additional figures are presented in the appendix and variably discussed in the main text.

3.2.1. Arctic and Atlantic ridge system north of Iceland

Figure 15 shows the along-axis crustal thickness and geochemical variations for the Atlantic and Arctic ridges north of Iceland (Kolbeinsey, Mohns, Knipovich and Gakkel Ridges). The Gakkel Ridge is divided into western (83-85 N) and eastern (85-87 N) segments separated by the Sparsely Magmatic Zone (SMZ) near 85 N (e.g. Michael et al., 2003; Goldstein et al., 2008). The crustal thickness decreases from a maximum of about 20 km along the southern part of the Kolbeinsey Ridge to less than 10 km along the northern part. A further abrupt drop to about 5 km occurs at the JMFZ, followed by increasing thickness northwards to about 8 km along the southern Mohns Ridge. Further north, the depths vary mostly between 5 and 7 km, with almost no crust in the SMZ separating the western and eastern Gakkel Ridge (Michael et al., 2003; Goldstein et al., 2008). The changes in ridge orientation, fracture zones, spreading dynamics and mantle flow field may largely explain the geophysical and geochemical variations.

The western and eastern Jan Mayen Fracture Zones represent a geochemical divide between high-degree melts from depleted source regions along the Kolbeinsey Ridge and enriched low-degree melts at Jan Mayen and along the southernmost part of the Mohns ridge. The Sr-Nd-Pb-isotope and La/Sm ratios will commonly serve as indicators of the degree of enrichment (proportions of enriched versus refractory melt components). An interesting observation regarding the NE Atlantic and Arctic ridge system is the partial decoupling of the La/Sm ratio from the Sr-Nd-Pb-isotope ratios. The La/Sm ratio indicates the strongest melt depletion along the Kolbeinsey Ridge and almost similar level of depletion along the western Gakkel Ridge (83-85 N). In contrast, the Sr-Nd-Pb-isotopes indicate stronger melt depletion along the eastern than the western (85-87 N) Gakkel Ridge. This may be related to an old, strongly melt-depleted and re-enriched SCLM along the western Gakkel Ridge (e.g. Goldstein et al., 2008). The MORB compositions are less refractory along the Mohns and Knipovich Ridges and become more enriched southwards to merge compositionally with the basalts at the Jan Mayen platform and island.

The Arctic and Atlantic ridges north of Iceland are characterized by ultra-slow and slow spreading, respectively. The full spreading rate decreases from 14.6 to 6.3 mm/a from west to east along the Gakkel Ridge, which is also characterized by abundant hydrothermal activity (Michael et al., 2003). Sufficient time for hydrothermal and conductive cooling, in combination with locally refractory asthenospheric source compositions may explain the abnormally thin crust, that largely vanishes within the SMZ. The northernmost narrow Knipovich basin (Lena Trough) between Spitsbergen-Yermak plateau and NE Greenland has highly oblique spreading (dextral movement). The strong melt enrichment along the southernmost Mohns Ridge towards the island of Jan Mayen may be explained by the fact that the lateral northeastward mantle flow from the Iceland plume (e.g. Jones et al., 2002; Breivik et al., 2006) does not experience significant melting until it is pulled upwards in the weak

extensional regime of the western JMFZ and southern tip of the Mohns Ridge. In contrast, the Kolbeinsey Ridge lies approximately along the northward extension of the Northern Rift Zone (NRZ) in Iceland, in spite of minor offset by the Tjørnes Fracture Zone. The NRZ and therefore the downstream-positioned Kolbeinsey Ridge is characterized by extensive melting into highly refractory (lower) mantle source components. Studies of multiple isotopic systems (Os, He, Sr and Nd) in basalts from the Icelandic volcanic flank zones and from Jan Mayen Island (Debaille et al., 2009) have found a positive correlation between $^{143}Nd/^{144}Nd$ and $^{187}Os/^{188}Os$ and further strengthen the evidence for the presence of recycled plume-related SCLM enriched in incompatible trace elements. This links the enrichment in the Jan Mayen area to the Iceland plume by lateral movement of plume material leading to partial melting in the tectonic regime of the Jan Mayen Fracture Zone. According to Debaille et al. (2009) the melt compositions of the area can be explained with binary mixing of two mantle sources; One being detached SCLM from the opening of the Atlantic Ocean (low, unradiogenic $^{187}Os/^{188}Os$ and $^{143}Nd/^{144}Nd$, low 3He/4He and high 87Sr/86Sr) and the other being a mixture of depleted upper mantle material with plume material containing recycled oceanic crust and depleted lower mantle material (high $^{187}Os/^{188}Os$, $^{143}Nd/^{144}Nd$ and $^{3}He/^{4}He$ with low $^{87}Sr/^{86}Sr$).

The regionally variation in MORB compositions north of Iceland are probably partly due to regional distribution of more than one enriched component in the asthenospheric mantle source, in addition to the general variation in the proportion of enriched versus refractory melt components. The ratio of $\Delta8/4$ to $\Delta7/4$ is especially high along the western Gakkel Ridge, compared to the eastern Gakkel Ridge and Kolbeinsey Ridge. This ratio is relatively high also in the Mohns and Knipovich Ridges. The western Gakkel Ridge has therefore been described as "DUPAL like" after the characteristics defined by Hart (1984) (i.e. $\Delta8/4>30$; compare Section 4). The low $\Delta7/4$ ratios in the Arctic suggest either a young enrichment age of the anomaly as discussed by Goldstein et al. (2008) or an early depletion of the source. The latter is strongly suggested by Os isotope data which indicates depletion ages of up to 2 Ga (Liu et al., 2008). Hf-data is not available for the Gakkel Ridge. The $\Delta\epsilon Hf$-values, however, are much higher in the Mohns and Knipovich Ridges, compared to the Kolbeinsey Ridge indicating a larger contribution of ROC as opposed to SCLM for the Kolbeinsey Ridge.
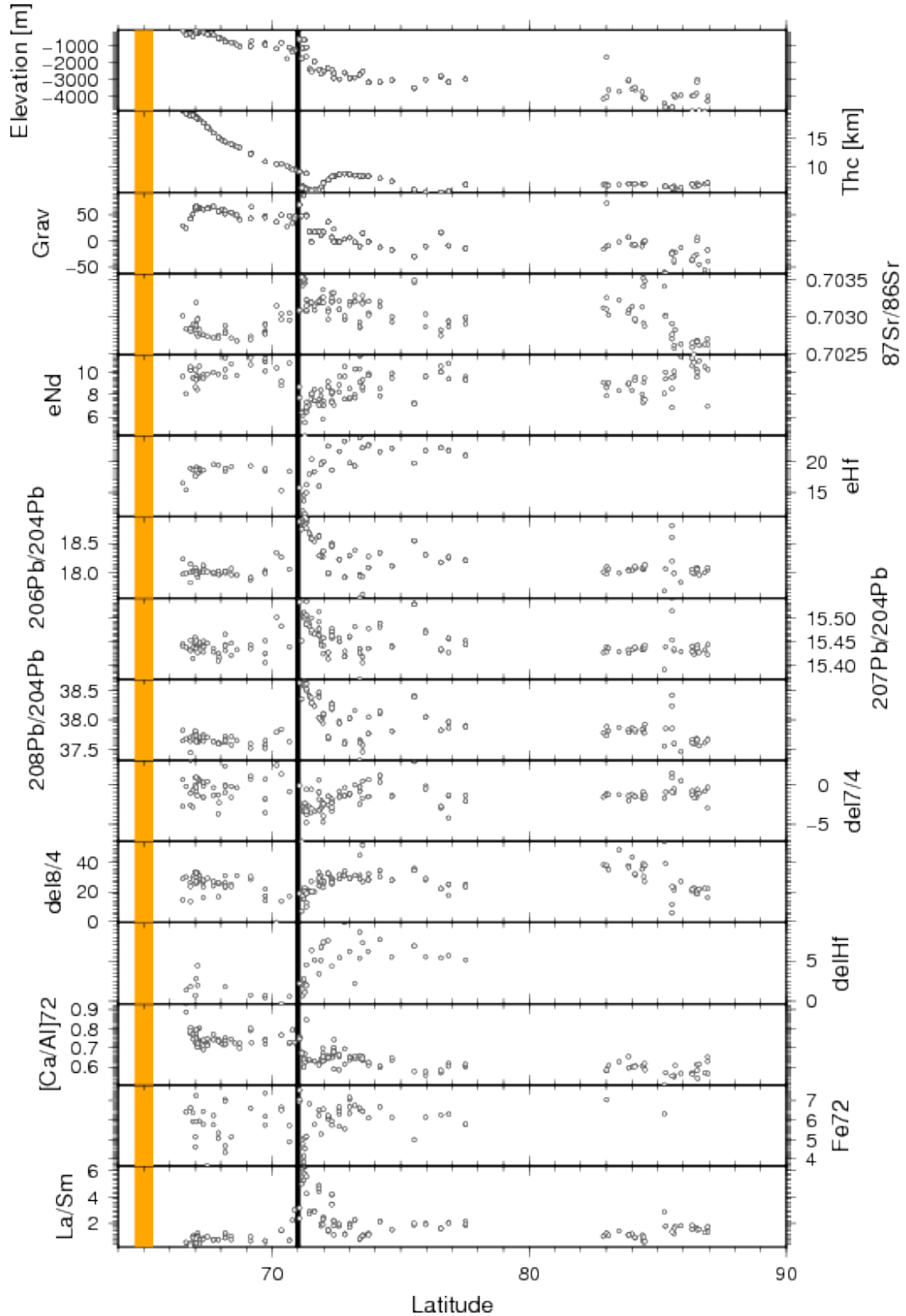
Figure 15: Along axis variation for the Atlantic and Arctic ridge system north of Iceland, showing ridge depth (elevation), crustal thickness (Th_C), gravity anomaly (Grav in mGal), $^{87}Sr/^{86}Sr$, ε_{Nd}, ε_{Hf}, $^{206}Pb/^{204}Pb$, $^{207}Pb/^{204}Pb$, $^{208}Pb/^{204}Pb$, $\Delta 7/4$ and $\Delta 8/4$ (Hart, 1984), $\Delta\varepsilon Hf$ (Andres et al., 2004), Ca_{72}/Al_{72}, Fe_{72} and La/Sm. The Ca_{72}/Al_{72} and Fe_{72} (labeled "[Ca/Al]72"and "Fe72" are the ratio CaO/Al_2O_3 and total Fe as FeO, recalculated to equilibrium with a melt composition with Mg# (=100Fe/(Mg+Fe), atom basis) of 72, according to the procedures of Niu and O'Hara (2008), a melt with Mg#=72 corresponds to a mantle residue olivine composition of $Fo_{89.6}$. Vertical bars mark hotspots in the vicinities of the ridge colored according to Fig. 2; from left to right: Iceland, Jan Mayen.
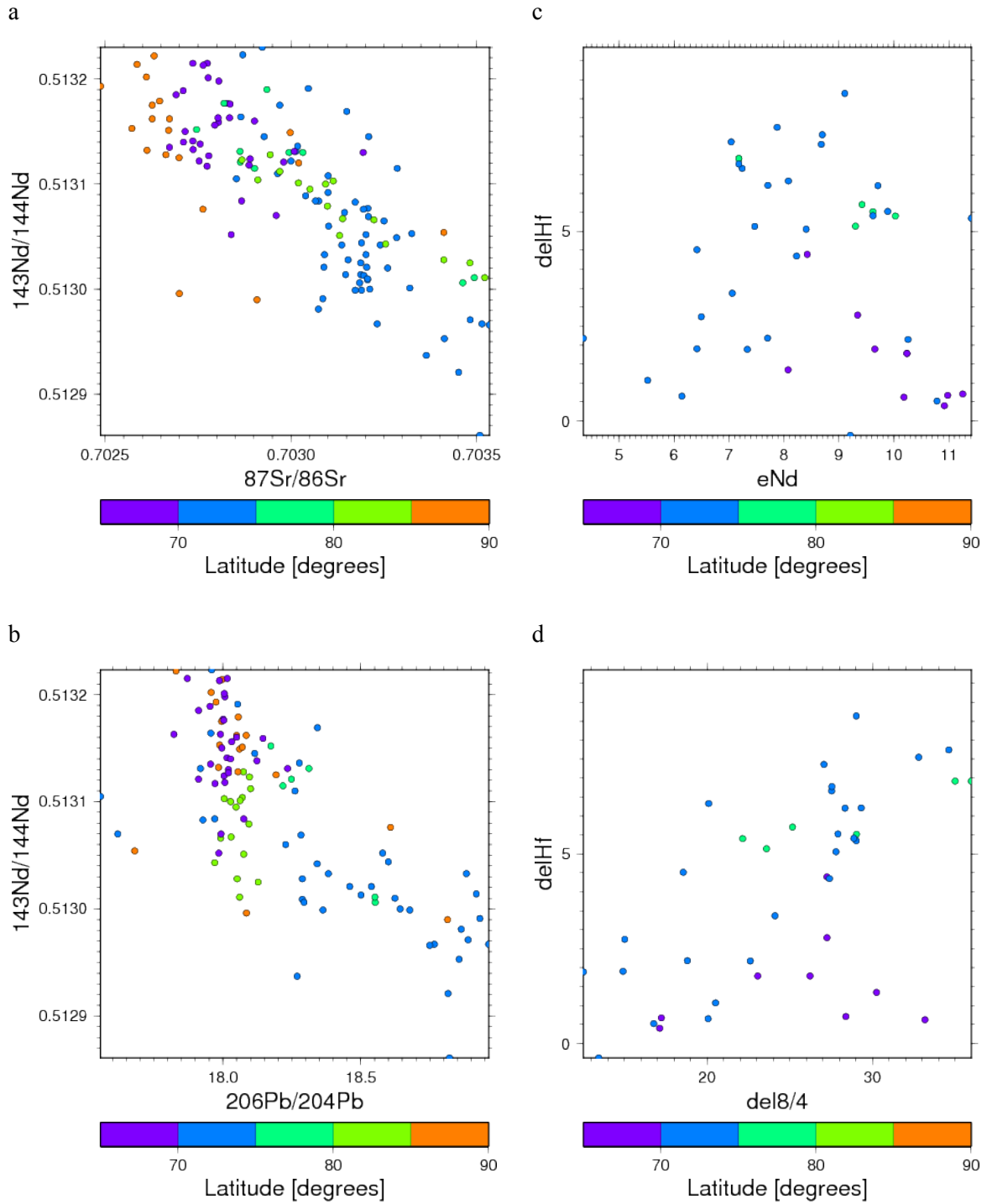
Figure 16: (a) $^{143}Nd/^{144}Nd$-$^{87}Sr/^{86}Sr$, (b) $^{143}Nd/^{144}Nd$-$^{206}Pb/^{204}Pb$, (c) $\Delta\epsilon Hf$-ϵNd and (d) $\Delta\epsilon Hf$- $\Delta 8/4$ plots for MORB of the Arctic and Atlantic ridge system north of Iceland.

The Sr and Nd isotope ratios show an anticorrelation with wide arrays of compositions occurring between 70°N and 85°N while the areas closest to Iceland and the North Pole mostly show high $^{143}Nd/^{144}Nd$ and low $^{87}Sr/^{86}Sr$ (Figure 16a).

Similarly to the $^{143}Nd/^{144}Nd$ - $^{87}Sr/^{86}Sr$ plot the isotopic signal in the $^{143}Nd/^{144}Nd$-$^{206}Pb/^{204}Pb$ space forms a roughly anticorrelated trend and is much more confined (high 143Nd/144Nd- low $^{206}Pb/^{204}Pb$) close to Iceland (65-70°N) and the eastern part of the Gakkel Ridge while the area close to Jan Mayen (70-75°N) shows a wide spread (Figure 16b). The western part of the Gakkel Ridge (80-85°N) and to a lesser extent the Kolbeinsey Ridge (65-70°N) do not follow the regional anticorrelated trend, but vary in $^{143}Nd/^{144}Nd$ at relatively constant low $^{206}Pb/^{204}Pb$.

The ε_{Nd}-$\Delta\varepsilon Hf$ signal of the Arctic shows two different trends: One of an anticorrelation near Jan Mayen and one of correlation for the other areas. Both trends are within an array of $\Delta\varepsilon Hf$=0-10 and ε_{Nd}=5-11 (Figure 19c). Samples from the southernmost MAR cover a wider span of ε_{Nd} ratios and resemble more the Indian Ocean signature (Figure 23c) with lower enriched compositions, whereas the northern segments of the ridge have higher ε_{Nd} ratios (5-15) for varying $\Delta\varepsilon Hf$.

$\Delta 8/4$ and ε_{Hf} show a linear regional correlation trend and the widest spread, covering the range of all other regional samples, in the area close to Jan Mayen (70-75°N). The Kolbeinsey Ridge (65-70°N) and the Knipovich Ridge (75-80°N) do not follow the general linear trend, but show large variations in $\Delta 8/4$ at a small range of ε_{Hf} and unlike the Jan Mayen related samples they show a slight anticorrelation of $\Delta 8/4$ and ε_{Hf}. $\Delta 8/4$ and $\Delta\varepsilon Hf$ show a very similar picture, the major difference being the Kolbeinsey Ridge (65-70°N) that incorporates higher $\Delta 8/4$ values at low $\Delta\varepsilon Hf$ and thus does not lie within the general linear trend. The high $\Delta 8/4$ values coexisting with high $\Delta\varepsilon Hf$ values (>5) of the Mohns and Knipovich with extreme values (9 to 10) occurring on the northern Mohns Ridge indicate the presence of SCLM in the Arctic-Atlantic upper mantle north of Jan Mayen (Figure 16d). The linear correlation between $\Delta 8/4$ values and $\Delta\varepsilon Hf$ suggests a mixing between SCLM and ROC as discussed by Debaille et al. (2009). The more enriched MORB from the close vicinity of Jan Mayen and the more depleted Kolbeinsey ridge both show a different signature with lower $\Delta\varepsilon Hf$ (-1 to 5) and a wide spread of $\Delta 8/4$. This signature is related to the Iceland plume.

3.2.2.   Mid-Atlantic Ridge south of Iceland

Mid-Atlantic Ridge south of Iceland till Romanche FZ 5°N

Fig. 17 shows the along-axis crustal thickness and geochemical variations for the MAR south of Iceland (North MAR including Reykjanes Ridge). The Gibbs FZ (53°N) separates the Reykjanes Ridge and the more southern segments of the MAR, which in turn are divided in a northern and a southern part by the Azores (38-39°N). The crustal thickness decreases from a maximum of ca. 17 km on the northern Reykjanes Ridge to between 10 and 12 km for its central part. The southern Reykjanes Ridge shows a further thinning of the crust towards ca. 7 km at its southernmost end. The MAR

between 52°N and 5°N has a very homogeneous crustal thickness of ca. 7 km, the only exception being the area around the Azores (37-42°N) where thicker crust with up to ca. 10 km thickness (38-40°N) occurs. The variations in crustal thickness, ridge depth and gravity anomaly as well as the geochemical variations are strongly tied to the presence of the Iceland and Azores hotspots.

The Sr, Nd and Pb isotopes as well as the La/Sm ratio indicate a decrease of enrichment on the Reykjanes Ridge with increasing distance from Iceland towards a minimum of enrichment at 50°N. Iceland as a hotspot does not show much enrichment in Pb, Nd and Sr isotopes or in REE ratios when compared to other hotspots (e.g. the Azores) and closer to the hotspot this signature becomes increasingly weak. This is due to the effect of dilution of the enriched components by a high degree of melting related to the production of large melt volumina (compare Appendix 1 and Dalton et al., 2014). Further south towards the Azores the MORB composition becomes increasingly enriched, reaching a maximum at ca. 42°N at the onset of the crustal thickening related to the Azores, at the Azores (ca. 39°N), directly south of the Azores (ca. 37°N) and at the southern onset of the crustal thickening at ca. 35°N. These maxima of enrichment all have stronger signatures than the northern Reykjanes Ridge where more depleted material is melted. South of the Azores the MORB is generally more depleted again. Nevertheless between 23 and 35°N the isotopic signal has a relatively high bandwidth. Between 30 and 40°N the Hf isotopic ratios untypically correlate to the general trend of the Pb and Sr isotopes instead of the usual Nd isotopes. At ca. 14°N isolated enriched isotope and REE ratios are present and possibly relates to a plume below the MAR at 15-25°N as discussed by Montelli et al. (2006).

$\Delta\varepsilon$Hf and $\Delta8/4$ are high at the northern and southern end of the crustal thickening of the Azores and suggest a potential presence of continental material, whereas low values are present at the Azores themselves are indicating a different source composition with a stronger influence of recycled material such as ROC.

The melt sensitive fractionation corrected Fe abundance and Ca/Al ratio follow the general pattern and indicate higher degrees of melting at the enriched points.
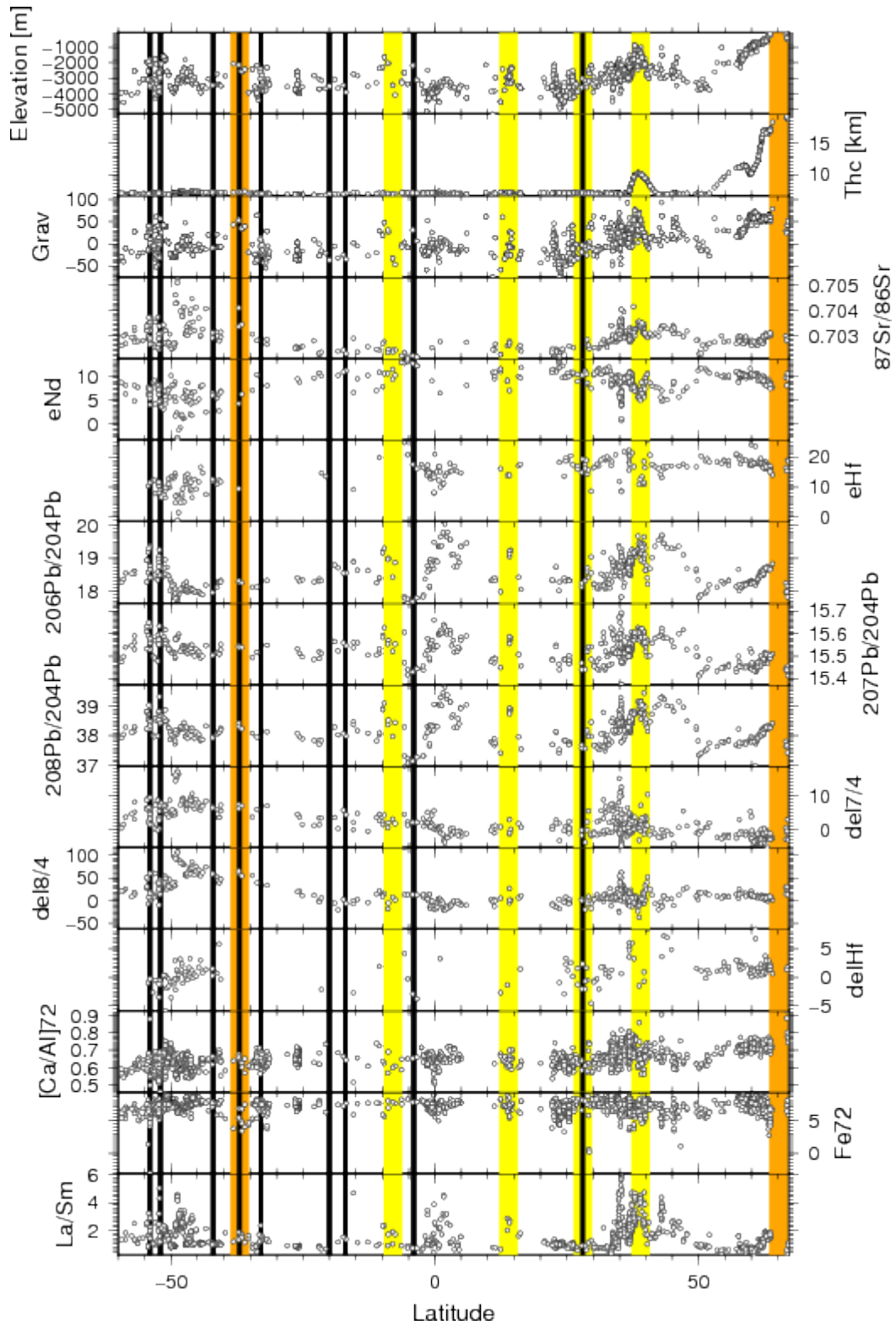
Figure 17: Along axis variation for the Atlantic ridge system south of Iceland. Marked hotspots (left to right) are Bouvet, Meteor, Discovery, Tristan, Vema, Trinidade, St. Helena, Ascension, Fernando, Cape Verde, Great Meteor, Canary, Azores and Iceland. Further explanations in Fig. 14.
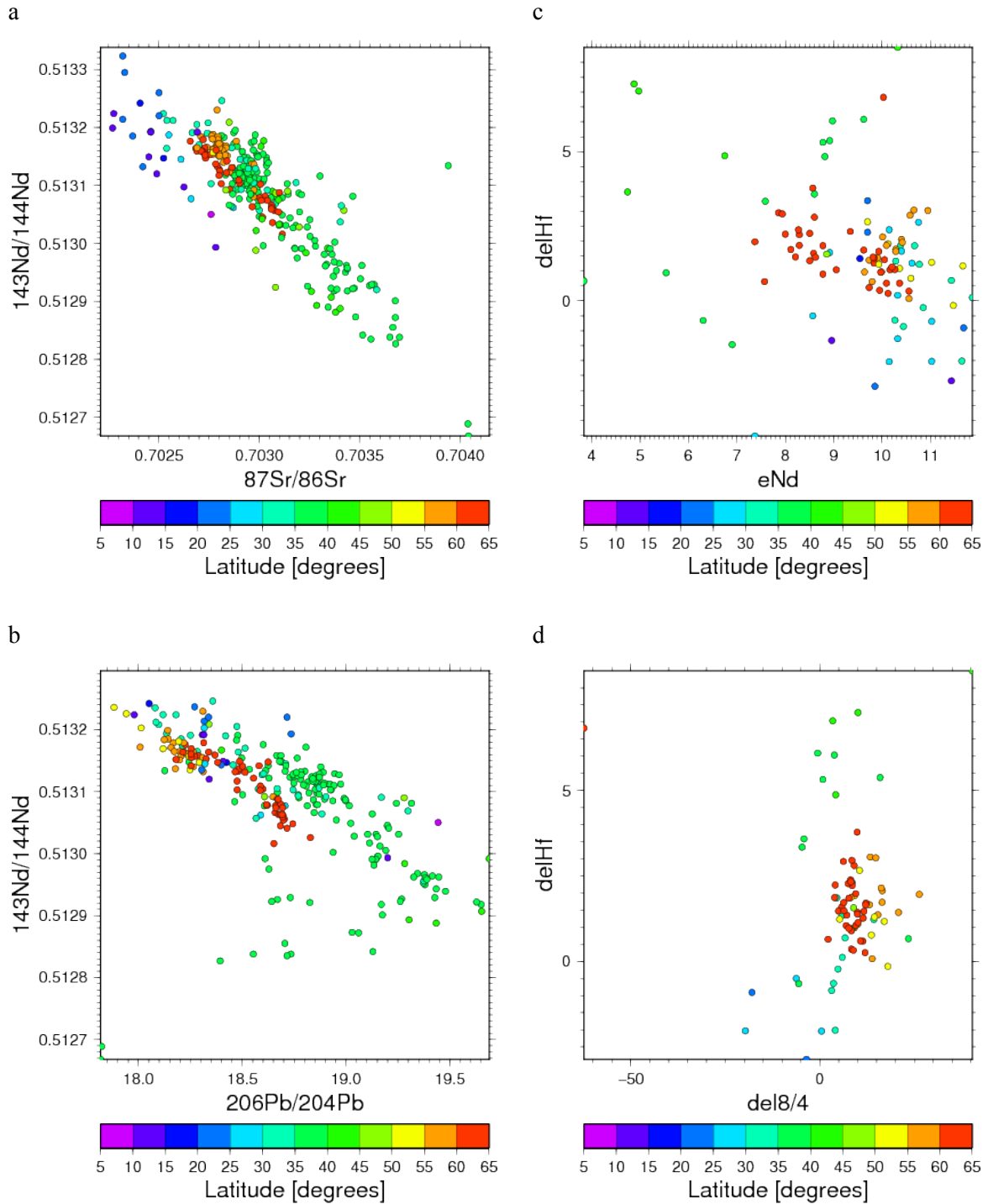
Figure 18: (a) $^{143}Nd/^{144}Nd-^{87}Sr/^{86}Sr$, (b) $^{143}Nd/^{144}Nd-^{206}Pb/^{204}Pb$, (c) $\Delta\varepsilon Hf-\varepsilon_{Nd}$ and (d) $\Delta\varepsilon Hf- \Delta 8/4$ plots for MORB of the Mid-Atlantic Ridge south of Iceland till Romanche FZ 5°N.

The Sr and Nd isotope ratios (Figure 18a) show a general anticorrelation with different areas covering distinct arrays. The widest range including the lowest $^{143}Nd/^{144}Nd$ and highest $^{87}Sr/^{86}Sr$ of the region is present in the area influenced by the Azores hotspot (30-45°N) while the most confined cluster, overlapping with the high $^{143}Nd/^{144}Nd$ and low $^{87}Sr/^{86}Sr$ of the Azores area, represents the Reykjanes Ridge (50-65°N). The southernmost segment of this region (5-25°N) is characterized by the highest

42

^{143}Nd/^{144}Nd and lowest ^{87}Sr/^{86}Sr and does not show almost any overlap with the signatures of the other parts of the region.

^{143}Nd/^{144}Nd-^{206}Pb/^{204}Pb (Figure 18b) shows a very similar picture to the ^{143}Nd/^{144}Nd - ^{87}Sr/^{86}Sr plot with a generally anticorrelated trend and the largest spread near the Azores hotspot (30-45°N). Differently from the latter diagram, here the signal of the southernmost area (5-25°N) is very similar to the one of the Reykjanes Ridge (50-65°N) and the Azores area (30-45°N) shows a "triangular" distribution of compositions indicating three endmembers (high ^{143}Nd/^{144}Nd- low ^{206}Pb/^{204}Pb, low ^{143}Nd/^{144}Nd- low ^{206}Pb/^{204}Pb and intermediate ^{143}Nd/^{144}Nd- high 206Pb/204Pb) contributing to its range.

The ε_{Nd}-$\Delta\varepsilon$Hf signal shows general trend of an anticorrelation with most samples being in an array of $\Delta\varepsilon$Hf=0-5 and ε_{Nd}=5-11, except for the Azores area which has a wide spread of the datapoints (Figure 18c). This low $\Delta\varepsilon$Hf signature indicates the presence of a ROC like component.

Δ8/4 and $\Delta\varepsilon$Hf (Figure 18d) show a linear correlation trend, although the different ridge segments are being separated by their $\Delta\varepsilon$Hf values, but not Δ8/4. The area under the influence of the Azores hotspot (30-45°N) shows the highest range of $\Delta\varepsilon$Hf in the region (-2-8), the Reykjanes Ridge (50-65°N) shows intermediate values and the southern areas (south of 30°N) show low $\Delta\varepsilon$Hf. One exception from the rule is a single data point with extremely low Δ8/4 and high $\Delta\varepsilon$Hf from the Reykjanes Ridge.

South Atlantic Ridge and American Antarctic Ridge

Figure 17 shows the along-axis bathymetry, crustal thickness, gravity anomaly and geochemical variations for the South Atlantic Ridge (south of Romanche FZ, 5°N) and the American Antarctic Ridge (AAR). This area is strongly influenced by numerous hotspots, most importantly Ascension (8°S), St. Helena (17°S), Tristan (37°S), Meteor (52°S) and Bouvet hotspots (54°S), relatively near to the ridges that mark the different ridge segments. To the south-west of the Bouvet triple junction (54°S) lies the AAR. Although there is some variability in the depth of the ridge and the gravity anomaly, the variation of the crustal thickness (6.6 to 7.2 km) is minimal in this region. It still reflects the general pattern of enrichment and plume related flow.

The MAR between the Tristan and Ascension Hotspots represents one of the major geochemical boundaries of the global MORB signal. The Sr and Nd isotope ratios and the Pb isotope signal show a characteristic decoupling in the Southern Atlantic with e.g. high Pb isotope ratios, generally indicating enrichment, coexisting with depleted Sr and Nd isotope ratios and vice versa. This specific signature is particularly pronounced at the Ascension hotspot which is depleted in Sr and Nd isotopes and has

mostly low Δ7/4 and Δ8/4 as well as at the otherwise strongly enriched segment at 48°S shows low depleted Pb isotope ratios, related to a low μ source such as LCC or SCLM. The strongly enriched segment at 48°S is related to higher crustal thickness likely to indicate stronger enrichment by plume flux. The origin of these signatures could be the incorporation of lower continental and subcontinental material in the upwelling mantle (Meyzen et al., 2007; Class and Le Roex, 2011). La/Sm and the Pb isotope signal are well correlated and indicate enrichment at hotspots.

The mixing of several components differing in their history of depletion and enrichment is also visible in the variation pattern of Δ7/4, Δ8/4 and ΔεHf. Δ8/4 increases from north to south on the MAR south of 20°S, reaching the highest regional values (ca. 100) of the Southern Atlantic DUPAL signature (further discussion in Section 4) between 45 and 50°S and decreasing again further south (particularly on the AAR). Positive ΔεHf values are present south of the Tristan hotspot and near Ascension and hint at the presence of a depleted, possibly SCLM like, component that can either be attributed to shallow detached or most likely deeply recycled material.
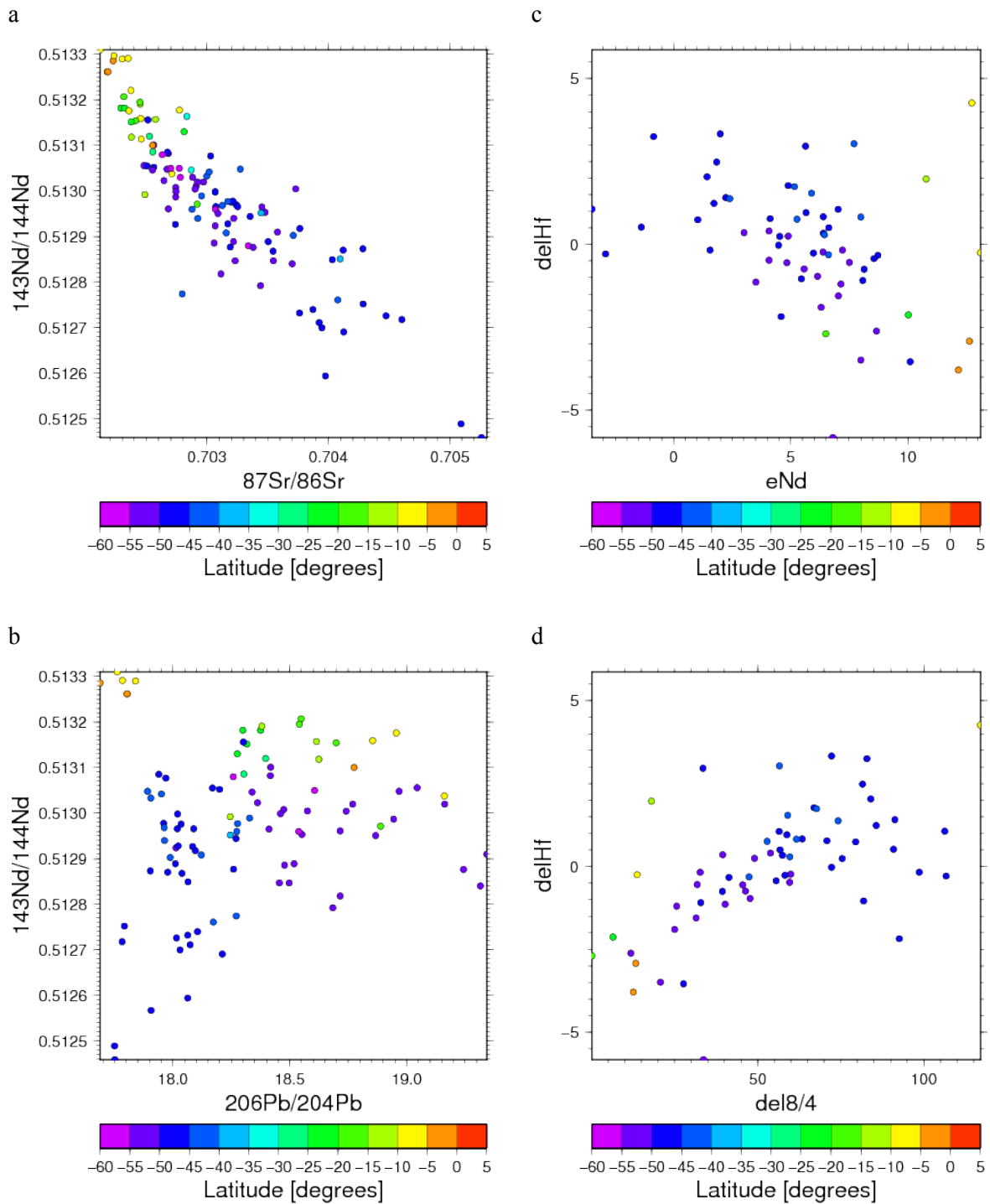
Figure 19: (a) ^{143}Nd/^{144}Nd-^{87}Sr/^{86}Sr, (b) ^{143}Nd/^{144}Nd-^{206}Pb/^{204}Pb, (c) ΔεHf-ε$_{Nd}$ and (d) ΔεHf- Δ8/4 plots for MORB of the South Atlantic Ridge and American Antarctic Ridge.

The Sr and Nd isotope ratios (Figure 19a) show a general anticorrelation with different areas covering distinct arrays. The widest range including the lowest ^{143}Nd/^{144}Nd and highest ^{87}Sr/^{86}Sr of the region is present in the southernmost Atlantic (40-50°S) while the highest ^{143}Nd/^{144}Nd and lowest ^{87}Sr/^{86}Sr ratios of the area are present directly north of the Ascension hotspot (5-10°S) and to a lesser degree in the wider area around Ascension (10-30°S).

The $^{143}Nd/^{144}Nd$-$^{206}Pb/^{204}Pb$ isotope diagram (Figure 19b) makes a similar tendency visible as the $^{143}Nd/^{144}Nd$ - $^{87}Sr/^{86}Sr$ plot with the largest spread in the southernmost MAR (40-55°S). A generally anticorrelated trend is formed except for the low $^{143}Nd/^{144}Nd$ area in the southern Atlantic (40-50°S). In this area, similar to the Azores area (30-45°N), a low $^{143}Nd/^{144}Nd$- low $^{206}Pb/^{204}Pb$ component is a major influence resulting in a "triangular" distribution of the overall compositions and a locally large spread in $^{143}Nd/^{144}Nd$ at $^{206}Pb/^{204}Pb$=17.7-18.4 with a possible linear correlation.

The ε_{Nd}-$\Delta\varepsilon Hf$ signal shows a general trend of an anticorrelation with most samples being in an array of $\Delta\varepsilon Hf$=0-10 and ε_{Nd}=5-11 (Figure 19c). Samples from the southernmost MAR cover a wider span of ε_{Nd} ratios and resemble more the Indian Ocean signature (Figure 23c) with lower enriched compositions, whereas the northern segments of the ridge have higher ε_{Nd} ratios (5-15) for varying $\Delta\varepsilon Hf$.

$\Delta 8/4$ and $\Delta\varepsilon Hf$ hint at a linear correlation trend, particularly the samples from 40 to 55°S, which is differing from the more northern parts of the Atlantic by having higher $\Delta 8/4$ (10-110) for comparable $\Delta\varepsilon Hf$ values (Figure 19d). The MAR north of 15°S has a completely different isotopic signature than in the southern Atlantic 40 to 55°S. One exception is the high $\Delta 8/4$ value at 6°S near Ascension.

3.2.3.   Ridges of the Indian Ocean

Central Indian Ridge, Gulf of Aden and Red Sea Rift

Figure 20 shows the along-axis ridge depth, crustal thickness, gravity anomaly and geochemical variations for the CIR and its continuation into the Red Sea. The CIR stretches northwards from the Rodrigues Triple Junction (26°S) to the Owen Fracture Zone at 10°N with its northernmost NW-SE oriented part (north of 2°N) being the Carlsberg Ridge. In the Gulf of Aden west of the Owen Fracture Zone, the ridge is oriented in an east-west direction until it meets the Afar hotspot and further continues towards the north-west in the Red Sea (12 to 28°N). The crustal thickness is constant at ca. 7 km for the whole CIR and increases westwards on the Carlsberg Ridge to up to 19 km at the Afar Hotspot very close to African continental crust. In the Red Sea the crustal thickness varies between 6 and 18 km, due to the sampling localities being in different parts of the rift with different amounts of continental crust and plume generated lavas being present.

The strongest geochemical signature of the region is present in the enriched signature in Sr, Nd and Pb isotopes, as well as La/Sm ratios at the Afar hotspot, which is, although weaker and with varying intensities, also present in most of the Red Sea. The Gulf of Aden W of 48°E has Indian DUPAL signature (Meyzen et al., 2007) hinting at a common plume or Tethys related origin of the crustal enrichment signature (Zhang et al., 2005). Depleted compositions occur between 21 and 23°N in the

central Red Sea where the formation of oceanic crust has started. The CIR is generally less enriched and shows a trend of increasing depletion towards the north. The most depleted signature is present on the Carlsberg Ridge at 10°N and could hint at detached depleted lithosphere. Enriched isotope signatures deviating from the general trend are present at 16 to 18°S, which is close to the Seychelles plateau, composed of flood basalts and continental fragments (Collier et al., 2008), as well as on the same latitude as the Réunion Hotspot. Therefore an incorporation of continental material in the local upper mantle is a viable option and some plume influence is possible.

$\Delta 8/4$ has only positive values and follows the enrichment pattern with the main maximum values being present close to the Rodrigues Triple Junction and at the Afar hotspot. This hints at the presence of a component with elevated $\Delta 8/4$ as the main source of enrichment in the northern Indian Ocean (for further discussion see section 4). $\Delta 8/4$ and $\Delta 7/4$ are correlated with major variation in the $\Delta 8/4$ to $\Delta 7/4$ ratio being present only in the Red Sea, where the ongoing rifting and plume activity suggests a complex mixture of components contributing to melt generation. The Northern Red Sea is relatively depleted in ^{208}Pb, Sr and Nd isotopes and has mostly low $\Delta 8/4$ and ^{208}Pb, but high $\Delta 7/4$ and ^{207}Pb.
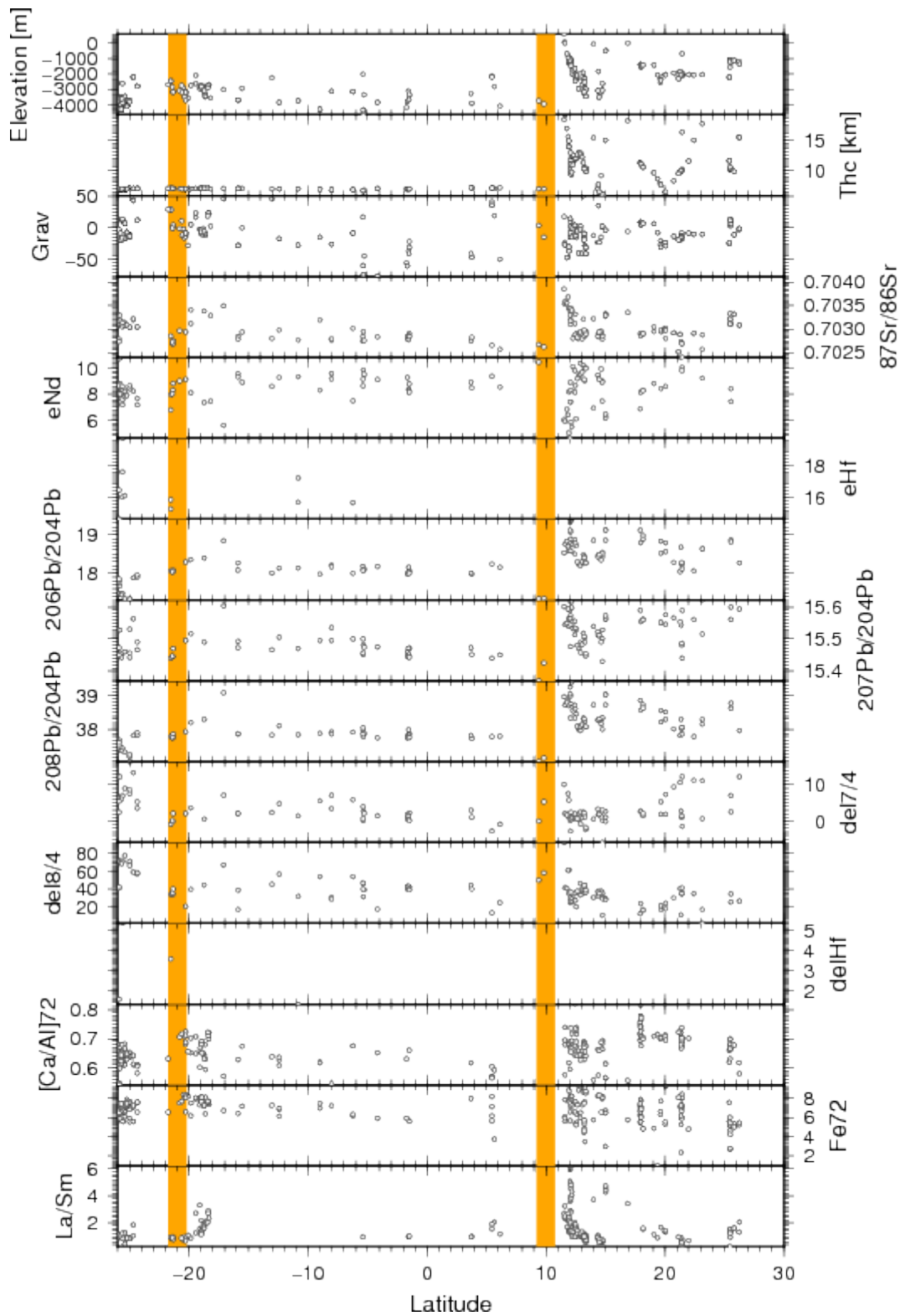
Figure 20: Along axis variation for the Central Indian Ridge, the Gulf of Aden and the Red Sea Rift. Marked hotspots (left to right) are Réunion and Afar. Further explanations in Fig. 14.
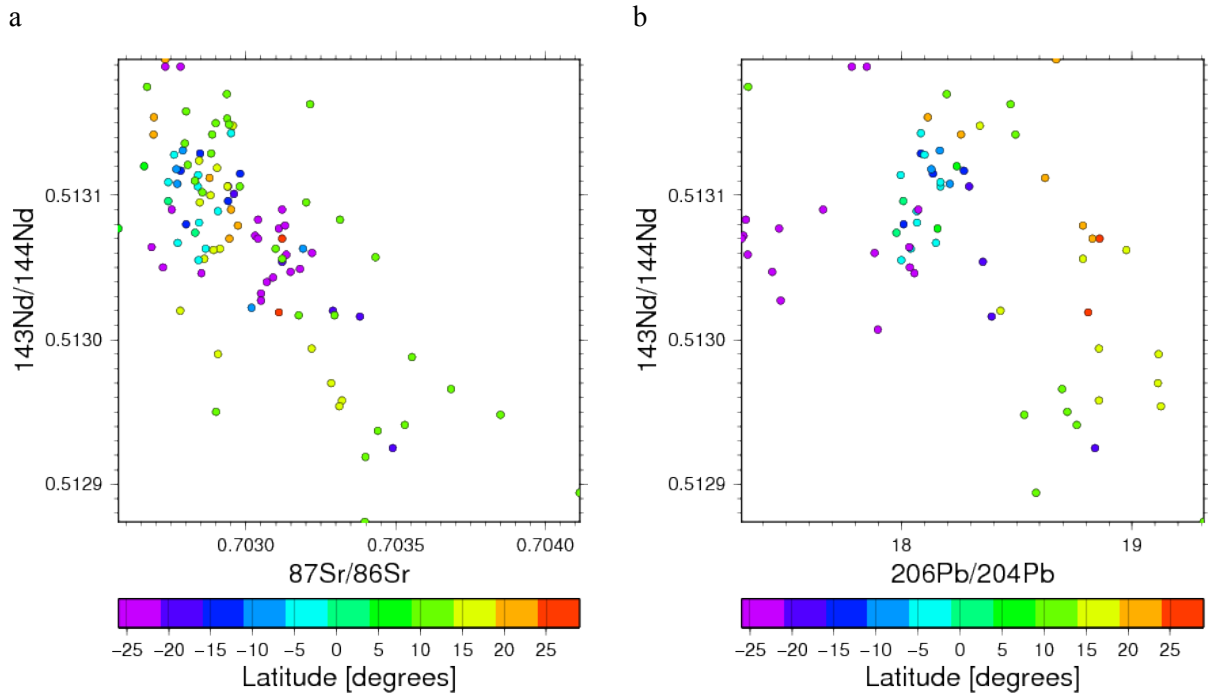
Figure 21: (a) $^{143}Nd/^{144}Nd$-$^{87}Sr/^{86}Sr$ and (b) $^{143}Nd/^{144}Nd$-$^{206}Pb/^{204}Pb$ plots for MORB of the Central Indian Ridge, the Gulf of Aden and the Red Sea Rift.

The Sr and Nd isotope ratios (Figure 21a) show a general anticorrelation with different areas covering distinct arrays. The widest range including the lowest $^{143}Nd/^{144}Nd$ and highest $^{87}Sr/^{86}Sr$ of the region is present near the Afar hotspot (10-20°N) and at 16°S while the other areas share relatively high $^{143}Nd/^{144}Nd$ and low $^{87}Sr/^{86}Sr$ ratios.

The $^{143}Nd/^{144}Nd$-$^{206}Pb/^{204}Pb$ isotope diagram has a similar tendency visible as the $^{143}Nd/^{144}Nd$-$^{87}Sr/^{86}Sr$ plot with a generally anticorrelated trend (Figure 21b). While there is no very clear segmentation within most of the region, the southernmost ridge segments of the CIR (20-25°S) deviate from the general regional trend by showing lower $^{206}Pb/^{204}Pb$ for given $^{143}Nd/^{144}Nd$ which is more characteristic for the southern parts of the Indian Ocean.

South-West Indian Ridge

Figure 22 shows the along-axis ridge depth, crustal thickness, gravity anomaly and geochemical variations for the SWIR, which is separated by the Dutoit Fracture Zone (ca. 30°E) in a western (0-30°E) and an eastern (30-70°E) segment. The crustal thickness varies within the narrow array of 6.7 to 7.1 km and its variation pattern does not reflect the changes in ridge depth and gravity anomaly well.

A major geochemical boundary is present in the central part of the SWIR (30-40°E) with more enriched Pb and Nd isotopic compositions being present in the western part that geochemically is part of the South Atlantic domain. More enriched Sr-Nd-Pb-isotope and La/Sm ratios are mostly in the vicinities of hotspots, such as the Meteor, Bouvet, Marion, Crozet and potentially Réunion Hotspots.

49

Additionally, enrichment occurs at 12-15°E (especially 15°E), most visibly in REE ratios. As in the Arctic ridges a partial decoupling of the La/Sm ratio from the Sr-Nd-Pb-isotope ratios can be observed for the western SWIR.

$\Delta 8/4$ and $\Delta 7/4$ have only positive values and generally follow the enrichment pattern. Still $\Delta 8/4$ shows a trend of increase to the east, whereas $\Delta 7/4$ does not. High $\Delta 7/4$ occurs near the Bouvet and Meteor Hotspots, at 39-41°E and at 66°E. The enrichment at 39-41°E in Sr, REE, accompanied by high values for the Δ indices, but depletion in the Pb isotope signal, reflects the presence of continental material that was potentially detached from Madagascar by the mantle flow (Meyzen et al., 2007) or brought in the upper mantle by the nearby plumes of the Marion and Crozet Hotspots. High $\Delta\varepsilon Hf$ near these hotspots indicates the presence of a depleted component such as SCLM in the plume transported material, whereas at the same time highly radiogenic Os isotope ratios (compare Figure 6) suggest LCC (as discussed by Escrig et al., 2004). Low $\Delta\varepsilon Hf$ at 25°E far away from hotspots, but near an area of thickened crust, may potentially indicate the presence of shallow detached LCC. It is reasonable to expect a presence of both components as part of plume material contaminated by detached material from continental roots (compare section 4 and 5; Meyzen et al., 2007).
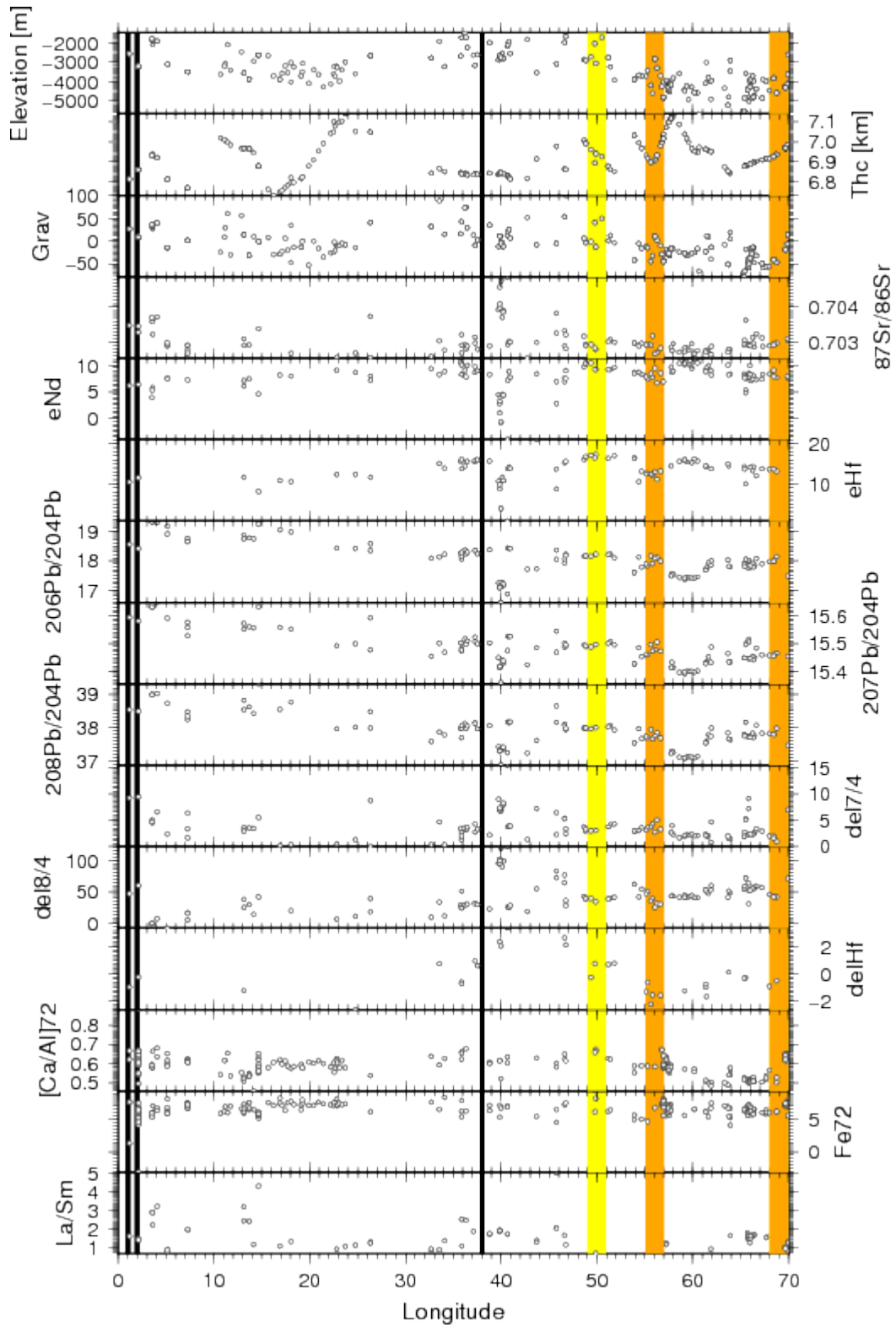
Figure 22: Along axis variation for the South West Indian Ridge. Marked hotspots (left to right) are Meteor, Bouvet, Marion, Crozet, Réunion and Kerguelen. Further explanations in Fig. 14.
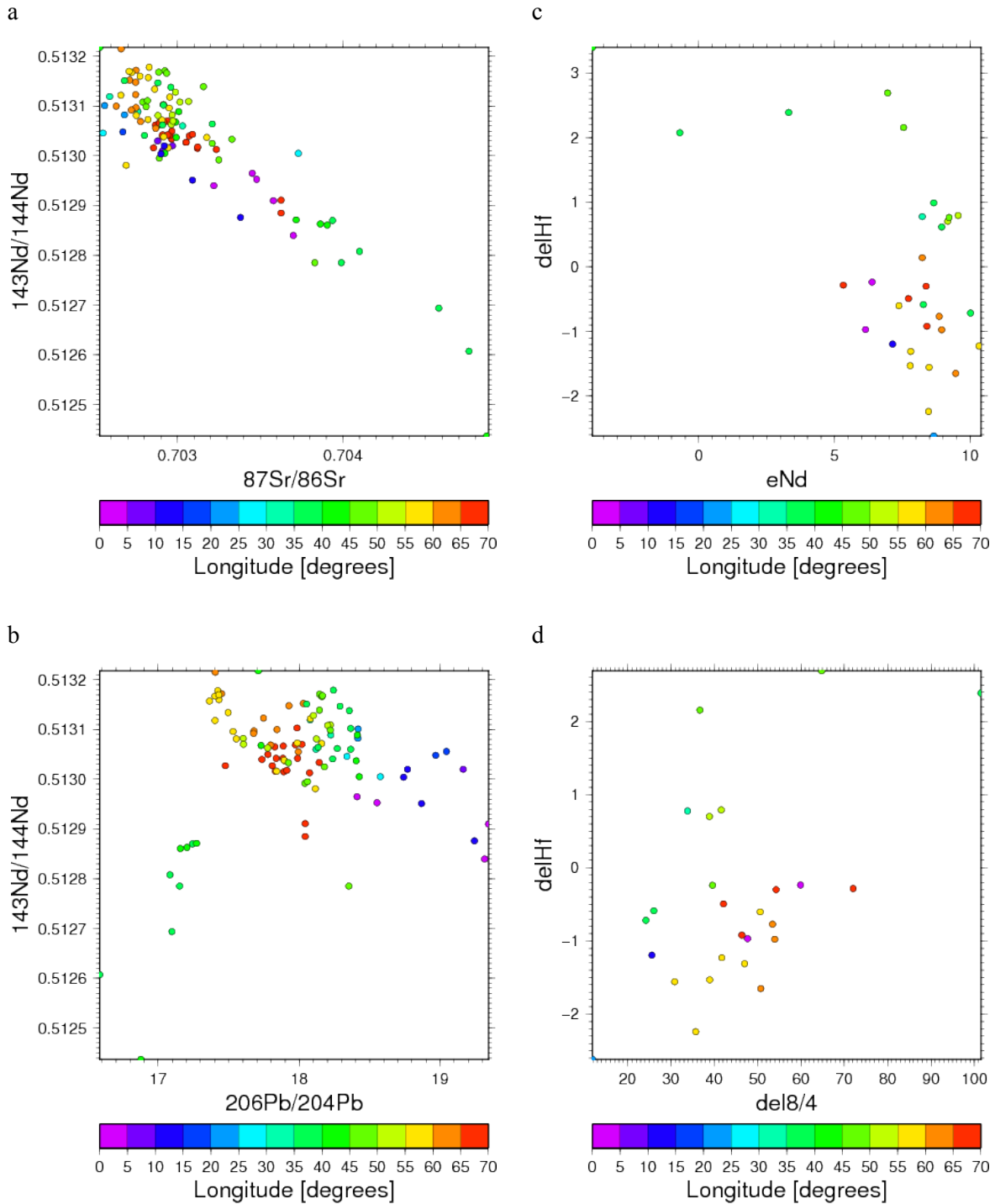
Figure 23: (a) $^{143}Nd/^{144}Nd$-$^{87}Sr/^{86}Sr$, (b) $^{143}Nd/^{144}Nd$-$^{206}Pb/^{204}Pb$, (c) $\Delta\varepsilon Hf$-ε_{Nd} and (d) $\Delta\varepsilon Hf$- $\Delta 8/4$ plots for MORB of the South-West Indian Ridge.

$^{143}Nd/^{144}Nd$ and $^{87}Sr/^{86}Sr$ show an anticorrelation (Figure 23a). While most of the SWIR clusters at $^{143}Nd/^{144}Nd$=0.51295-0.5132 and $^{87}Sr/^{86}Sr$=0.7025-0.7033, compostions with lower $^{143}Nd/^{144}Nd$ and higher 87Sr/86Sr occur near hotspots (i.e. between the Marion and the Crozet hotspot, and near the Meteor and Bouvet hotspots) as well as near the Rodrigues triple junction at the east of the SWIR and occasionally between 14 and 27°E.

52

The 143Nd/144Nd-206Pb/204Pb isotope diagram has a similar anticorrelated trend as the 143Nd/144Nd-87Sr/86Sr plot for most of the regional data (Figure 23b). From west to east there is a tendency of a decrease in 206Pb/204Pb and an increase in 143Nd/144Nd within an array confined by 143Nd/144Nd=0.51295-0.5132 and 87Sr/86Sr=17.3-19.3. Lower 206Pb/204Pb and 143Nd/144Nd ratios can be found at 39-41°E in close proximity to the Marion and the Crozet hotspots.

The ε_{Nd}-$\Delta\varepsilon$Hf signal of the SWIR shows a general trend of an anticorrelation with most samples forming a cluster at $\Delta\varepsilon$Hf=-2.5-1 and ε_{Nd}=5-11 (Figure 23c). Samples outside of this cluster with a wider span of ε_{Nd} including lower values (ε_{Nd}=-4-10) and higher positive $\Delta\varepsilon$Hf (0.5-3.4) can be found at 30-50°E near the Marion and the Crozet hotspots.

Δ8/4 and $\Delta\varepsilon$Hf hint at a positive correlation with different subparallel trends for the different parts of the ridge (Figure 23d). The central part of the ridge near the Marion and the Crozet hotspots (30-50°E) generally shows lower Δ8/4 and higher $\Delta\varepsilon$Hf than the westernmost (0-15°E) and easternmost (55-70°E) parts of the ridge.

South-East-Indian Ridge

Figure 24 shows the along-axis ridge depth, crustal thickness, gravity anomaly and geochemical variations for the SEIR. The SEIR is subdivided by its two most distinct geochemical and geophysical features: The Amsterdam/St. Paul Hotspot (78°E) and the Australian Antarctic Discordancy (AAD; 120-128°E). The shallowest ridge depth and strongest positive gravity anomaly are present at the Amsterdam hotspot, whereas the AAD represents the opposite extremes. The crustal thickness varies within the narrow array of 6.8 to 7.15 km with the only exception being crustal thicknesses of up to 7.4 km at the Amsterdam Hotspot. West of the AAD the crustal thickness roughly correlates with the geochemical and isotopic enrichment signature.

The Amsterdam Hotspot shows a local strong enrichment in the Sr, Nd and Pb isotope signal, as well as in the Sm/Nd ratio. The AAD is a major geochemical boundary between the Indian and the Pacific domain, two large scale domains of the upper mantle. This boundary however is not visible in the Sr and Nd isotopic signal or the Sr/Nd ratio, whereas it is pronounced in the Pb isotope signal (particularly ^{206}Pb/^{204}Pb and ^{208}Pb/^{204}Pb) indicating less radiogenic values at the AAD itself and a generally higher level of enrichment east of it. The Sr and Nd isotopes on the other hand show an uninterrupted trend of depletion towards the east. Similar to the Arctic ridges some decoupling of the La/Sm ratio from the Sr-Nd-Pb-isotope ratios can be observed: In most of the ridge it follows the Pb isotope pattern, east of the AAD La/Sm follows the trend of the Sr and Nd isotope signal. Similar to the Arctic this could be related to an old depletion of the lithosphere followed by re-enrichment.

The Δ indices also depict the impact of the Amsterdam Hotspot and the AAD on the SEIR. West of the AAD Δ8/4 has only high positive values with extreme values at the Amsterdam Hotspot, whereas to the east of it negative values much closer to zero are present. Δ7/4 and ΔεHf follow the same pattern in a less pronounced way with positive values dominating west of the AAD and negative values east of it. The AAD is also visible as a minimum in the fractionation corrected Ca/Al and Fe signal, indicating low amounts of melt generation. This in combination with the pronouncedness of the geochemical boundary has generally led to the interpretation of the AAD as a "convection front" in the mantle flow pattern, related to downwelling or upwelling of cold material at the presence of a "floating" subducted slab or a fragment of continental lithosphere (Klein et al., 1988; Christie et al., 1998; Hanan et al., 2004; Meyzen et al., 2007). The latter is favored by the high ΔεHf at the AAD whereas the relatively high coexisting Nd and Pb isotopic ratios suggest an influence of oceanic crust.

The geochemical Signature of the Indian Ocean MORB (DUPAL Anomaly) could be explained as well with recycled, ancient altered oceanic crust and sediments, as with ancient continental crust and/or lithosphere. Each of the models favors one of the possible mechanisms are deep recycling of subducted material (i.e. oceanic lithosphere) followed by fertilization of the upper mantle via plumes (Storey et al.,1989) and alternatively the presence of detached continental lithosphere (Arndt and Goldstein, 1989). A third possibility is the presence of crustal material as "leftover" from ancient subduction processes (Kempton et al., 2002). Newer studies based on isotope analyses such as Hanan et al. (2004) favor the presence of crustal material (most likely lower crustal material) from the rifting and breakup of Gondwana as explanation, as the plumes of the area do have too high 206Pb/204Pb ratios to be related to the low $^{206}Pb/^{204}Pb$ ratios present in the Indian MORB while SCLM has too low trace element concentrations and $^{187}Os/^{188}Os$ ratios. East of the AAD (120°E - 127°E) the isotopic signature changes to a "Pacific" signature.
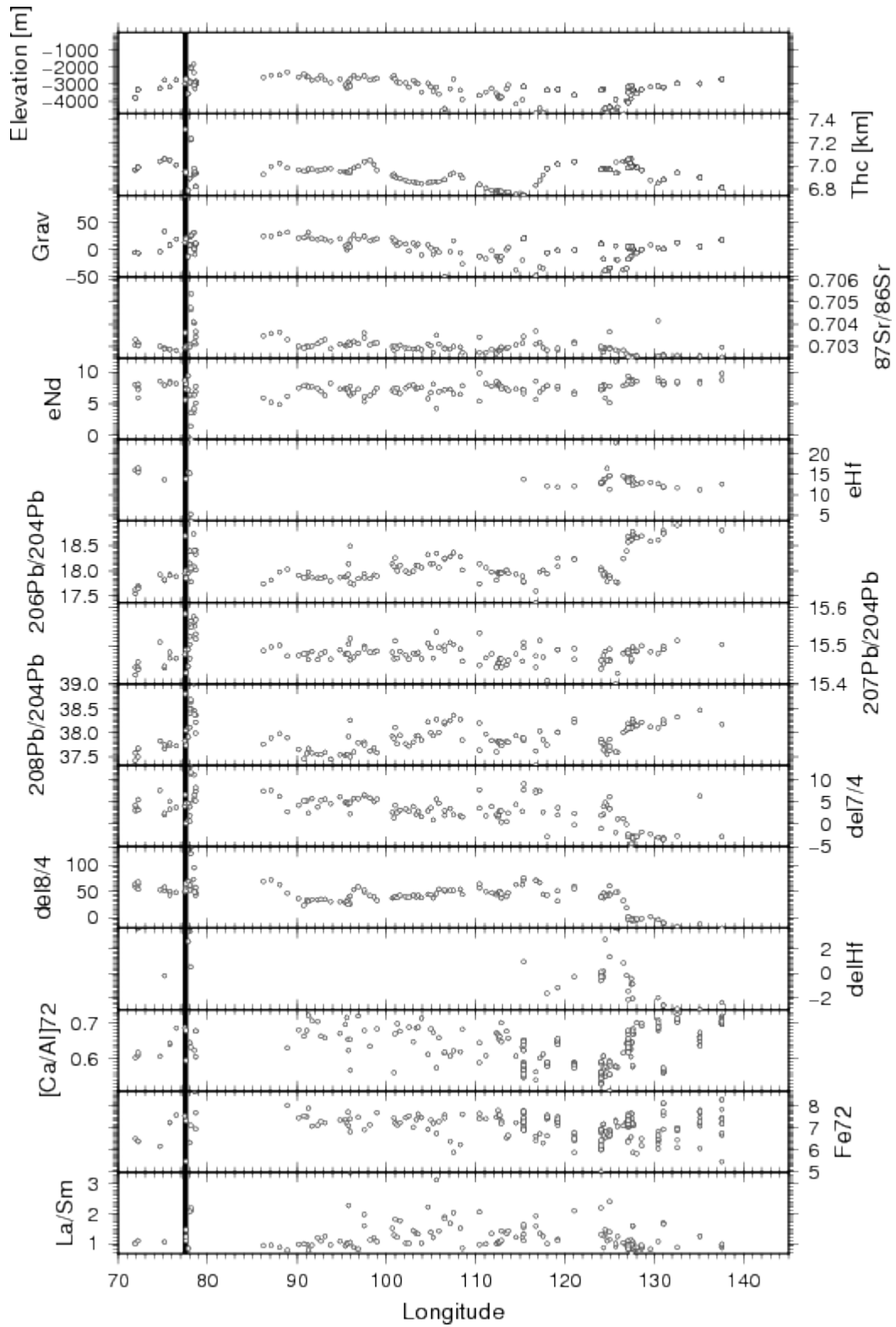
Figure 24: Along axis variation for the South East Indian Ridge. Marked hotspot is Amsterdam-St. Paul. Further explanations in Fig. 14.
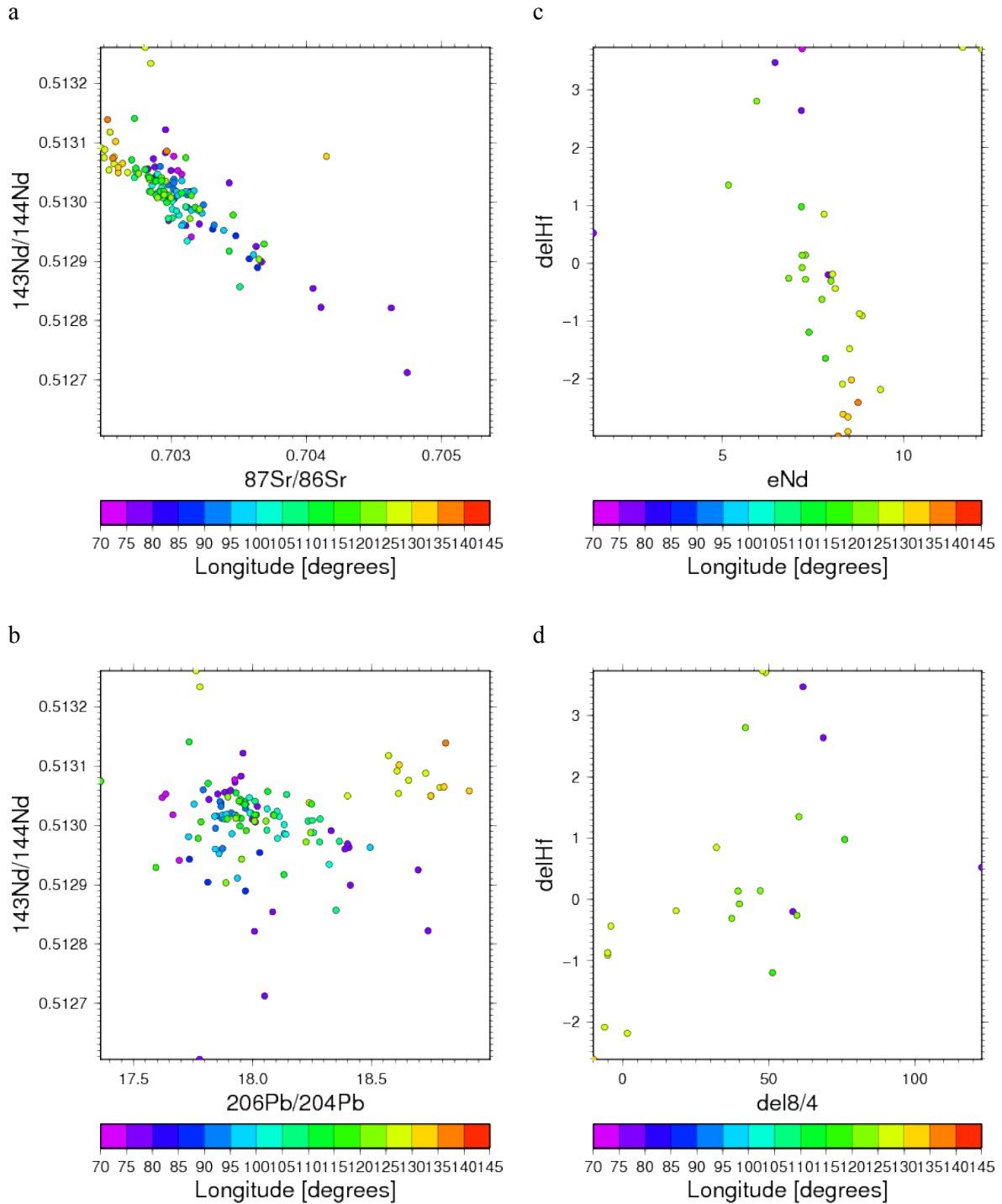
Figure 25: (a) $^{143}Nd/^{144}Nd$-$^{87}Sr/^{86}Sr$, (b) $^{143}Nd/^{144}Nd$-$^{206}Pb/^{204}Pb$, (c) $\Delta\varepsilon Hf$-ε_{Nd} and (d) $\Delta\varepsilon Hf$- $\Delta 8/4$ plots for MORB of the South-East-Indian Ridge.

The Sr and Nd isotope ratios show an anticorrelation with the main array lying between $^{143}Nd/^{144}Nd$=0.51285-0.51315 and $^{87}Sr/^{86}Sr$=0.7028-0.7038 respectively (Figure 25a). Isotope ratios extending this array to more extreme compositions occur in two distinct areas: The lowest $^{143}Nd/^{144}Nd$ (0.5127-0.5129) and highest $^{87}Sr/^{86}Sr$ (0.7037-0.7048) of the region are present at the Amsterdam-St. Paul hotspot (ca. 78°E), while the highest $^{143}Nd/^{144}Nd$ (0.51305-0.51315) and lowest $^{87}Sr/^{86}Sr$ (0.7025-

0.7028) occur east of the AAD. Few samples from the area near the Amsterdam-St. Paul hotspot show higher relative $^{143}Nd/^{144}Nd$ and $^{87}Sr/^{86}Sr$ ratios lying above the general regional array and include the maximal regional $^{143}Nd/^{144}Nd$ (0.51326).

The $^{143}Nd/^{144}Nd$-$^{206}Pb/^{204}Pb$ isotope diagram (Figure 25b) shows a clear separation between the parts of the SEIR east and west of the AAD (125°E) with the eastern segments showing systematically higher $^{143}Nd/^{144}Nd$ and $^{206}Pb/^{204}Pb$. Within these two distinct sub-regions the compositions show generally anticorrelated trends. The SEIR west of the AAD shows the largest spread including the relatively highest $^{206}Pb/^{204}Pb$ and lowest $^{143}Nd/^{144}Nd$ near the Amsterdam-St. Paul hotspot (ca. 78°E) and the segments to the west of the AAD have the most confined arrays.

For the majority of the samples from the SEIR ε_{Nd} and $\Delta\varepsilon Hf$ (Figure 25c) show an anticorrelation with a clear trend from low ε_{Nd} and high (i.e. positive) $\Delta\varepsilon Hf$ in the west to high ε_{Nd} and low (i.e. negative) $\Delta\varepsilon Hf$ in the east. Isotopic signals outside of this general trend can be found at the AAD (126°E) which show the highest ε_{Nd} of the region (ca. 14) and at the same time high $\Delta\varepsilon Hf$. A different type of anomalous signature is present at the Amsterdam-St. Paul hotspot (ca. 78°E) where at one point the lowest ε_{Nd} values of the SEIR (1.5) coexist with intermediate $\Delta\varepsilon Hf$.

The limited dataset of $\Delta 8/4$ and $\Delta\varepsilon Hf$ (Figure 25d) show a linear correlation trend for the SEIR as a whole, although the different ridge segments are distinct in their $\Delta\varepsilon Hf$ and $\Delta 8/4$ value. The area near the AAD (125-135°E) shows the largest variations in $\Delta\varepsilon Hf$ (-2.6-3.7), including both the highest and the lowest values of the region, as well as the lowest $\Delta 8/4$ (-10-50). In comparison the more western areas show systematically higher $\Delta\varepsilon Hf$ (>-1.3) and $\Delta 8/4$ (ca. 40-80; at the Amsterdam-St. Paul hotspot (ca. 78°E) up to 125.)

3.2.4. Pacific Ridges

East Pacific Rise

Figure 26 shows the along-axis ridge depth, crustal thickness, gravity anomaly and geochemical variations for the East Pacific Rise (EPR). Generally the data in the southern EPR is scarce and huge areas between 170°W/65°S and 140°W/55°S and between 117°W/53°S and 108°W/35°S are not covered by most parameters of the dataset at all. The EPR is subdivided by its triple junctions with branching ridges and the respective micro-plates formed at these triple junctions. The Juan Fernandez Triple Junction (JFTJ; 35°S) marks the branching off of the Chile Ridge and separates the southernmost EPR bordering the Antarctic Plate from the central part bordering the Nazca Plate, whereas the Galapagos Triple Junction (GTJ, 2°N) separates this central part from the northern segment bordering the Cocos, Rivera and North American Plates in the Gulf of California. The crustal

thickness is very constant at ca. 7 km for most of the EPR with thinner crust (6 km) being present between 20 and 22°N near the Socorro hotspot and thicker crust of up to 9 km thickness occurring at the northernmost end of the EPR in the Gulf of California (22-24°N). This change in crustal thickness reflects the transition towards the continental crust of North America. Some lesser variations of crustal thickness can be attributed to geochemical enrichment such as most notably the slightly thickened crust near the Louisville Hotspot (52-55°S). On the fast spreading EPR the hotspot signatures in crustal thickness and geochemical parameters (and potentially other inhomogeneities as well) are diluted compared to slower spreading ridges, making the EPR the most homogeneous of the major MORs. The EPR has the highest Ca_{72}/Al_{72} ratios (0.65-0.73) of the main MORs, reflecting a high degree of partial melting (Niu and O'Hara, 2008), and also a higher proportion of the ROC component relative to the EM-type components (Jackson and Dasgupta, 2008).

Much of the variation in the Sr, Nd and Pb isotope signal can be attributed to hotspots, such as the Louisville, Easter, Socorro and potentially also Galapagos Hotspots. Although the local variability (spread) is low, there is variability in the isotopic compositions between different parts of the EPR further away from hotspots such as relatively enriched signatures at 38°S, 16-21°S, 8°S and 8-10°N. With the exception of the enrichment at 38°S and 8-10°N La/Sm does not reflect these phenomena and therefore indicates the presence of older local mantle potentially containing some ROC. The enrichment at 8-10°N has a signature with high Sr and Pb, low Hf isotope ratios and high REE ratios potentially related to recycled crust that could possibly be supplied by the Galapagos hotspot.

Δ7/4 and Δ8/4 are close to zero (compared to other regions) for almost all the EPR indicating its "standard" asthenospheric signature.

The pattern of ΔεHf strongly resembles the pattern of the Pb isotope ratios. Showing exclusively negative values except for one point at the Easter Hotspot, ΔεHf illustrates the general absence of continental material in the Pacific asthenosphere.
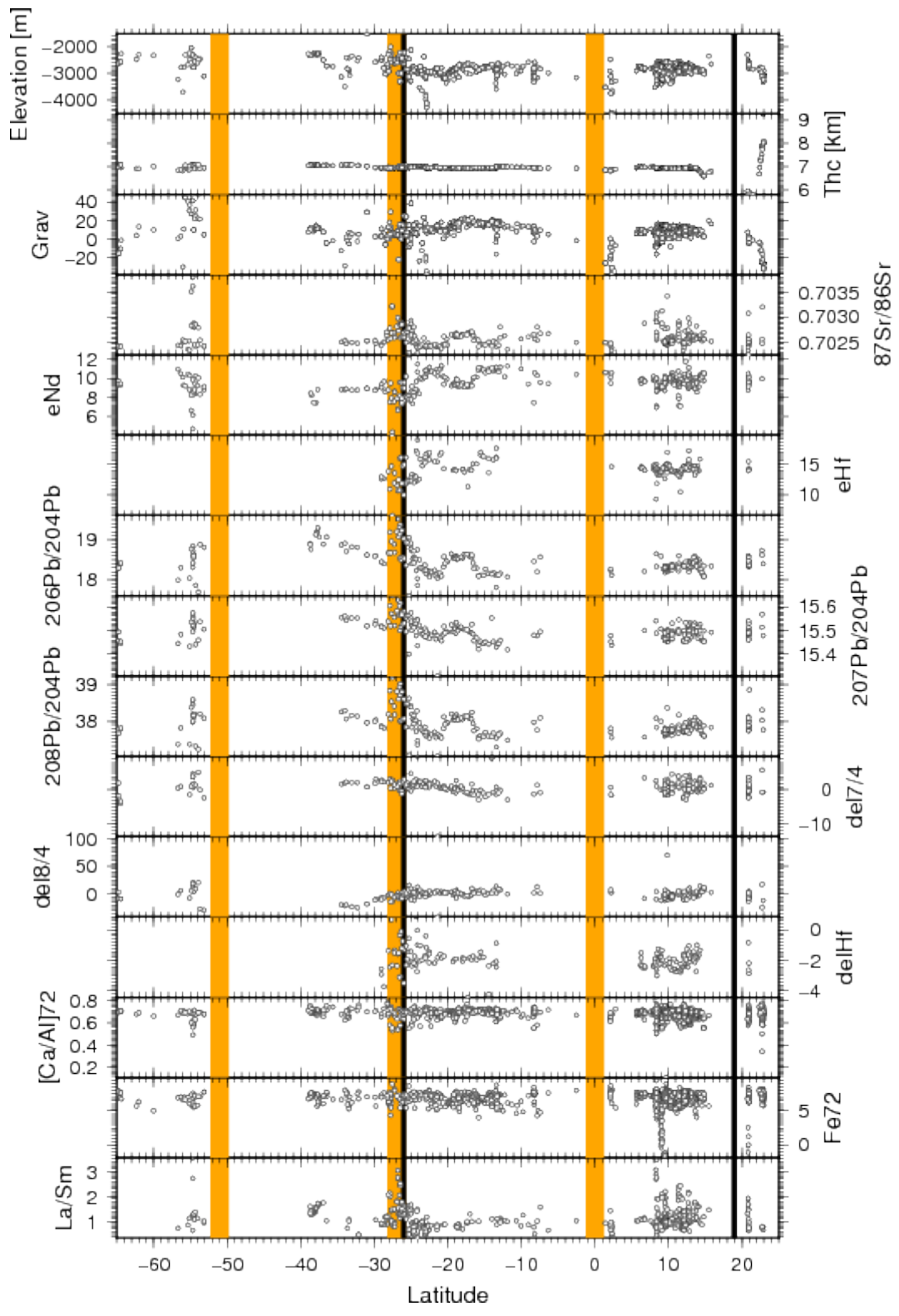
Figure 26: Along axis variation for the East Pacific Rise. Marked hotspots (left to right) are Louisville, Easter, Pitcairn, Galapagos and Socorro. Further explanations in Fig. 14.
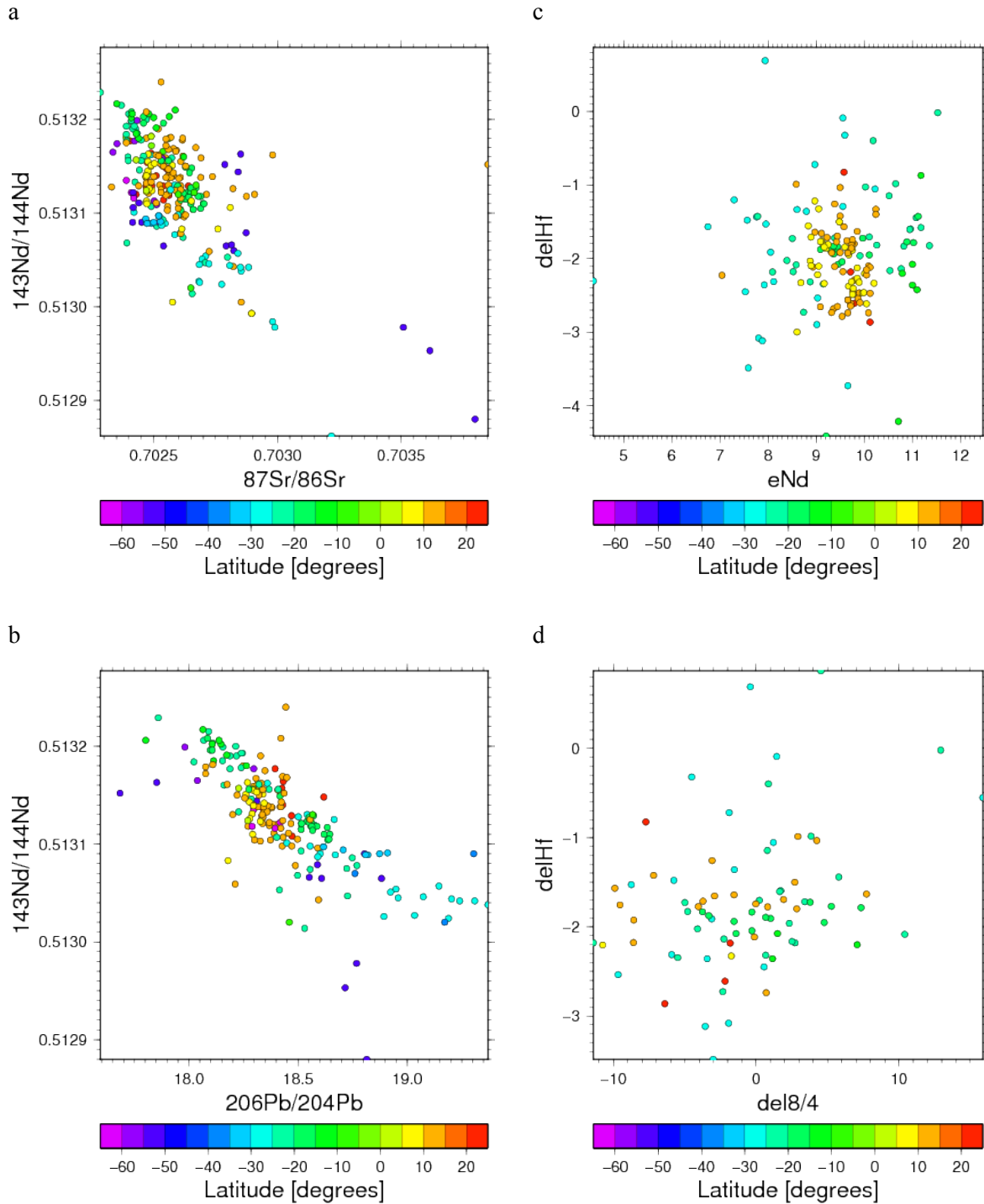
Figure 27: (a) ^{143}Nd/^{144}Nd-^{87}Sr/^{86}Sr, (b) ^{143}Nd/^{144}Nd-^{206}Pb/^{204}Pb, (c) ΔεHf-ε$_{Nd}$ and (d) ΔεHf- Δ8/4 plots for MORB of the East Pacific Rise.

The Sr and Nd isotope signal of the EPR (Figure 27a) generally follows an anticorrelation with almost all compositions being within the array of ^{143}Nd/^{144}Nd=0.51298-0.51325 and ^{87}Sr/^{86}Sr=0.7023-0.7030. Distinct trending of the isotopic signatures outside of this confined array that still follow similar subparralel trends are present near the Louisville (ca. 55°S) and the Easter (ca. 25°S) hotspots, showing the lowest ^{143}Nd/^{144}Nd (0.51300-0.51296) and highest ^{87}Sr/^{86}Sr (Louisville: 0.7035-0.7038;

60

Easter: 0.7029-0.7033) of the region. One irregular sample far off from the general trend with relatively high $^{143}Nd/^{144}Nd$ (0.51315) and extremely high $^{87}Sr/^{86}Sr$ (0.7038) is present in the northernmost EPR.

In the $^{143}Nd/^{144}Nd$-$^{206}Pb/^{204}Pb$ isotope diagram (Figure 27b) the general picture is similar to the one visible in the Sr and Nd isotopes. Most of the EPR has very homogenous isotopic characteristics ($^{206}Pb/^{204}Pb$=18.0-18.6; $^{143}Nd/^{144}Nd$=0.51298-0.51325)and the major deviations from this towards lower $^{143}Nd/^{144}Nd$ and higher $^{206}Pb/^{204}Pb$ occur at the Louisville (ca. 55°S) and the Easter (ca. 25°S) hotspots. The two hotspots show distinct signatures with Louisville having the lowest $^{143}Nd/^{144}Nd$ (ca. 0.5129) while the Easter hotspot does not deviate much from the bulk (0.5130-0.5131). In respect to $^{206}Pb/^{204}Pb$ on the other hand the Easter hotspot shows more extreme compositions (>18.9) that are not shared by the Louisville hotspot.

ε_{Nd} and $\Delta\varepsilon Hf$ data does not cover the southern parts of the EPR (including the Louisville hotspot), and the widest spread of compositions towards all extremes is present at the Easter hotspot (Figure 27c). Apart from the hotspot influenced samples the signal is relatively homogeneous with almost all points clustering at $\Delta\varepsilon Hf$=0 - -3 and ε_{Nd}=8.5-10.5 and the only other deviation being a group of samples from 10-20°S that show the regionally highest ε_{Nd} (10-12).

$\Delta 8/4$ and $\Delta\varepsilon Hf$ also do not cover the southernmost EPR and show no clear trend, but a clustering of all points in a relatively limited area ($\Delta 8/4$=-10-10; $\Delta\varepsilon Hf$=-3.5-1) with the largest spread being present near the Easter hotspot (Figure 27d).

Chile Rise

Figure 28 shows the along-axis ridge depth, crustal thickness, gravity anomaly and geochemical variations for the Chile Rise. The central Chile Rise between 83°W and 92°W is not covered by geochemical data. This gap divides the dataset for the ridge in a western part (92-98°W) and an eastern part (75-83°W) nearby the subduction zone of the Peru-Chile Trench. The crustal thickness is very constant at ca. 7 km for most of the ridge, except for the easternmost segments very close to the subduction zone (75-77°W) which show an increase to up to 15 km due to the subduction of the ridge.

The western part of the ridge is relatively depleted in Sr, Nd and Pb isotope ratios as well as La/Sm, whereas the eastern part shows a much higher variation with both depleted (like in the western part) and strongly enriched signatures being present very close to one another. La/Sm only reflects this at 78°W. The presence of an enriched component in the eastern Chile Rise can partly be attributed to recycling of material from the near subduction zone and partly to the presence of a DUPAL-like continental component (Sturm et al., 1999) which could potentially be related to the relative proximity

of the Juan Fernandez Hotspot. No Hf and Os isotope data to discriminate this further exists for this ridge.

Δ7/4 and Δ8/4 follow the same pattern as the isotope ratios and indicate the presence of a potentially recycled crustal or lithospheric component in the eastern part of the ridge with high positive values.
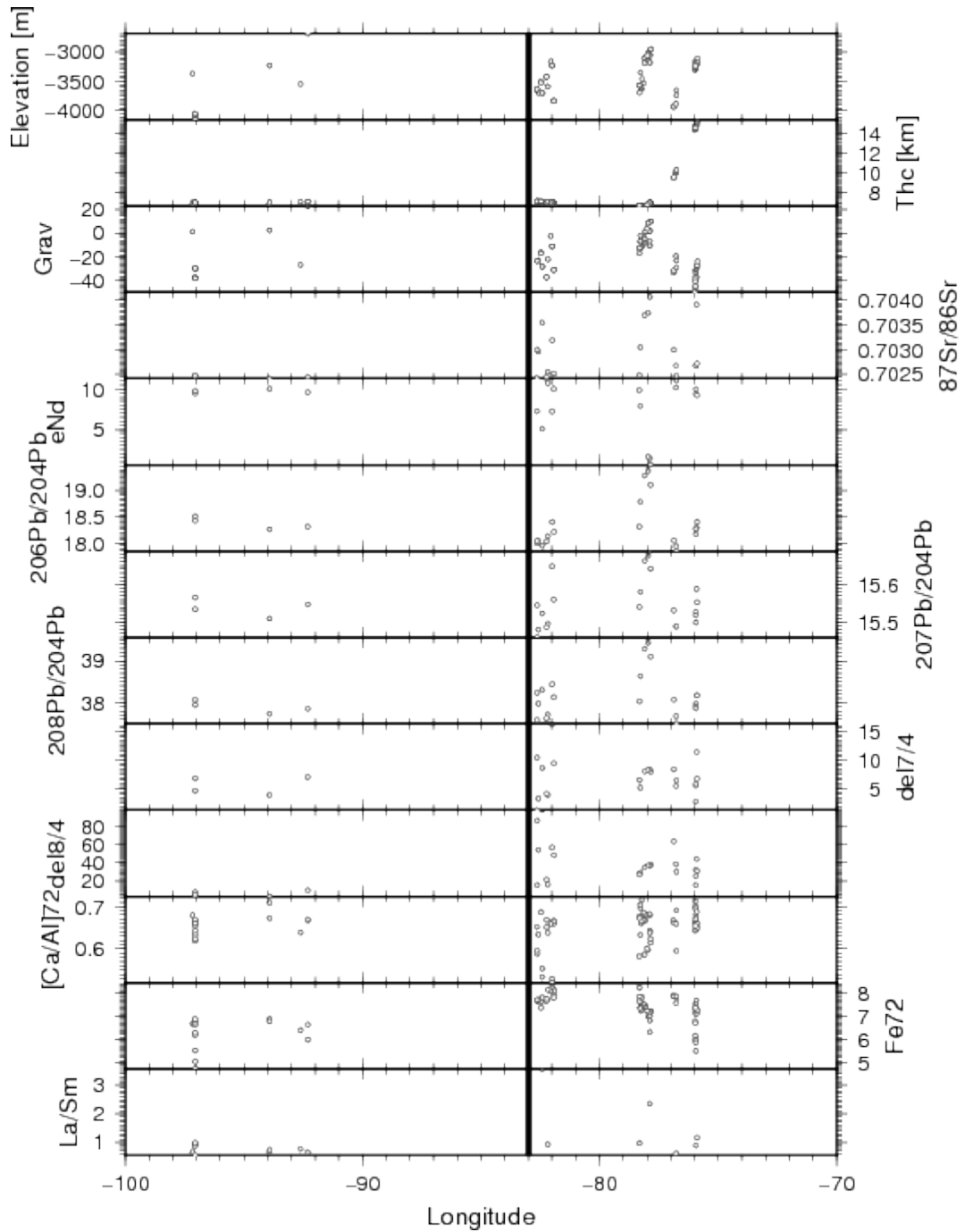
Figure 28: Along axis variation for the Chile Rise. Marked hotspot is Juan Fernandez. Further explanations in Fig. 14.
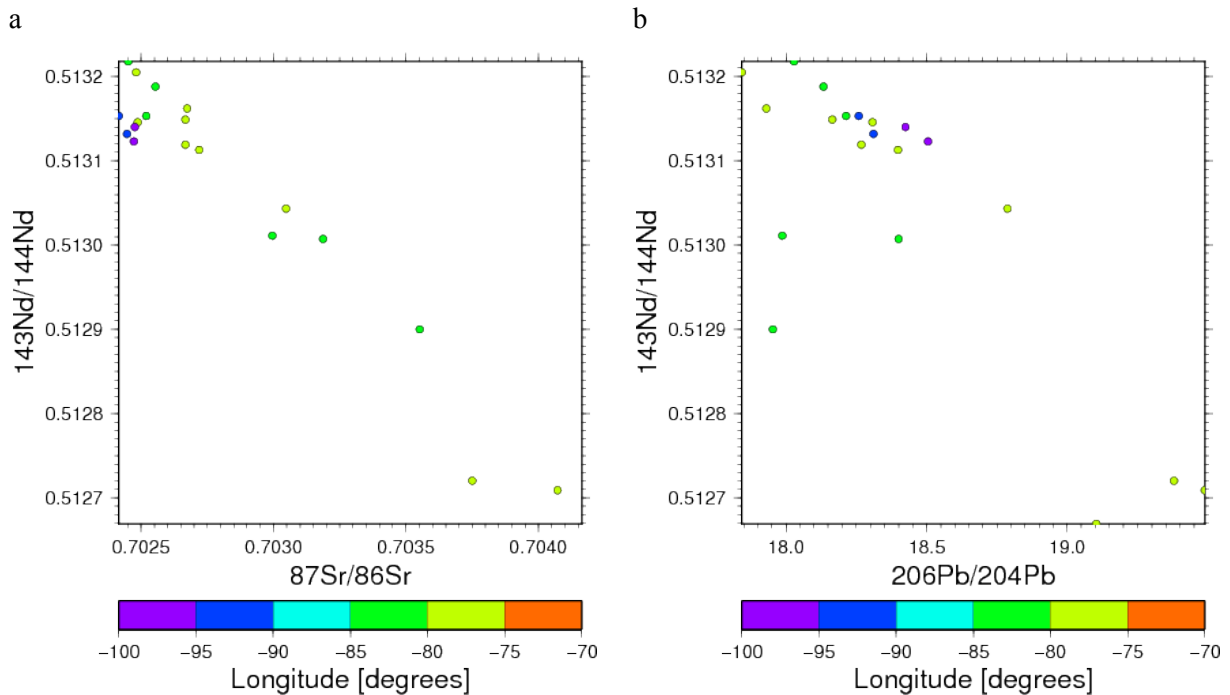
Figure 29: (a) ^{143}Nd/^{144}Nd-^{87}Sr/^{86}Sr and (b) ^{143}Nd/^{144}Nd-^{206}Pb/^{204}Pb plots for MORB of the Chile Rise.

The Sr and Nd isotope signal (Figure 29a)of the Chile Ridge forms an anticorrelation within an array confined by 143Nd/144Nd=0.5127-0.5132 and 87Sr/86Sr=0.7023-0.7042. While the enriched eastern ridge segments (75-85°W) cover much of the regional range, the westernmost part of the ridge (90-100°W) has an extremely narrow range of compositions (143Nd/144Nd=0.5131-0.5132 and 87Sr/86Sr=0.7023-0.7025) at the high 143Nd/144Nd and low 87Sr/86Sr end of the regional range.

Although 206Pb/204Pb plotted against 143Nd/144Nd (Figure 29b) shows a general anticorrelation, when viewed with the 206Pb/204Pb ratios the wide spread in 143Nd/144Nd signature at 75-85°W does show two distinct trends east and west of 80°W: To the west 206Pb/204Pb is limited to 17.9-18.5 and 206Pb/204Pb does not vary significantly in correlation to 143Nd/144Nd, while to the west the complete regional range is represented (206Pb/204Pb=17.8-19.5).

Galapagos Ridge

Figure 30 shows the along-axis ridge depth, crustal thickness, gravity anomaly and geochemical variations for the Galapagos Ridge. The Galapagos Ridge is in all aspects dominated by the nearby Galapagos Hotspot (92°W) which affects the ridge between 85 and 95°W. The main crustal thickening related to the hotspot is centered around 90°W, where it reaches 13 km, extending from 92 to 85°W and forms the transection of the Cocos Ridge, a track of the Galapagos hotspot. This crustal thickening only reflects the eastern part of the elevated ridge and positive gravity anomaly present in the area. The segment west of 92°W has a constant crustal thickness of ca. 7 km while the eastern part of the ridge varies more and reaches higher crustal thicknesses closer to the continent.

The Sr isotopic signature of the enrichment by the Galapagos hotspot is atypical and very weak, except for one point at 86°W where anomalous high Fe basalts are present. The Nd, Hf and Pb isotopes as well as La/Sm on the other hand follow the geophysical signature of the hotspot and indicate enrichment between 85 and 95°W with the maximum between 89 and 93°W. The hotspot signature of the ridge is generally stronger than on the Galapagos Islands directly on top of the plume, which can be explained with deep asthenospheric flow of plume material towards the ridge, decoupled from plate movement, and multi stage melting (Villagómez et al., 2014).

$\Delta 8/4$ and $\Delta 7/4$ follow the general enrichment pattern possibly representing the varying contribution of a relatively uniform enriched component. High $\Delta 8/4$ and low $\Delta\varepsilon Hf$ indicate the presence of ROC in the Galapagos hotspot signature. Fractionation corrected Ca/Al and Fe show extreme peaks indicating a very low melt fraction for the high Fe basalts at 86°W.

$^{143}Nd/^{144}Nd$ viewed against $^{87}Sr/^{86}Sr$ and $^{206}Pb/^{204}Pb$ plotted against $^{143}Nd/^{144}Nd$ show identical pictures for the Galapagos ridge (Figure 31a, b): The general trend forms an anticorrelation of the two respective isotope ratios and the central part of the ridge closest to the hotspot shows a much wider spread and compasses lower $^{143}Nd/^{144}Nd$ ratios than there are present in the western and eastern parts of the ridge.

In the areas close to the Galapagos hotspot lower values for both $\Delta\varepsilon Hf$ and particularly ε_{Nd} are present while the eastern part of the ridge shows relatively high ε_{Nd} and low $\Delta\varepsilon Hf$ and the western end is constrained to both high ε_{Nd} and $\Delta\varepsilon Hf$ (Figure 31c).

As the other isotopic indexes $\Delta 8/4$ and $\Delta\varepsilon Hf$ (Figure 31d) show a much wider variation of compositions in the central parts of the ridge near the hotspot ($\Delta 8/4=3-36$; $\Delta\varepsilon Hf=-2.9-1$) than it is the case in the westernmost and the easternmost parts ($\Delta 8/4=2-30$; $\Delta\varepsilon Hf=-1.6-0.5$). In these less hotspot affected parts a linear relationship between $\Delta 8/4$ and $\Delta\varepsilon Hf$ is visible, the eastern part showing lower and the western part showing higher$\Delta 8/4$ and $\Delta\varepsilon Hf$. Also in the area closer to the Galapagos hotspot higher values are more prevalent in the west.
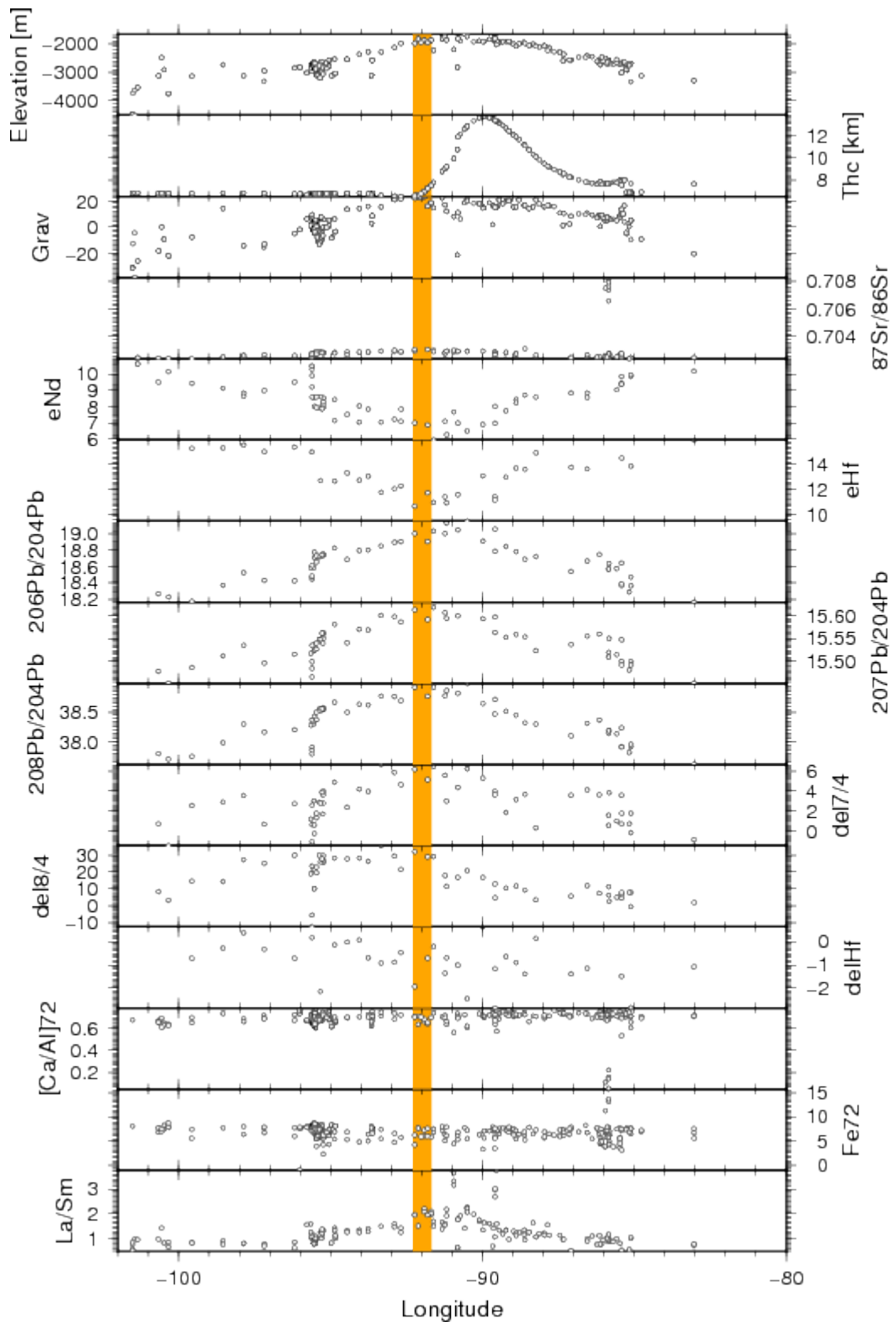
Figure 30: Along axis variation for the Galapagos Ridge. Marked hotspot is Galapagos. Further explanations in Fig. 14.

a

c

b

d
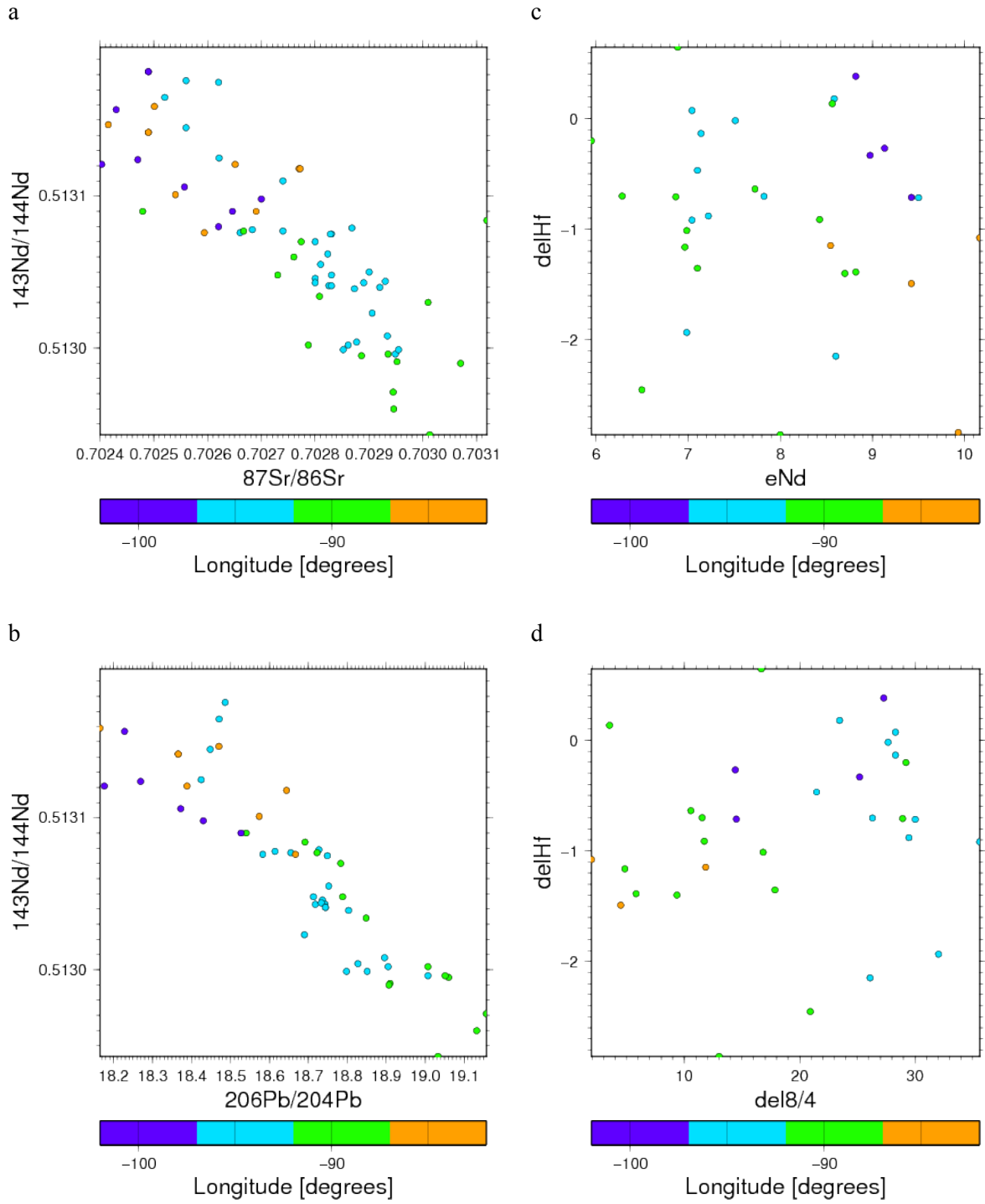
Figure 31: (a) ^{143}Nd/^{144}Nd-^{87}Sr/^{86}Sr, (b) ^{143}Nd/^{144}Nd-^{206}Pb/^{204}Pb, (c) $\Delta\varepsilon$Hf-ε_{Nd} and (d) $\Delta\varepsilon$Hf- Δ8/4 plots for MORB of the Galapagos Ridge.

66

Juan de Fuca Ridge

Figure 32 shows the along-axis ridge depth, crustal thickness, gravity anomaly and geochemical variations for the Juan de Fuca Ridge (JFR) including the adjacent Gorda and Explorer Ridges (40-52°N). This ridge system is subdivided by fracture zones. To the south of the Blanco Fracture Zone (44°N) is the Gorda Ridge, to the north of the Sovanco Fracture Zone (49°N) the Explorer Ridge and in between lies the Juan de Fuca Ridge sensu stricto. Two minor hotspots are situated near this ridge system: The Cobb hotspot (46°N) is extremely close to the central JFR and the Bowie hotspot is near the northern end of the Explorer Ridge (53°N). The crustal thickness varies from 6 to 14 km with increasing crustal thickening related to the proximity to the North American Continent.

The Sr, Nd and Pb isotope ratios of the JFR indicate a depleted composition with little variation. The variation that is present does not show a systematic pattern. Hf isotopic data is not available.

The Δ indices also do not significantly reflect the presence of the hotspots. The Δ8/4 values close to zero are suggesting no strong influence of recycled components in the regional asthenosphere. Δ7/4 has low positive and negative values suggest old depletion ages of the local source mantle.

$^{143}Nd/^{144}Nd$ and $^{87}Sr/^{86}Sr$ (Figure 33a) show an anticorrelation within an array confined by $^{143}Nd/^{144}Nd=0.51303-0.51325$ and $^{87}Sr/^{86}Sr=0.7023-0.7026$. Ratios outside of this array with higher $^{143}Nd/^{144}Nd$ (up to 0.7029) can be found in the southern part of the ridge south of the Cobb hotspot (40-45°N).

$^{206}Pb/^{204}Pb$ plotted against $^{143}Nd/^{144}Nd$ (Figure 33b) shows a general anticorrelation with no clear subdivisions of the ridge signal within the narrow array confined by $^{206}Pb/^{204}Pb=18.1-18.9$ and $^{143}Nd/^{144}Nd=0.51303-0.51325$).
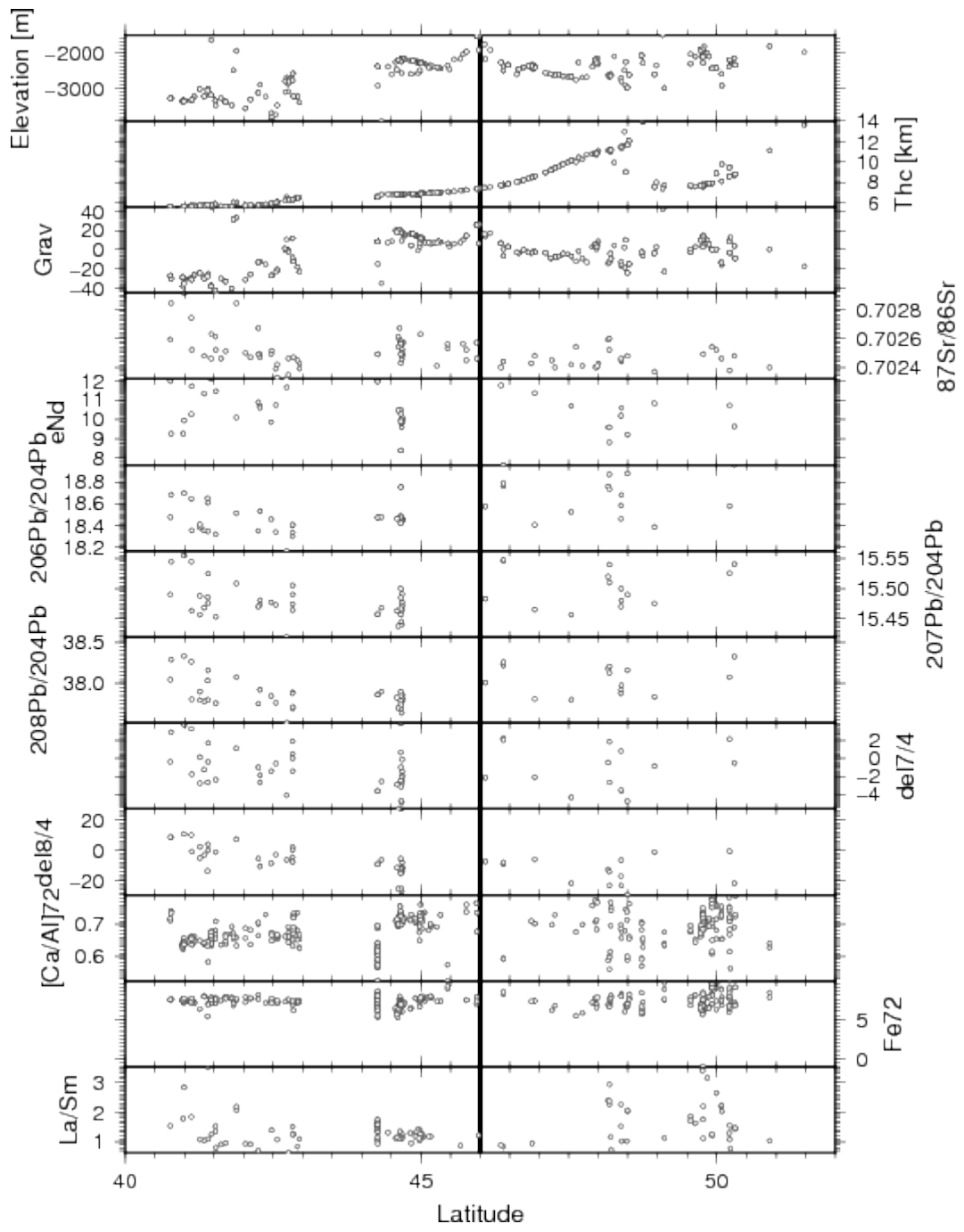
Figure 32: Along axis variation for the Juan de Fuca ridge system. Marked hotspot is Cobb. Further explanations in Fig. 14.
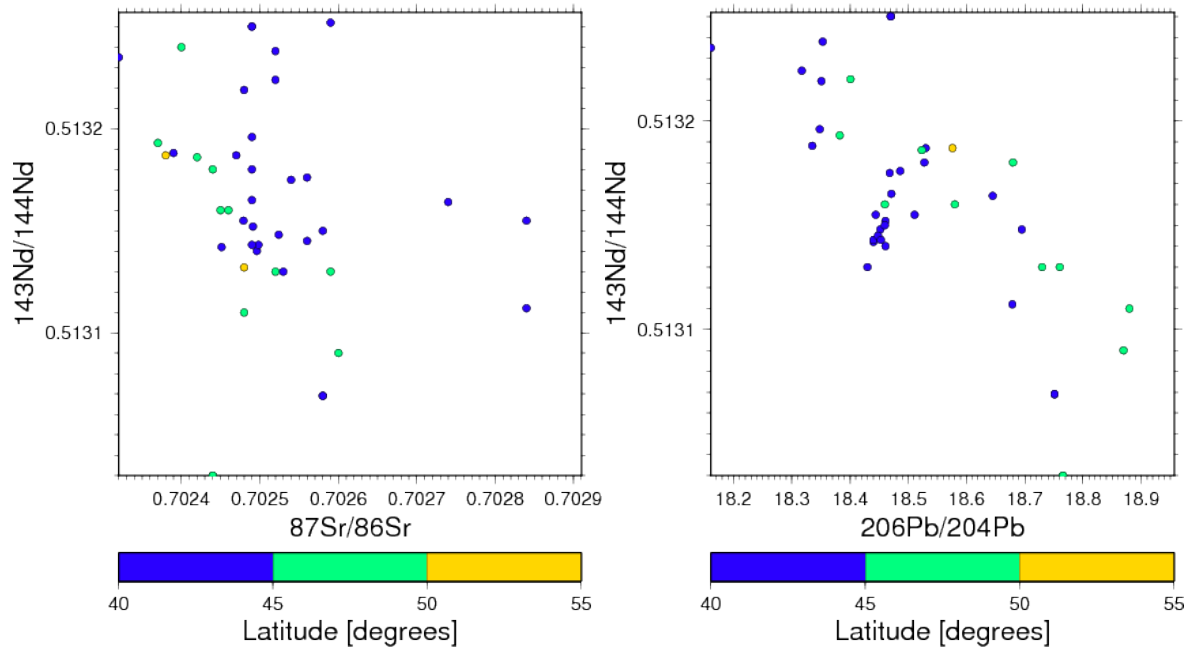
Figure 33: (a) ^{143}Nd/^{144}Nd-^{87}Sr/^{86}Sr and (b) ^{143}Nd/^{144}Nd-^{206}Pb/^{204}Pb plots for MORB of the Juan de Fuca Ridge.

3.2.5. Cayman Rise

The Cayman Rise, as deepest mid-ocean ridge endmember, was included in the analysis. However, the segment is very short for substantial along ridge variations. On global plots of the isotopic and geochemical data it always lies within or in extension of the Pacific-like depleted main array.

4. Global geochemical features

4.1. Geochemical features and their relation to geophysics

4.1.1. The effect of spreading rate, mantle potential temperature and composition

The full spreading rate for the major MOR segments vary from < 20 mm/a for the SWIR and the MAR north if Iceland via 20-35, 23-43, 60-73 and 80-150 for the MAR, CIR, SEIR and EPR, respectively. The Ca_{72}/Al_{72} ratio, corresponding to the CaO/Al_2O_3 ratio in primary mantle melts, can be used as rough measure of degree of partial melting (Niu and O'Hara, 2008 and section 3.2). As shown in Figure 22, 20, 18, 24, and 26, respectively, the Ca_{72}/Al_{72} ratios for SWIR, MAR (south of Iceland), CIR, SEIR (70°-115°E) and EPR are mostly within the following ranges: 0.50-0.67, 0.60-0.70, 0.60-0.73, 0.61-0.71, 0.65-0.73.The slightly increasing ratios support the conclusions of Niu and Hekinian (1997) that the spreading rate is positively correlated with degree of partial melting. The high Ca_{72}/Al_{72} ratios of the EPR basalts can possibly also be ascribed to a high proportion of the HIMU-component relative to the EM-components in the Pacific (Jackson and Dasgupta, 2008). The Indian Ridges which have low HIMU-proportions and low spreading rates are also characterized by low Ca_{72}/Al_{72} ratios. As a side effect high spreading rates such as at the EPR can enhance the mixing between plume material and the ambient upper mantle, dispersing the chemical and thermal plume signature (Dalton et al., 2014).

Dalton et al. (2014) demonstrated a strong negative correlation between shear-wave velocity at about 75 km depth and spreading rate (the correlation coefficient, r, is approximately -0.8). This correlation decreases with increasing depth and r reaches approximately -0.2 at depths exceeding 250 km. As pointed out by Dalton et al. (2014), the strong negative correlation between V_S and spreading rate at shallow depths simply reflect the fact that there is a wider zone of hot oceanic lithosphere on both sides of the fast-spreading ridges than on the sides of slow-spreading ridges.

The geochemical variations of MORB are widely seen as reflecting mantle variability by being the result of partial melting of a heterogeneous "marble-cake" upper mantle (Allègre et al., 1984; Morgan and Morgan, 1999; Hofmann, 2003; Stracke et al., 2005). Niu and O'Hara (2008) take this position to the extreme and completely doubt the importance of variation in T_p as from their fractionation correction calculations find only a span of Fe compositions in primary melts that suggests a variation of T_p by less than 50°C. They interpret the correlation of ridge depth and main element MORB composition as the consequence of mantle compositional variation that is responsible for isostatic ridge depth variation via differences in lithology and density. They see the correlated variation of

primary MORB melt compositions and ridge depth as the effect of dense more enriched fertile peridotite with higher garnet and jadeite content being responsible for greater ridge depths and consequentially for shorter melting columns, inhibited upwelling and reduced melt production.

The results of the different fractionation correction methods, i.e. Na72 (Niu and O'Hara, 2008) as opposed to Na8 (Klein and Langmuir, 1987) as well as Na8.5 (Kelley et al., 2006) are correlated for most data points and thus should show widely identical results (Appendix 3; compare Dalton et al., 2014). Na8 systematically shows slightly higher values than the other corrected Na compositions as it does not account for the complete fractionation from a primary melt. Although the three compared methods perform fractionation correction to different points and the correction to MgO of 8 wt% is clearly not reaching a primary melt composition they all are more or less exchangeable. Fe8 and Fe72 show a less clear correlation with a "fanning out" that could represent the differences in Fe for a given Mg# allowed with Fe72.

Dalton et al. (2014) detect the necessity of compositional variation mainly for hotspot influenced MORB such as at the Azores and the Marion hotspot where the ridge depth variation is not related to a matching variation in seismic velocity at depth. Also for other hotspots they find the existence of differing subparallel trends of correlated variation in ridge depth and seismic velocity to indicate an influence of asthenospheric compositional variation. Also the variations found in abyssal peridotites are not consistent with T_p being the only major influence on MORB composition as they directly prove heterogeneity of the upper mantle below MORs (Warren and Shimizu, 2010). On the other hand the upper mantle is also being influenced by the ascending melts that percolate through it and potentially partly crystallize in it. A consequence of this can be the local refertilization of the generally depleted upper mantle (Warren and Shimizu, 2010; Mallick et al., 2014).

4.1.2. The role of mantle temperature variation as opposed to chemical heterogeneity

Mantle potential temperature variations are a major factor controlling MORB chemistry and it has been argued by several authors (e.g. Klein and Langmuir, 1987; Dalton et al., 2014) to have a stronger influence on MORB composition than chemical mantle heterogeneity. The recent comparative study of ridge depth, seismic shear velocities at 300 km depth and fractionation-corrected major and minor element composition (Na_{90}, Ca_{90}/Al_{90} and Fe_{90}) by Dalton et al. (2014) supports a general temperature control on MORB chemistry. In that study a range of mantle potential temperatures of 250°C corresponding to the MORB compositional variation was calculated by a combination of procedures in Langmuir et al. (1993) and the pMELTS software. The derived variation pattern of the potential temperature (T_p) along ridges (Figure 34) is in accordance with much of the observed geochemical data. Variations in T_p and the resulting degree of partial melting govern the proportion of fertile and

refractory source components extracted to the melt. The type and composition of each of the fertile and refractory components, however, vary between regions.
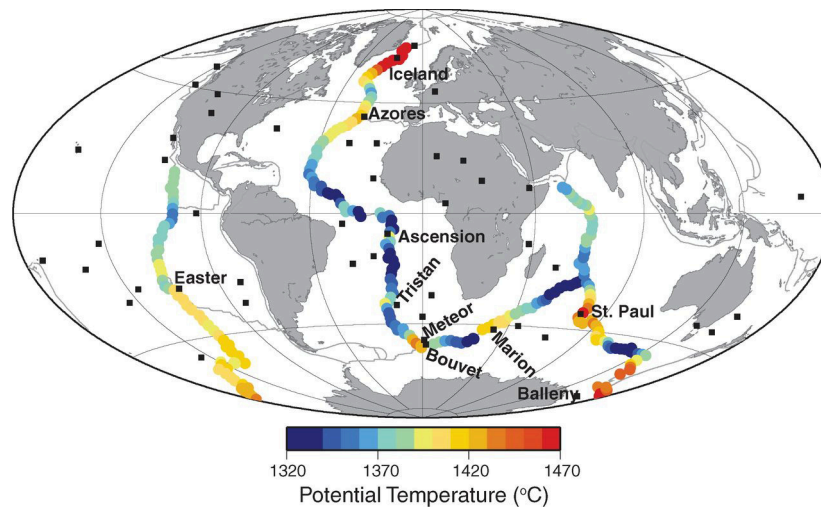
Figure 34: Mantle potential temperatures estimated from ridge depth and V_s at 300 km (from Dalton et al., 2014).

The fertile material may include subduction-modified ROC (HIMU-type components, possibly integrated with pelagic sediments as an EM2-like (i.e. UCC-like) component (e.g. Jackson et al. 2007), as well as LCC and SCLM detached from continents (EM1-like components). The process of reintroduction of such enriched components in the sub-ridge asthenosphere will complicate and differentiate the elemental compositions and the time-scales of these processes will govern the growth of the radiogenic isotopes. After the modification of ROC at the seafloor (e.g. carbonate precipitation in fractures) and in the subduction zone, the material might have a long residence time in the transition zone and lower mantle before plume or non-plume convective return to the upper mantle and asthenosphere. Low-degree partial melting of carbonated basaltic material (e.g eclogite or garnetite) to generate carbonatite melts (e.g. Rohrbach and Schmidt, 2011; Cottrell and Kelly, 2013) can lead to metasomatism of the ambient mantle (including the asthenosphere) during slab decent as well as later convective ascent. Chemically modified ROC-components extracted from such metasomatized asthenoshpere during MORB-generation will differ significantly from ROC-components that are only mechanically (convectively) mixed into the asthenosphere.

The recycling timescale and composition of detached LCC and SCLM can also be extremely variable. Such detached material can be directly incorporated into the ambient asthenosphere by convective mixing during the initial rifting and opening of an oceanic basin. Alternatively, the material can sink to the transition zone and lower mantle and be returned to the asthenosphere by deep plumes or other convective flow. The refractory component in MORB is mostly residing in the stationary melt-

depleted, and partly re-fertilized, asthenosphere. Plume-transported refractory lower mantle, however, may also mix into the asthenosphere in certain regions.

4.2. Global MORB systematics

In addition to the compositional variation within the individual ocean basins and along the major ridge segments (Section 3.2), there are also broad compositional distinctions between ocean-wide asthenospheric domains. The Nd-Sr-isotopic variation fields for MORB from the major ocean basins largely overlap with each other (Figure 35a). However, within this broadly bimodal mantle array from refractory (depleted MORB mantle, DMM) to fertile compositions, certain characteristic differences are apparent. The Pacific MORB has the most restricted compositions with an average that has higher $^{143}Nd/^{144}Nd$ and lower $^{87}Sr/^{86}Sr$ than the Indian Ocean and Atlantic-Arctic MORB. This agrees with the higher Ca_{72}/Al_{72} ratios, and thus the higher degrees of partial melting, affecting the Pacific MORB (Section 3). In addition, Jackson and Dasgupta (2008) found that the Ca/Al-ratio also tends to be slightly higher in the HIMU- or ROC-components, which seems to be the dominant fertile material in the Pacific asthenosphere, compared to the EM-type components (SCLM and LCC), which are more prevalent in Atlantic-Arctic and Indian Ocean MORB (see below). At a given $^{143}Nd/^{144}Nd$ ratio of e.g. 0.51312 the Pacific MORB has slightly lower average $^{87}Sr/^{86}Sr$ ratio than the average ratio of the other ocean basins. The ranges from strongly depleted to fertile compositions in terms of the Sr-Nd-isotopic arrays are wider for the Atlantic-Arctic ridges (slightly more refractory average) than for the Indian Ocean ridges (slightly more enriched average).

The $^{143}Nd/^{144}Nd$ versus $^{206}Pb/^{204}Pb$ diagram (Figure 35b) is potentially very useful for a discrimination between the enriched components, HIMU-ROC-type or EM1-type (LCC or SCLM). Diagrams with the $^{143}Nd/^{144}Nd$ ratio versus either $^{207}Pb/^{204}Pb$ or $^{208}Pb/^{204}Pb$ will generally show the same features. The dominant trend in these diagrams is the negatively sloping vector from DMM versus HIMU-ROC-type compositions with highly radiogenic Pb-isotope ratios. The other trends towards low $^{143}Nd/^{144}Nd$ and low $^{206}Pb/^{204}Pb$ are representative for the EM-type component mixing. As demonstrated by Figure 35b and discussed in Section 4.2, the EM1-type components have the strongest representation in the Indian Ocean and South Atlantic, i.e. the DUPAL-domain first described by Dupré and Allègre (1983) and named by Hart (1984). The NE Atlantic and Arctic ridges north of Iceland, and possibly a limited area south of the Azores, at 36 N near the east Azores (Oceanographer fracture zone), also show the EM-component trends.

The discrimination between the continental EM-type components, SCLM and LCC is not straightforward, but can in most cases be based on Os-isotope and Nb/U-concentration variation, e.g. as a function of Sr-isotope ratios (e.g. Widom and Shirey, 1996; Rehkämper and Hofmann, 1997;

Escrig et al., 2004; Sun et al., 2008; Debaille et al., 2009). Whereas convective erosion of pure SCLM material is possible, a corresponding erosion of LCC without some of the underlying SCLM seems unlikely. The prevalent enriched EM-type component along the ultra-slow spreading ridges in the NE Atlantic and Arctic (Mohns, Knipovich and western Gakkel Ridges) appears to be SCLM that was convectively eroded from the continental margins and mixed into the asthenosphere during the recent rifting and oceanic opening (Goldstein et al., 2008; Salters et al., 2011). The short time since continental rifting and short distances to the nearest continental shelf for these three ridge segments (and also for the ultra-depleted Kolbeinsey and eastern Gakkel Ridges) favor such a local convective contamination from the nearby continental margins. The postulated SCLM-contribution to the Azores magma systems, suggested by Widom and Shirey (1996), however, is much more uncertain (Schaefer et al., 2002; Cooper et al., 2004). The MORB signature near the Azores covers a wide range of compositions combining the presence of enrichment in extension of the main array (towards high μ) with both a low μ signature similar to the Southern Atlantic, and SCLM or LCC like high ΔεHf (compare Appendix 2, Figure A 10).

Most workers have favored a LCC-component convectively eroded and mixed into the Indian Ocean asthenosphere during the Mesozoic rifting and dispersal of the Pangaea continental blocks, based e.g. on Os-isotopic evidence (Escrig et al., 2004). The situation for the South Atlantic DUPAL asthenosphere is less clear, with a possible combination of SCLM and LCC, originating either by shallow asthenospheric flow (Class and Le Roex, 2009) or more likely deep plume supply (Class and Le Roex, 2011). The favored interpretation that the south Atlantic DUPAL components were supplied by the Tristan-Gough, Discovery and possibly the Shona, plumes is based on the geochemical similarity of these plumes with the DUPAL-type MORB in this area and the lack of similarity with the nearby southern African SCLM.

In the ε_{Nd}-$\Delta\varepsilon$Hf space the trend of the S-Atlantic leads more towards crustal material (low in both) and the N-Atlantic and Arctic towards a depleted reservoir such as SCLM (high in both) relative to the Pacific. In the Indian Ocean both signatures are present (Figure 35c, compare Appendix 2, Figure A 10)

The Δ8/4-Δ7/4 diagram (Figure 35d) discriminates well between the Pacific (lowest Δ8/4, low Δ7/4), Indian (high Δ8/4, high Δ7/4), South Atlantic (highest Δ8/4, highest Δ7/4), NE Atlantic and Arctic (high Δ8/4, low Δ7/4), central Atlantic (intermediate-low Δ8/4, low Δ7/4).The additional ΔεHf-Δ8/4 relations, and secondarily also the ΔεHf-Δ7/4 relations,(Figure 35e, f) are central to the identification of the LCC and MORB and other oceanic basalts, in the sense that both the ΔεHf and Δ8/4 parameters are distinctly elevated in basalts containing these components (Hanan et al., 2004; Goldstein et al., 2008). Figure 35f demonstrates at least three main vectors emanate from the Pacific MORB field with

74

ΔεHf of about -2 and Δ8/4 of about 0: (1) towards elevated ΔεHf of 5-10 for the Azores area (Oceanographer FZ), (2) towards ΔεHf of 8-9 and Δ8/4 of 30-40 for the NE Atlantic and (3) towards ΔεHf of 2-5 and Δ8/4 of 100-120 for the south Atlantic and Indian Ocean. These three vector trends probably represent three different, but broad source compositions. There is no clear difference between the Indian Ocean and the south Atlantic, although some of the Indian Ocean samples are located more between trends (2) and (3).

Elevated ΔεHf and Δ8/4 (Figure 35f) reflect time-integrated low ratios of Lu/Hf and Th/U. These ratios are high in both the SCLM and LCC components relative to ROC or HIMU components. Variations in the Δ7/4 parameter, however, are governed largely by the time in Earth history when specific depletion or enrichment events occurred. Low Δ7/4 may therefore be a result of early melt depletion, e.g. by melting somewhere in the deep mantle during the Hadean. Low Δ7/4 observed in relatively enriched (peridotite or basalt) compositions (peridotite or basalt), e.g. in Iceland, could be a result of old depletion (to low U/Pb) followed by young enrichment (increase in U/Pb with low $^{235}U/^{238}U$ ratio, e.g. Thirlwall, 1997). The ΔεHf-Δ7/4 diagram (Figure 35e) the NE Atlantic and central Atlantic MORBs (including the Azores region) are mostly within the upper left quadrant with positive ΔεHf and negative Δ7/4 with a broad field extending from the Pacific MORB (average ΔεHf and Δ7/4 of -2 and 0) towards the Indian ocean and south Atlantic (average ΔεHf of about -1 and 2 and Δ7/4 of about 2 and 8, respectively).

If the south Atlantic EM1-like DUPAL components came to the asthenosphere via deep plume supply from the lower mantle (Class and Le Roex, 2011), rather than by shallow convective erosion of SCLM and LCC during the rifting of Pangaea (e.g. Hanan et al., 2004) or by plume erosion from the bottom of the African cratons, one might expect that their compositions in the compositions the ΔεHf-Δ7/4 and Δ8/4-Δ7/4 diagrams would be displaced towards the Pacific MORB field characterized by ROC-HIMU-component mixing into the otherwise refractory asthenosphere. The actually observed opposite trend is therefore surprising and difficult to explain. A pelagic sediment component, however, will have elevated ΔεHf and Δ7/4 and could easily be introduced as a recycled component in a plume influenced setting.
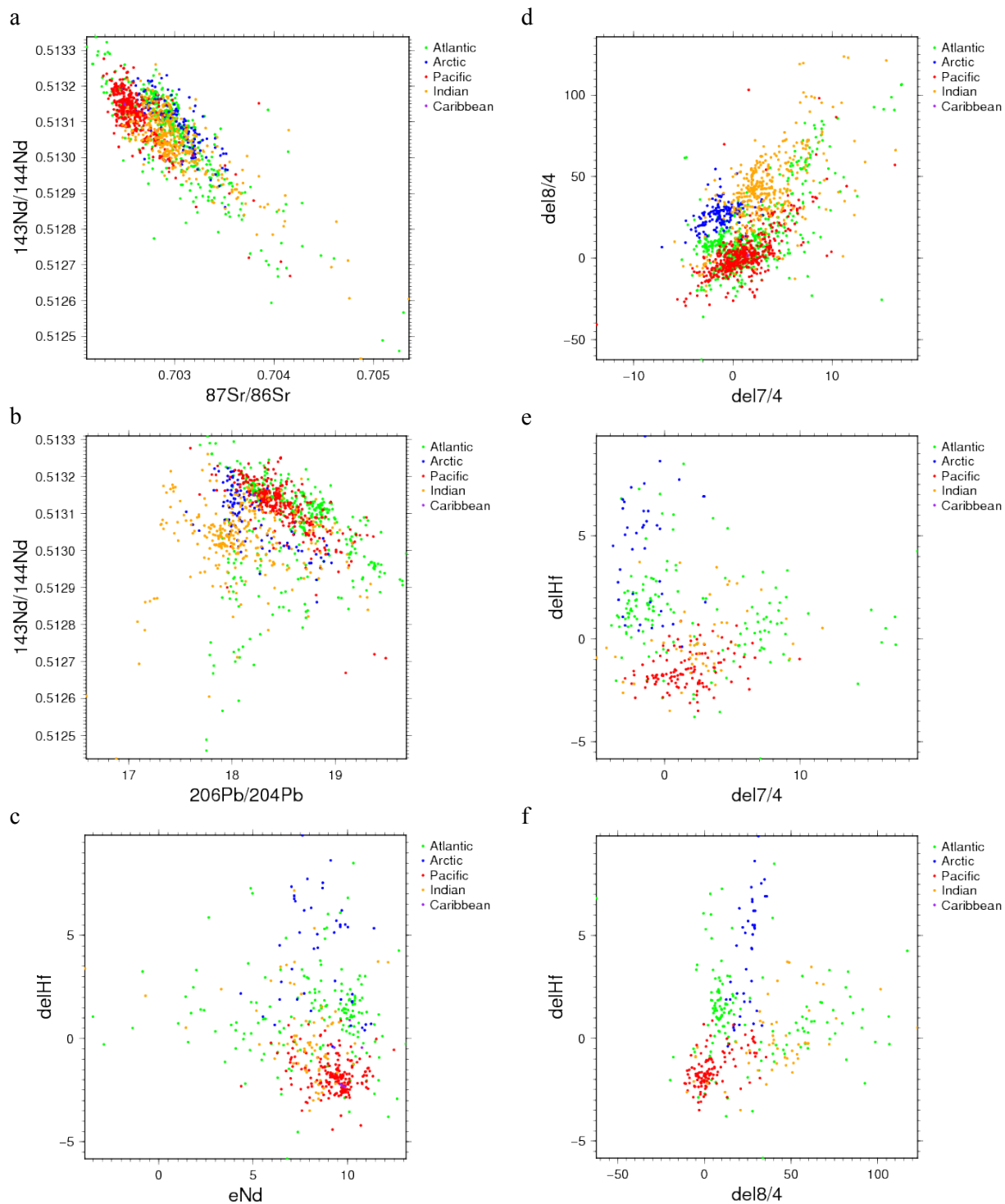
Figure 35: (a) ^{143}Nd/^{144}Nd-^{87}Sr/^{86}Sr, (b) ^{143}Nd/^{144}Nd-^{206}Pb/^{204P}b, (c) ΔεHf-ε$_{Nd}$, (d) Δ8/4-Δ7/4 (e) ΔεHf-Δ8/4 and (f) ΔεHf- Δ8/4 plots of global MORB.

5. Conclusion

The present investigation of some of the main geochemical features of the entire MORB array has sought to systematize the variations in overall source compositions and extent of melting along the different ridge segments. A tentative conclusion based on the fractionation-corrected Ca/Al-ratio, which broadly reflects the degree of partial melting (from parameterization of experimental data by Niu and O'Hara, 2008) is that the mean spreading rate of the major oceanic ridges is positively correlated with degree of partial melting (F). The two end member ridges, the SWIR (full spreading rate < 20 mm/a) and the EPR (80-150 mm/a) with the lowest and highest Ca/Al-ratio, differ also in their proportions of the fertile HIMU and EM1 components (dominating along the EPR and SWIR, respectively), which can modify the fractionation-corrected Ca/Al-ratio (Jackson and Dasgupta, 2008). Also Niu and Hekinian (1997) concluded that the spreading rate is positively correlated with F. Moreover, the more restricted and refractory isotopic compositions of the Pacific compared to the Atlantic and Indian Ocean MORB seem consistent with as high F, as well as more efficient homogenization in a vigorous flow regime.

The water depth and gravity field yield crustal thickness which also seems broadly correlated with the mean melt fraction. The Kolbeinsey Ridge and Mid-Cayman Rise are the shallowest and deepest ridges, respectively, and were identified as the ridges with the highest and lowest melt fractions, respectively, already by Klein and Langmuir (1986).

The Nd-Pb-isotope relations and the parameters $\Delta 7/4$, $\Delta 8/4$ and $\Delta\varepsilon Hf$ are the most useful discriminators betweendifferent proportions of the enriched end members HIMU and EM1in different sample suites along the various ridge segments. The EPR with its simple negative Nd-Pb-isotopic correlation and low $\Delta 8/4$ and $\Delta\varepsilon Hf$ is dominated by the HIMU (ROC) fertile component. The DUPAL-component, which is relatively prevalent along the southern part of the MAR (south of 20 S), the Indian Ocean ridges south of the equator, is characterized by low $^{206}Pb/^{204}Pb$ ratios (and $^{207}Pb/^{204}Pb$ and $^{208}Pb/^{204}Pb$) at low $^{143}Nd/^{144}Nd$ ratios, as well as low $\Delta 8/4$ and $\Delta\varepsilon Hf$. Based on Os-Sr-Nd-Hf isotope relations the Indian Ocean DUPAL-component is thought to have a high LCC/SCLM ratio and originate by shallow convective erosion and mixing into the asthenosphere during rifting of Pangea, creating India, Australia and several microcontinents that subseduently drifted across the present Indian ocean asthenosphere (e.g. Escrig et al. 2002; Hanan et al. 2004; Meyzen et al. 2007; Torsvik et al. 2013). The apparent dominance of the LCC over the SCLM component may seem surprising in view of the fact that removal of most of the SCLM is necessary to expose the LCC. However, per volume or mass unit the LCC may be a far more potent asthenospheric contaminant in terms of shifting the trace element concentration and isotope ratios.

The compositional distinctions between the south Atlantic and Indian Ocean DUPAL-components are unclear. Based on a geochemical comparison between the south Atlantic mantle plumes, the SCLM of southern Africa and the regional DUPAL-signature, Class and Le Roex (2011) concluded that the deep plumes supplied and mixed the DUPAL component into the asthenosphere. Large proportions of the SCLM component are also present in the NE Atlantic and Arctic, especially along the Mohns and Knipovich Ridges as well as the western Gakkel Ridge. ROC seems to be the dominant enriched component in the MORB south of Iceland, along the Reykjanes Ridge and further along the MAR between 53 N and 30 S. An exception to this, however, is that high proportion of SCLM may be preset south of the Azores, near the intersection between the MAR and the Oceanographer Fracture Zone.

The asthenosphere sampled by the current MORB volcanism can thus be divided into a Pacific domain, characterized by relatively restricted and refractory MORB with HIMU/ROC as the dominant component and a combined Atlantic and Indian Ocean domain with variable MORB compositions, covering a larger range from highly refractory to strongly enriched and with variable and locally large proportions of the EM1-type components. This division can be explained by the large-scale mantle structure and the distribution of the continents through the last 340 Ma. As indicated by Meyzen et al. (2007) and Torsvik et al. (2014) the current Pacific and former Panthalassan asthenosphere, overlying the Pacific Large-Low Shear-wave Velocity Province (LLSVP) in the lowermost mantle, has been nearly free of continents during the last 340 Ma. This region is characterized by several active plumes ascending through a wide zone of slowly rising mantle, 4000-5000 km in diameter, causing a residual geoid high. The upward plume and surrounding passive flow brings lower mantle material, including ROC to the asthenoshere. Most of the present Indo-Atlantic asthenosphere, however, was overlain by continents during the same period and Pangaea amalgamated and rifted apart in this hemisphere. The rifting process would naturally be associated with convective erosion of the continental roots. It is possible that the convective mixing of SCLM and LCC was especially efficient in large parts of the Indian Ocean asthenosphere due to rift jumps and the displacement of several microcontinental fragments into the Indian Ocean and the fast movement of India and Australia across much of the area (e.g. Torsvik et al., 2013; 2014). The Central Atlantic however lacks both microcontinents and a SCLM or LCC signature (Pushcharovsky, 2013).

6. Further suggested studies

The current investigation was designed to acquire a broad geochemical picture of the entire MOR-system. More detailed investigations, focusing on specific regions and specific issues, using selected geochemical parameters would allow in-depth insights into the interplay between the character of the heterogeneous mantle, the sub-ridge flow field, as well as the mantle potential temperature and the decompressional melting.

The growing database for abyssal peridotites would facilitate direct and detailed comparison of the petrology and geochemistry of selected MORB samples, possibly including melt inclusions in primary phenocrysts or xenocrysts of olivine, with their corresponding residual peridotites to better understand the source heterogeneities and dynamics of progressive melting. Such a study should be confined to a selected area to be able to account for the small scale variation in abyssal peridotites. Attempts to quantify the influence of source variation as opposed to variation of mantle potential temperature could be made by applying information from such an integrated study of abyssal peridotite variability.

Supplementary tectonic investigations will be important to resolve the questions of why the Indian Ocean MORB composition seems to reflect a high proportion of LCC relative to SCLM and to what degree the Indian Ocean and South Atlantic DUPAL signatures have been generated by different processes. A related question is how the Arctic domain can be the only one with a strong SCLM signature if the complete "Pangaean" domain is more or less affected by continental material due to the presence of continents and continental fragments.A locally more focused study could as well incorporate the Nb/U signal (e.g. Rekämper and Hoffmann, 1997) as an additional parameter for the discrimination of the different lithospheric components in the mantle. On the scales examined here, the Nb/U ratio was too variable for interpretation, but a more detailed study may be able to gain interesting insights from it.

Further clarification of the ambiguous aspects of the MORB signal such as the role of shallow detached material as opposed to deep recycling can improve our understanding of the mantle and plate tectonics. The incorporation of data from mantle plumes far away from MORs and the resulting intra-plate magmatism could be helpful for developing a more in-depth integrated picture that, coupled with geodynamic modeling, would provide useful insights into the interaction between the convecting mantle and the lithosphere.

The improvement and successive completion of the Os isotope dataset on a global scale will be very valuable to clearly distinguish the different enriched components in the upper mantle that shape the MORB variations.

References

Allègre C.J. (1968): Comportement des systèmes U-Th-Pb dans le manteau supérieur et modèle d'évolution de ce dernier au cours des temps géologiques. Earth and Planetary Science Letters, 5, 261-269.

Allègre C.J., Hamelin B., Dupré B. (1984): Statistical analysis of isotopic ratios in MORB: the mantle blob cluster model and the convective regime of the mantle. Earth and Planetary Science Letters, 71, 71–84.

Allègre C.J., Hart S.R., Minster J.-F. (1983): Chemical structure and evolution of the mantle and continents determined by inversion of Nd and Sr isotopic data: II. Numerical experiments and discussion. Earth and Planetary Science Letters, 66, 191–213.

Allègre C.J., Turcotte D.L. (1986): Implications of a two-component marble-cake mantle. Nature, 323, 123-127.

Amante C., Eakins B.W., (2009): ETOPO1 1 Arc-Minute Global Relief Model: Procedures, Data Sources and Analysis. NOAA Technical Memorandum NESDIS NGDC-24. National Geophysical Data Center, NOAA, doi:10.7289/V5C8276M.

Andrault D., Pesce G., Bouhifd M.A., Bolfan-Casanova N., Hénot J.M., Mezouar M. (2014): Melting of subducted basalt at the core-mantle boundary. Science, 344, 6186, 892–895.

Andres M., Blichert-Toft J., Schilling J.-G. (2004): Nature of the depleted upper mantle beneath the Atlantic: evidence from Hf isotopes in normal mid-ocean ridge basalts from 798N to 558S. Earth and Planetary Science Letters,225, 89–103.

Arndt N.T., Goldstein S.L. (1989): An open boundary between lower continental crust and mantle: its role in crust formation and crustal recycling. Tectonophysics, 161, 210–212.

Blichert-Toft J., Agranier A., Andres M., Kingsley R.,Schilling J.-G., Albarède F. (2005): Geochemical segmentation of the Mid-Atlantic Ridge north of Iceland and ridge–hot spot interaction in the North Atlantic. Geochemistry Geophysics Geosystems, 6, Q01E19, doi:10.1029/2004GC000788.

Brandl P.A., Regelous M., Beier C., Haase K.M. (2013): High mantle temperatures following rifting caused by continental insulation. Nature Geoscience, 6, 5, 391-394.

Breivik A.J., Mjelde R., Faleide J.I., Murai Y. (2006): Rates of continental breakup magmatism and seafloor spreading in the Norway Basin–Iceland plume interaction. Journal of Geophysical Research, 111, B7, doi:10.1029/2005JB004004.

Burke K., Steinberger B., Torsvik T.H., Smethurst M.A. (2008): Plume Generation Zones at the margins of Large Low Shear Velocity Provinces on the core–mantle boundary. Earth and Planetary Science Letters, 265, 49-60.

Burton K.W., Cenki-Tok B., Mokadem F., Harvey J., Gannoun A., Alard O., Parkinson I.J. (2012): Unradiogenic lead in Earth's upper mantle. Nature Geoscience, 5, 570–573.

Burton K.W., Schiano P., Birck J.-L., Allègre C.J., Rehkämper M. (2000): The distribution and behavior of Re and Os amongst mantle minerals and the consequences of metasomatism and melting on mantle lithologies. Earth and Planetary Science Letters, 183, 93–106.

Christensen U.R., Yuen D.A. (1985): Layered convection induced by phase transitions. Journal of Geophysical Research, 90, B12, 10291-10300.

Christie D.M., West B.P., Pyle D.G., Hanan B.B. (1998): Chaotic topography, mantle flow and mantle migration in the Australian-Antarctic discordance. Nature, 394, 637–644.

Class C., Le Roex A. (2011): South Atlantic DUPAL anomaly - Dynamic and compositional evidence against a recent shallow origin. Earth and Planetary Letters, 305, 92–102.

Class C., Le Roex A.P. (2009): Shona and Discovery seamount chains, South Atlantic: Superplume source constraints. Geochimica et Cosmochimica Acta, 73, A229.

Collier J.S.,Sansom V., Ishizuka O., Taylor R.N., Minshull T.A., Whitmarsh R.B. (2008): Age of Seychelles–India break-up. Earth and Planetary Science Letters, 272, 264–277.

Cooper K.M., Eiler J.M., Asimow P.D., Langmuir C.H. (2004): Oxygen isotope evidence for the origin of enriched mantle beneath the mid-Atlantic ridge. Earth and Planetary Science Letters, 220, 3, 297-316.

Cottrell E., Kelley K.A. (2013): Redox Heterogeneity in Mid-Ocean Ridge Basalts as a Function of Mantle Source. Science, 340, 6138, 1314-1317.

Courtillot V., Davaille A., Stock J., Besse J. (2003): Three distinct types of hotspots in the Earth's mantle. Earth and Planetary Science Letters, 205, pp. 285–308.

Dalton C.A., Langmuir C.H., Gale A. (2014): Geophysical and Geochemical Evidence for Deep Temperature Variations Beneath Mid-Ocean Ridges. Science, 344, 80, 80-83.

Debaille V., Trønnes R.G., Brandon A.D., Waight T.E., Graham D.W., Lee C.-T. A. (2009): Primitive off-rift basalts from Iceland and Jan Mayen: Os-isotopic evidence for a mantle source containing enriched subcontinental lithosphere. Geochimica et Cosmochimica Acta, 73, 3423–3449.

DePaolo D.J., Wasserburg G.J. (1976): Inferences about magma sources and mantle structure from variations of 143Nd/144Nd. Geophysical Research Letters, 3, 12, 743-746.

Dupré B., Allègre C.J. (1983): Pb–Sr isotope variation in Indian Ocean basalts and mixing phenomena. Nature, 303, 142–146.

Dziewonski A.M., Anderson D.L. (1981): Preliminary reference Earth model. Physics of the Earth and Planetary Interiors, 25, 297–356.

Elliott T., Plank T., Zindler A., White W., Bourdon B. (1997): Element transport from slab to volcanic front at the Mariana Arc. Journal of Geophysical Research, 102, 14991–15019.

Elliott T., Zindler A., Bourdon B. (1999): Exploring the Kappa Conundrum: the role of recycling in the lead isotope evolution of the mantle. Earth and Planetary Science Letters, 169, 129–145.

Escrig S., Capmas F., Dupré B., Allègre C.J. (2004): Osmium isotopic constraints on the nature of the DUPAL anomaly from Indian mid-ocean-ridge basalts. Nature, 431, 59-63.

Faure G., Mensing T.M. (2005): Isotopes: principles and applications. 3rd edition, Revised edition of Principles of isotope geology,2nd edition (1986),Wiley, Hoboken, New Jersey, USA.

French S., Lekic V., Romanowicz B. (2013): Waveform Tomography Reveals Channeled Flow at the Base of the Oceanic Asthenosphere. Science, 342, 227-230.

Fukao Y., Widiyantoro S., Obayashi M. (2001): Stagnant slabs in the upper and lower mantle transition region. Reviews of Geophysics, 39, 3, 291-323.

GEOROC (2014): Geochemistry of Rocks of the Oceans and Continents. Database. Available at: http://georoc.mpch-mainz.gwdg.de/georoc/ (Accessed: January 2014).

Goldstein S.L., Soffer G., Langmuir C.H., Lehnert K.A., Graham D.W., Michael P.J. (2008): Origin of a "Southern Hemisphere" geochemical signature in the Arctic upper mantle. Nature, 453, 89–93.

Graham D.W., Blichert-Toft J., Russo C.J., Rubin K., Albarede F. (2006): Cryptic striations in the upper mantle revealed by hafnium isotopes in Southeast Indian Ridge basalts. Nature, 440, 199–202.

Graham D.W., Hanan B.B., Hémond C., Blichert-Toft J., Albarède F. (2014): Helium isotopic textures in Earth's upper mantle. Geochemistry Geophysics Geosystems, 15, 2048–2074, doi:10.1002/2014GC005264.

Hager B.H., Richards M.A. (1989): Long-wavelength variations in Earth's geoid: Physical models and dynamical implications. Philosophical Transactions of the Royal Society of London, Series A, Mathematical and Physical Sciences, 328, 1599, 309-327.

Hanan B.B., Blichert-Toft J., Hemond C., Sayit K., Agranier A., Graham D.W., Albarède F. (2013): Pb and Hf isotope variations along the Southeast Indian Ridge and the dynamic distribution of MORB source domains in the upper mantle. Earth and Planetary Science Letters, 375, 196-208.

Hanan B.B., Blichert-Toft J., Pyle D.G., Christie D.M. (2004): Contrasting origins of the upper mantle revealed by hafnium and lead isotopes from the Southeast Indian Ridge. Nature, 432, 91-92.

Hart S.R. (1984): A large-scale isotope anomaly in the southern-hemisphere mantle. Nature, 309, 753–757.

Hart S.R. (1988): Heterogeneous mantle domains—signatures, genesis and mixing chronologies. Earth and Planetary Science Letters, 90, 273–296.

Hart S.R., Hauri E.H., Oschmann L.A., Whitehead J.A. (1992): Mantle plumes and entrainment—isotopic evidence. Science, 256, 517–520.

Hart S.R., Schilling J.G., Powell J.L. (1973): Basalts from Iceland and along the Reykjanes Ridge: Sr isotope geochemistry. Nature, 246, 104–107.

Hedlin M.A.H., Shearer P.M., Earle P.S. (1997): Seismic evidence for small-scale heterogeneity throughout the Earth's mantle. Nature, 387, 145–150.

Hekinian R., Stoffers P., Ackermand D., Révillon S., Maia M., Bohn M. (1999): Ridge–hotspot interaction: the Pacific–Antarctic Ridge and the foundation seamounts. Marine Geology, 160(3), 199-223.

Helffrich G., Wiens D.A., Vera E., Barrientos S., Shore P., Robertson S., Adaros R. (2002): A teleseismic shear-wave splitting study to investigate mantle flow around South America and implications for plate-driving forces. Geophysical journal international, 149, 1, F1-F7.

Helffrich G.R., Wood B.J. (2001): The Earth's Mantle. Nature, 412, 501-507.

Hofmann A.W. (1988): Chemical differentiation of the Earth: the relationship between mantle, continental crust, and oceanic crust. Earth and Planetary Science Letters, 90, 297–314.

Hofmann A.W. (1997): Mantle geochemistry: the message from oceanic volcanism. Nature, 385, 219–229.

Hofmann A.W. (2003): Sampling mantle heterogeneity through oceanic basalts: isotopes and trace elements. In: Carlson, R.W., Holland, H.D., Turekian, K.K. (Eds.), Treatise on Geochemistry: The Mantle and Core, Elsevier, 61–101.

Ionov D., Ashchepkov I., Jagoutz E. (2005): The provenance of fertile off-craton lithospheric mantle: Sr-Nd isotope and chemical composition of garnet and spinel peridotite xenoliths from Vitim, Siberia. Chemical Geology, 217, 41–75, doi:10.1016/j.chemgeo.2004.12.001.

Jackson M.G., Carlson R.W., Kurz M.D., Kempton P.D., Francis D., Blusztajn J. (2010): Evidence for the survival of the oldest terrestrial mantle reservoir. Nature, 466, 7308, 853-856.

Jackson M.G., Carlson R.W. (2011): An ancient recipe for flood-basalt genesis. Nature, 476, 7360, 316-319.

Jackson M.G., Dasgupta R. (2008): Compositions of HIMU, EM1, and EM2 from global trends between radiogenic isotopes and major elements in ocean island basalts. Earth and Planetary Science Letters, 276, 1, 175-186.

Jackson M.G., Hart S.R., Koppers A.A., Staudigel H., Konter J., Blusztajn J., Kurz M., Russell J.A. (2007): The return of subducted continental crust in Samoan lavas. Nature, 448, 7154, 684-687.

Jacobsen S.B., Wasserburg G. J. (1979): The mean age of mantle and crustal reservoirs. Journal of Geophysical Research, 84, 7411–7427.

Jaques A.L., Green D.H. (1980): Anhydrous melting of peridotite at 0-15 kb pressure and the genesis of tholeiitic basalts. Contributions to Mineralogy and Petrology, 73, 287-310.

Johnson K., Dick H.J., Shimizu N. (1990): Melting in the oceanic upper mantle: an ion microprobe study of diopsides in abyssal peridotites. Journal of Geophysical Research, 95, 2661-2678.

Jones S.M., White N., Maclennan J. (2002): V-shaped ridges around Iceland: Implications for spatial and temporal patterns of mantle convection. Geochemistry, Geophysics, Geosystems, *3,* 10, 1-23.

Kelley K.A., Plank T, Grove T.L., Stolper E.M., Newman S., Hauri E. (2006): Mantle melting as a function of water content beneath back-arc basins. Journal of Geophysical Research, 111, B09208, doi:10.1029/2005JB003732.

Kempton P.D., Pierce J.A., Barry T.L., Langmuir C., Christie D.M. (2002): Sr-Nd-Pb-Hf isotope results from ODP Leg 187: Evidence for mantle dynamics of the Australian-Antarctic discordance and origin of the Indian MORB source. Geochemistry Geophysics Geosystems, 3, doi:10.1029/2002GC000320.

Klein E.M., Langmuir C.H. (1987): Global correlations of ocean ridge basalt chemistry with axial depth and crustal thickness. Journal of Geophysical Resarch, 92, 8089-8115.

Klein E.M., Langmuir C.H., Zindler A., Staudigel H., Hamelin B. (1988): Isotope evidence of a mantle convection boundary at the Australian–Antarctic discordance. Nature, 333, 623–629.

Knudsen P., Andersen O.B. (2010):A global mean ocean circulation estimation using GOCE gravity model. Available at:
http://www.space.dtu.dk/english/Research/Scientific_data_and_models/downloaddata (Accessed: May 2014).

Langmuir C.H., Klein E.M., Plank T. (1993): Petrological systematics of mid-ocean ridge basalts: constraints on melt generation beneath ocean ridges. In: Geophysical Monograph 71, Mantle Flow and Melt Generation at Mid-Ocean Ridge, Morgan J.P., Blackman D.K., Sinton J.M. (Eds.), American Geophysical Union, Washington, D.C., 183-280.

Laske G., Masters G., Ma Z.,Pasyanos M. (2013):Update on CRUST1. 0-A 1-degree Global Model of Earth's Crust. Geophysical Research Abstracts, 15, 2658.

Liu C.-Z., Snow J.E., Hellebrand E., Brügmann G., von der Handt A., Büchl A., Hofmann A.W. (2008): Ancient, highly heterogeneous mantle beneath Gakkel ridge, Arctic Ocean. Nature, 452, 311–316.

Maclennan J., McKenzie D., Grönvold K., Shimizu N., Eiler J.M., Kitchen N. (2003a): Melt mixing and crystallization under Theistareykir, northeast Iceland. Geochemistry, Geophysics, Geosystems, 4, 11, doi:10.1029/2003GC000558.

Maclennan J., McKenzie D., Hilton F., Gronvöld K., Shimizu N. (2003b): Geochemical variability in a single flow from northern Iceland. Journal of Geophysical Research, 108, ECV-4, doi:10.1029/2000JB000142.

86

Maia M., Pessanha I., Courrèges E., Patriat M., Gente P., Hémond C., Janin M., Johnson K., Roest W., Royer J.-Y., Vatteville J. (2011): Building of the Amsterdam-Saint Paul plateau: A 10 Myr history of aridge-hot spot interaction and variations in the strength of the hot spot source. Journal of Geophysical Research, 116, doi:10.1029/2010JB007768.

Mallick S., Dick H.J.B., Sachi-Kocher A., Salters V.J.M. (2014): Isotope and trace element insights into heterogeneity of subridge mantle. Geochemistry Geophysics Geosystems, 15, 2438–2453, doi:10.1002/2014GC005314.

Meyzen C.M., Blichert-Toft J., Ludden J.N., Humler E., Mevel C., Albarede F. (2007): Isotopic portrayal of the Earth's upper mantle flow field. Nature, 447, 1069–1074.

Michael P.J., Langmuir C.H., Dick H.J.B., Snow J.E., Goldstein S.L., Graham D.W., Lehnert K., Kurras G., Jokat W., Mühe R., Edmonds H.N. (2003): Magmatic and amagmatic seafloor generation at the ultraslow-spreading Gakkel ridge, Arctic Ocean. Nature, 423, 6943, 956-961.

Miller D.M., Goldstein S.L., Langmuir C.H. (1994): Cerium/lead and lead isotope ratios in arc magmas and the enrichment of lead in the continents. Nature, 368, 514–520.

Mitrovica J.X., Forte A.M. (1997): Radial profile of mantle viscosity: results from the joint inversion of convection and postglacial rebound observables. Journal of Geophysical Research, 102, 2751-276.

Montelli R., Nolet G., Dahlen F.A., Masters G. (2006): A catalogue of deep mantle plumes: new results from finite-frequency tomography. Geochemistry Geophysics Geosystems, 7, doi:10.1029/2006GC001248.

Morgan J.P., Morgan W.J. (1999): Two-stage melting and the geochemical evolution of the mantle: a recipe for mantle plum-pudding. Earth and Planetary Science Letters, 170, 215–239.

Müller R.D., Sdrolias M., Gaina C., Roest W.R. (2008): Age, spreading rates, and spreading asymmetry of the world's ocean crust. Geochemistry Geophysics Geosystems, 9, 1525-2027, doi:10.1029/2007GC001743.

Nicolaysen K.P., Frey F.A., Mahoney, J. J., Johnson, K. T. M., & Graham, D. W. (2007): Influence of the Amsterdam/St. Paul hot spot along the Southeast Indian Ridge between 77 and 88 E: Correlations of Sr, Nd, Pb, and He isotopic variations with ridge segmentation. Geochemistry, Geophysics, Geosystems, 8, 9.

Niu Y., Collerson K.D., Batiza R., Wendt J.I., Regelous M. (1999): The origin of E-Type MORB at ridges far from mantle plumes: The East Pacific Rise at 11820'N. Journal of Geophysical Research, 104, 7067-7087.

Niu Y., O'Hara M.J. (2008): Global Correlations of Ocean Ridge Basalt Chemistry with Axial Depth: a New Perspective. Journal of Petrology, 49, 4, 633-664.

Niu, Y., Hekinian, R. (1997): Spreading-rate dependence of the extent of mantle melting beneath ocean ridges. Nature, 385, 326-329.

O'Hara M.J. (1977): Open system crystal fractionation and incompatible element variation in basalts. Nature, 268, 36–38.

O'Nions R.K., Evensen N.M., Hamilton P.J. (1979): Geochemical modeling of mantle differentiation and crustal growth. Journal of Geophysical Resarch, 84, 6091–6101.

Olson P.L., Yuen D.A., Balsiger D.S. (1984): Mixing of passive heterogeneities by mantle convection. Journal of Geophysical Resarch, 89, 425–436.

Pearson D.G., Parman S.W., Nowell G.M. (2007): A link between large mantle melting events and continent growth seen in osmium isotopes. Nature, 449, 202-205.

Peslier A.H., Woodland A.B., Bell D.R., Lazarov M. (2010): Olivine water contents in the continental lithosphere and the longevity of cratons. Nature, 467, 78-81.

PetDB database (2014): Available at: www.earthchem.org/petdb (Accessed: January 2014).

Pushcharovsky Y.M. (2013): Microcontinents in the Atlantic Ocean. Geotectonics, 47, 4, 241-250.

Regelous M., Hofmann A.W., Abouchami W., and Galer J.S.G. (2002): Geochemistry of lavas from the Emperor Seamounts, and the geochemical evolution of Hawaiian magmatism 85–42 Ma. Journal of Petrology, 44, 113–140.

Rehkämper M., Hofmann A.W. (1997): Recycled ocean crust and sediment in Indian Ocean MORB. Earth and Planetary Science Letters, 147, 93–106.

Rohrbach A., Schmidt M.W. (2011): Redox freezing and melting in the Earth's deep mantle resulting from carbon-iron redox coupling. Nature, 472, 7342, 209-212.

Rubin K.H., Sinton J.M., Maclennan J., Hellebrand E. (2009): Magmatic filtering of mantle compositions at mid-ocean-ridge volcanoes. Nature Geoscience, 2, 5, 321-328.

Ryberg T., Tittgemeyer M., Wenzel F. (2000): Finite difference modelling of P-wave scattering in the upper mantle. Geophysical Journal International,141, 787–801.

Salters V.J.M., Dick H.J.B. (2002): Mineralogy of the mid-ocean-ridge basalt source from neodymium isotopic composition of abyssal peridotites. Nature, 418, 6893, 68–72.

Salters V.J.M., Hart S.R. (1991): The mantle sources of ocean ridges, islands and arcs: The Hf-isotope connection. Earth and Planetary Science Letters, 104, 2-4, 364-380.

Salters V.J.M., Mallick S., Hart S.R., Langmuir C.E., Stracke A. (2011): Domains of depleted mantle: New evidence from hafnium and neodymium isotopes. Geochemistry Geophysics Geosystems, 12, Q08001, doi:10.1029/2011GC003617.

Schaefer B.F., Turner S., Parkinson I.J., Rogers N.W.,Hawkesworth C.J. (2002): Evidence for recycled Archaean oceanic mantle lithosphere in the Azores plume. Nature, 420, 304–307.

Schilling J.-G. (1973): Iceland mantle plume: geochemical evidence along Reykjanes Ridge. Nature, 242, 565–571.

Seyler M., Cannat M., Mével C. (2003): Evidence for major-element heterogeneity in the mantle source of abyssal peridotites from the Southwest Indian Ridge (52° to 68°E). Geochemistry, Geophysics, Geosystems, 4, 2, 9101.

Shen Y., Forsyth D.W. (1995): Geochemical constraints on initial and final depths of melting beneath mid-ocean ridges. Journal of Geophysical Resarch, 100, 2211–2237

Shorttle O., Maclennan J. (2011): Compositional trends of Icelandic basalts: Implications for short–length scale lithological heterogeneity in mantle plumes. Geochemistry, Geophysics, Geosystems, 12, 11, doi:10.1029/2011GC003748.

Shorttle O., Maclennan J., Piotrowski A.M. (2013): Geochemical provincialism in the Iceland plume. Geochimica et Cosmochimica Acta, 122, 363–397.

Sigloch K., Mihalynuk M.G. (2013): Intra-oceanic subduction shaped the assembly of Cordilleran North America. Nature, 496, 7443, 50-56.

Simon N.S.C., Carlson R.W., Pearson D.G., Davies G.R. (2007): The origin and evolution of the Kaapvaal cratonic lithospheric mantle. Journal of Petrology, 48, 3, 589–625, doi:10.1093/petrology/egl074.

Sims, K.W.W., Goldstein, S.J., Blichert-Toft, J., Perfit, M.R., Kelemen, P., Fornari, D.J., Michael P., Hart S.R., DePaolo D.J., Layne G., Ball L., Jull M., Bender J. (2002): Chemical and isotopic constraints on the generation and transport of magma beneath the East Pacific Rise. Geochimica et Cosmochimica Acta, 66, 3481–3504.

Sobolev A.V., Hofmann A.W., Nikogosian I.K. (2000): Recycled oceanic crust observed in "ghost plagioclase" within the source of Mauna Loa lavas. Nature, 404, 986–990.

Steinberger B., Calderwood A.R. (2006): Models of large-scale viscous flow in the Earth's mantle with constraints from mineral physics and surface observations. Geophysical Journal International,*167,* 3, 1461-1481.

Storey, M., Saunders A.D., Tarney J., Gibson I.L., Norry M.J., Thirlwall M.F., Leat P., Thompson R.N., Menzies M.A. (1989): Contamination of the Indian Ocean asthenosphere by the Kerguelen-Heard mantle plume. Nature, 338, 574–576.

Stracke A. (2012): Earth's heterogeneous mantle: A product of convection-driven interaction between crust and mantle. Chemical Geology, 330, 274-299.

Stracke A., Hofmann A.W., Hart S.R. (2005): FOZO, HIMU and the rest of the mantle zoo. Geochemistry, Geophysics, Geosystems 6, Q05007.

Stracke A., Snow J.E., Hellebrand E.,von der Handt A., Bourdon B., Birbaum K., Günther D. (2011): Abyssal peridotite Hf isotopes identify extreme mantle depletion. Earth and Planetary Science Letters, 308, 3–4, 359–368.

Sturm M.E., Klein E.M., Graham D.W., Karsten J. (1999): Age constraints on crustal recycling to the mantle beneath the southern Chile Ridge: He-Pb-Sr-Nd isotope systematic. Journal of Geophysical Research, 104, 5097-5114.

Sun W., Hua Y., Kamenetsky V.S., Eggins S.M., Chen M., Arculus R.J. (2008): Constancy of Nb/U in the mantle revisited. Geochimica et Cosmochimica Acta, 72, 3542–3549.

Taylor B., F. Martinez (2003): Back-arc basin basalt systematic. Earth and Planetary Science Letters, 210, 481– 497.

Thirlwall M.F. (1997): Pb isotopic and elemental evidence for OIB derivation from young HIMU mantle. Chemical Geology, 139, 51-74.

Thirlwall M.F., Gee M.A.M., Taylor R.N., Murton B.J. (2004): Mantle components in Iceland and adjacent ridges investigated using double-spike Pb isotope ratios. Geochimica et Cosmochimica Acta, 68, 2, 361-386.

Torsvik T.H., Amundsen H., Hartz E.H., Corfu F., Kusznir N., Gaina C., Doubrovine P.V., Steinberger B., Ashwal L.D., Jamtveit B. (2013): A Precambrian microcontinent in the Indian Ocean. Nature Geoscience, 6, 3, 223-227.

Torsvik T.H., van der Voo R., Doubrovine P.V., Burke K., Steinberger B., Ashwal L.D., Trønnes R.G., Webb S.J., Bull A.L. (2014): Deep mantle structure as a reference frame for movements in and on the Earth. Proceedings of the National Academy of Sciences, 201318135.

van der Meer D.G., Spakman W., van Hinsbergen D.J., Amaru M.L., Torsvik T.H. (2009): Towards absolute plate motions constrained by lower-mantle slab remnants. Nature Geoscience, 3, 1, 36-40.

van Keken P.E., Ballentine C.J., Hauri E.H. (2003): Convective Mixing in Earth's Mantle. In: Carlson, R.W., Holland, H.D., Turekian, K.K. (Eds.), Treatise on Geochemistry: The Mantle and Core, Elsevier, 471-492.

Villagómez D.R., Toomey D.R., Geist D.J., Hooft E.E., Solomon S.C. (2014): Mantle flow and multistage melting beneath the Galapagos hotspot revealed by seismic imaging. Nature Geoscience, 7, 2, 151-156.

Vlastelic I., Dosso L., Guillou H., Bougault H., Géli L., Etoubleau J., Joron J.L. (1998): Geochemistry of the Hollister Ridge: relation with the Louisville hotspot and the Pacific–Antarctic Ridge. Earth and Planetary Science Letters, 160, 3, 777-793.

Warren J.M., Shimizu N. (2010): Cryptic Variations in Abyssal Peridotite Compositions: Evidence for Shallow-level Melt Infiltration in the Oceanic Lithosphere. Journal of Petrology, 10, 1-29.

Weaver S.J., Langmuir C.H. (1990): Calculation of phase equilibrium in mineral-melt systems. Computational Geosciences, 16, 1– 19.

Wessel P. (2001): Global distribution of seamounts inferred from gridded Geosat/ERS-1 altimetry. Journal of Geophysical Research, 106 (B9), 19 431-19 441.

White W.M., Duncan R.A. (1996): Geochemistry and geochronology of the Society Islands: new evidence for deep mantle recycling. In: Basu A. and Hart S.R. (Eds.) Earth Processes: Reading the Isotopic Code, American Geophysical Union, Geophysical Monograph, 95, Washington, 183–206.

Widom E., Shirey S.B. (1996): Os isotope systematics in the Azores: implications for mantle plume sources. Earth and Planetary Science Letters, 142, 3, 451-465.

Willbold M., Stracke A. (2006): Trace element composition ofmantle end-members: implications for recycling of oceanic and upper and lower continental crust. Geochemistry, Geophysics, Geosystems, 7, Q04004, http://dx.doi.org/10.1029/2005GC001005.

Willbold M., Stracke A. (2010): Formation of enriched mantle components by recycling of upper and lower continental crust. Chemical Geology, 276, 188–197.

Wittig N., Pearson D.G., Duggen S., Baker J.A., Hoernle A. (2010): Tracing the metasomatic and magmatic evolution of continental mantle roots with Sr, Nd, Hf and and Pb isotopes: A case study of Middle Atlas (Morocco) peridotite xenoliths. Geochimica et Cosmochimica Acta, 74, 4, 1417-1435.

Workman R.K., Hart S.R., Jackson M., Regelous M., Farley K.A., Blusztajn J., Kurz M., Staudigel H. (2004): Recycled metasomatized lithosphere as the origin of the Enriched Mantle II (EM2) end-member: evidence from the Samoan volcanic chain. Geochemistry, Geophysics, Geosystems, 5, Q04008, http://dx.doi.org/10.1029/2003GC000623.

Xu Z., Zhao Z.F., Zheng Y.F. (2012): Slab–mantle interaction for thinning of cratonic lithospheric mantle in North China: Geochemical evidence from Cenozoic continental basalts in central Shandong. Lithos, 146, 202-217.

Yang D.B., Xu W.L., Pei F.P., Yang C.H., Wang Q.H. (2012): Spatial extent of the influence of the deeply subducted South China Block on the southeastern North China Block: constraints from Sr–Nd–Pb isotopes in Mesozoic mafic igneous rocks. Lithos, 136, 246-260.

Zhang S.-Q., Mahoney J.J., Mo X.-X., Ghazi A.M., Milani L., Crawford A.J., Guo T.-Y., Zhao Z.-D. (2005): Evidence for a Widespread Tethyan Upper Mantle with Indian-Ocean-Type Isotopic Characteristics. Journal of Petrology, 46, 4, 829–858.

Zindler A., Hart S. (1986): Chemical geodynamics. Annual Review of Earth and Planetary Sciences, 14, 493–571.

List of figures

Appendix

An electronic supplement with the data file is available on request.

Appendix 1: Regional overview maps and detailed description

Arctic and Atlantic ridge system north of Iceland

Isotope signal:

The different isotopic signals of Pb of the Arctic ridges are showing almost identical patterns in $^{207}Pb/^{204}Pb$ and $^{208}Pb/^{204}Pb$. The $^{207}Pb/^{204}$ Pb ratio of the segments of the MAR near Iceland is relatively low despite being close to the Iceland hotspot. Further north in the proximity of Jan Mayen both $^{207}Pb/^{204}Pb$ and $^{208}Pb/^{204}Pb$ reach their regional maximum. Towards the Knipovich Ridge and Spitsbergen the enrichment decreases makes way to strong small scale variations with several maxima and minima of different intensity. The Gakkel Ridge is a special case where the $^{207}Pb/^{204}Pb$ and $^{208}Pb/^{204}Pb$ ratios are not correlated: The $^{207}Pb/^{204}Pb$ ratios are intermediate and relatively homogeneous over the whole ridge while the $^{208}Pb/^{204}Pb$ ratio shows a clear separation between the intermediate ratios of the western Gakkel Ridge and the very low values of the eastern Gakkel Ridge.

The Δ7/4 pattern is similar to the $^{207}Pb/^{204}Pb$ pattern on the Knipovich and Gakkel Ridges, while it is not correlated in the areas affected by the Iceland Plume. Unlike the $^{207}Pb/^{204}Pb$ ratio Δ7/4 is not clearly lower close to Iceland compared to Jan Mayen. These deviations continue to the North of Jan Mayen where the $^{207}Pb/^{204}Pb$ ratios decrease towards the Knipovich Ridge while the Δ7/4 values close to Jan Mayen are negative and increase towards the Knipovich Ridge. The same applies to Δ8/4: Δ8/4 and $^{208}Pb/^{204}Pb$ are decoupled between Iceland and the Knipovich Ridge with Δ8/4 having the lowest values in the area around Jan Mayen.

The Sr isotope ratio forms a similar pattern as the $^{208}Pb/^{204}Pb$ ratio. Low $^{87}Sr/^{86}Sr$ values occur close to Iceland and increase towards a maximum at Jan Mayen. North of Jan Mayen the ratio decreases slightly towards the Knipovich Ridge which by itself shows a further declining trend that is interrupted by a point with a higher ratio in the center of the ridge. The Gakkel Ridge is separated equivalent to the $^{208}Pb/^{204}Pb$ signature with relatively high values in the West and extremely low values in the East (0.7025 – 0.7026).

The Sm-Nd systematics of the area reflects the same pattern as the Sr isotopes but with reversed polarity. The $^{143}Nd/^{144}Nd$ (and therefore εNd) values are lower than the background around Jan Mayen and higher in the segments close to Iceland and the Eastern Gakkel Ridge.

The $^{176}Hf/^{177}Hf$ ratio (and subsequently εHf) in the Northern Atlantic depicts a pattern similar to the Nd isotope signal. The data does not cover the Gakkel Ridge. The $^{176}Hf/^{177}Hf$ ratio is low directly N of

Iceland and around Jan Mayen with intermediate ratios in between. The ridges further north have high ^{176}Hf/^{177}Hf ratios. This indicates a strong presence of garnet that holds back Lu in the Iceland plume that also strongly influences Jan Mayen.

No Re-Os data is available for MORB of the region.

REE signal:
The La/Sm and the Ce/Sm ratio as LREE/IREE ratios as indicators of enrichment both show an identical pattern with the highest values occurring in the close proximity of Jan Mayen. Particularly low ratios are found on the western Gakkel ridge, the northernmost part of Mohns Ridge and on the ridge segments between Iceland and Jan Mayen, an area influenced by the melting anomaly of the Iceland plume.

The LREE/HREE ratios Ce/Yb and La/Yb show exactly the same pattern as the LREE/IREE ratios.

The IREE/HREE ratios Gd/Yb (and Gd/Lu) are particularly sensitive to the relative garnet contribution with HREE being highly compatible in garnet. The general pattern of the IREE/HREE ratio is similar to the one shown by the LREE/IREE ratio with the highest ratios at Jan Mayen and the lowest ratios occur on the Kolbeinsey Ridge. Differently from the IREE/HREE ratios the Gakkel Ridge does not have an equally low ratio as the Kolbeinsey Ridge. This may indicate a higher contribution of garnet in the source mantle and deeper seated melting of the MORB closer to Iceland.

Other elements
The CaO-Al2O3 ratio as an indicator of the degree of melting is high between Iceland and Jan Mayen (Kolbeinsey Ridge) and decreases towards the north reaching the lowest values at the Gakkel Ridge.
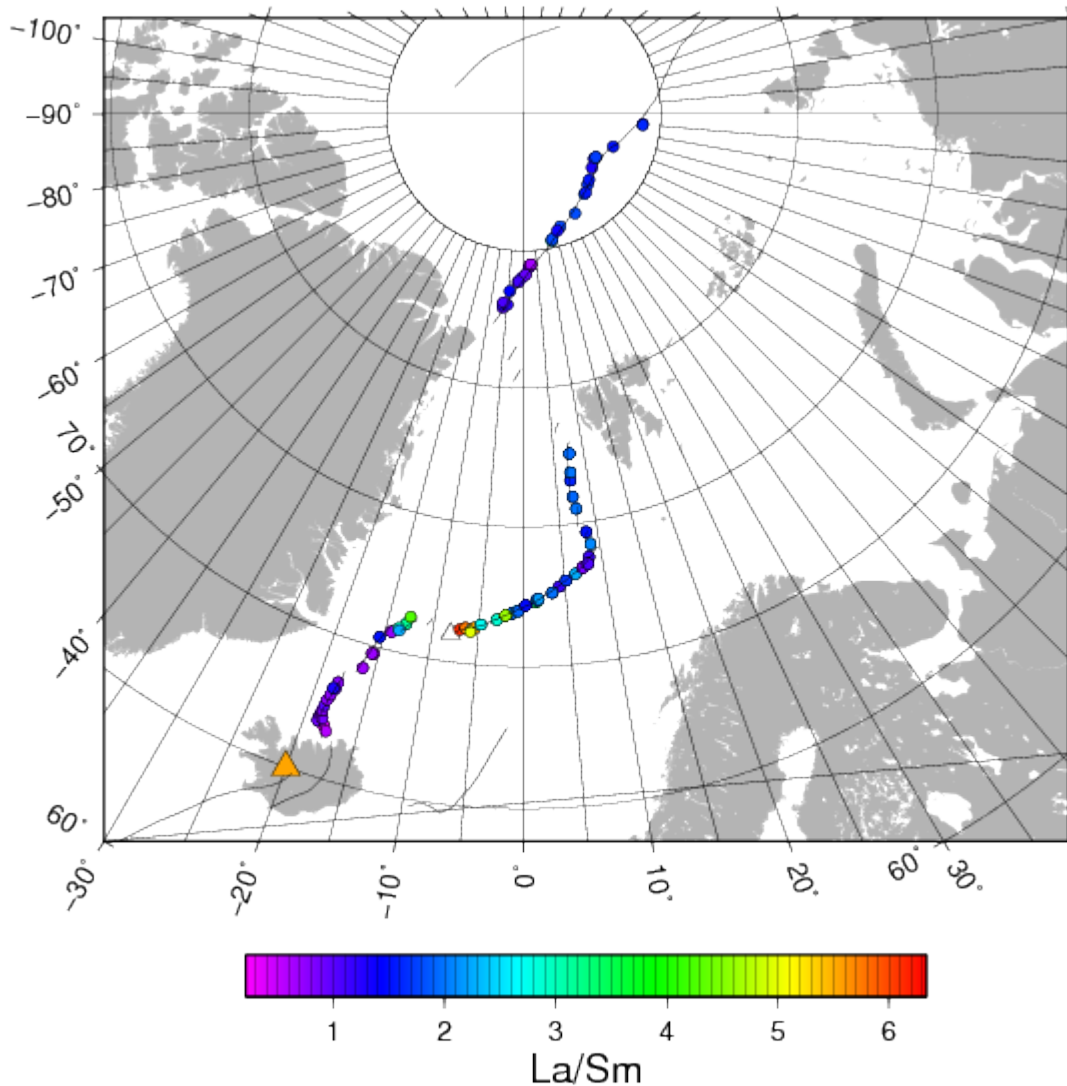
Figure A 1: Map of the Arctic and Atlantic ridge system north of Iceland with sampled localities with La/Sm data marked by colored circles. Other details according to figure 2.

Mid-Atlantic Ridge south of Iceland till Romanche FZ 5°N

Isotope signal:
[207]Pb/[204]Pb and [208]Pb/[204]Pb are showing quite similar patterns. The [207]Pb/[204]Pb ratio of the northern segments of the MAR near Iceland is relatively low despite being close to the iceland hotspot. Between 50° N and 30°N there are higher ratios occurring. These higher ratios are, except for the immediate proximity of the Azores (35-40°N), accompanied by samples with low ratios similar to those from the Reykjanes Ridge. The Δ7/4 generally forms a linear trend from lower Δ7/4 in the north towards higher values in the south. This trend is overlaid by hotspots and their surroundings showing higher Δ7/4 and occasional lower values that seem randomly distributed.

The $^{208}Pb/^{204}Pb$ signal shows a similar picture as the $^{207}Pb/^{204}Pb$, but is more clearly visible in connection with hotspots: Both the Azores and Iceland are in the centre of regional positive anomalies. Additional small scale variation occurs.

The Sr isotope signal shows high $^{87}Sr/^{86}Sr$ values around hotspots with the Iceland plume having a weaker signature than the Azores.

The Sm-Nd systematics of the area reflects the same pattern as the Sr isotopes but with reversed polarity. The $^{143}Nd/^{144}Nd$ values are lower than the background around hotspots indicating the enrichment by plumes.

The $^{176}Hf/^{177}Hf$ ratio (and subsequently εHf) does not show a clear pattern. Although the highest values are in areas affected by hotspots, some of the lowest ratios occur also in close proximity to hotspots. This indicates strong inhomogeneities (i.e garnet content variation) in the local mantle. Especially low ratios are not clearly tied to hotspots though and may indicate lower pressure melting or depleted mantle sources.

Re-Os data for this region is incomplete with the area north of 42°N, including the Reykjanes ridge, being not covered at all. The $^{187}Os/^{188}Os$ ratios vary from ca. 0.13 to 0.135. The highest values occur north of the Azores (at 45°N) while the lowest values are present south of them (between 30 and 37°N).

REE signal:
The La/Sm and the Ce/Sm ratio as LREE/IREE ratios are indicators of enrichment. Both ratios show an identical pattern with the highest values occurring directly north and south of the Azores "plateau" as well as in the center of it. Less distinct peaks indicating minor enrichment are situated on the northern Reykjanes ridge very close to the Icelandic coast and at ca 2°N and a minor peak at ca 13°N (as the isotope anomaly). The lowest ratios are found on the southern Reykjanes Ridge, an area influenced by the melting anomaly of the Iceland plume.

The LREE/HREE ratios Ce/Yb and La/Yb show exactly the same pattern as the LREE/IREE ratios.

The IREE/HREE ratios Gd/Yb (and Gd/Lu) are particularly sensitive to the relative garnet contribution with HREE being highly compatible in garnet. The general pattern of the IREE/HREE ratio is similar to the one shown by the LREE/IREE ratio with the highest ratios on the Azores hotspot and directly N and S of the Azores "plateau", while the lowest ratios occur on the southern Reykjanes Ridge. Differently from the IREE/HREE ratios the variation of areas unaffected by hotspots is much higher with "secondary order" Gd/Yb peaks at 51°N, 30°N, 22°N, 13°N and 2°N. This indicates areas rich in garnet in the local source mantle.
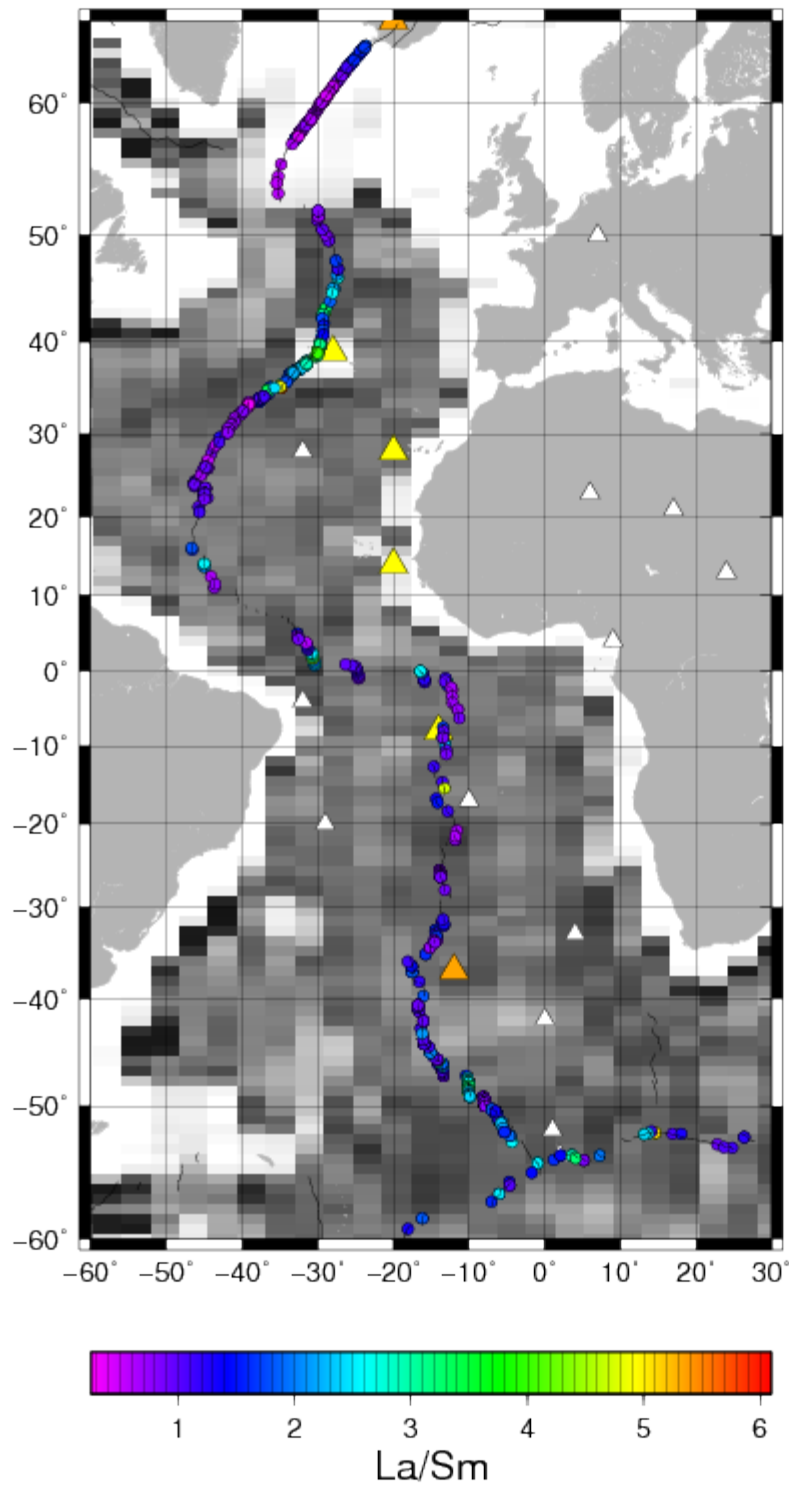
Figure A 2: Map of the Atlantic Ridges south of Iceland with sampled localities with La/Sm data marked by colored circles and oceanic crustal thickness (CRUST1) on a scale from 0 km (black) to 10 km and above (white). Other details according to figure 2.

South Atlantic Ridge and American Antarctic Ridge

Isotope signal:

$^{207}Pb/^{204}Pb$ and $^{208}Pb/^{204}Pb$ show a (strong?) correlation and are much more in accordance with each other than in the northern parts of the MAR. The only strong deviation of the $^{207}/^{204}$ Pb pattern from the $^{208}Pb/^{204}Pb$ pattern is situated at 50°S where high $^{207}Pb/^{204}Pb$ ratios coexist with rather low $^{208}Pb/^{204}Pb$ ratios and there is an anticorrelation between the two ratios. The lowest $^{207}Pb/^{204}Pb$ and $^{208}Pb/^{204}Pb$ ratios occur between 1°S and 6°S north of Ascension. Particularly high $^{207}Pb/^{204}Pb$ and $^{208}Pb/^{204}Pb$ ratios are present close to the Ascension Hotspot and in the southernmost parts of the MAR near the Bouvet and Meteor hotspots. Comparably high $^{207}Pb/^{204}Pb$ and $^{208}Pb/^{204}Pb$ ratios occur also at the equatorial Segment at 16°W, which may or may not be affected by the Ascension hotspot, while at 50°S only $^{207}Pb/^{204}Pb$ reaches a comparable level. The Tristan hotspot does not cause a similar impact with only the $^{208}Pb/^{204}Pb$ ratio being strongly above the background. The remaining areas further away from hotspots show small scale variation of low to intermediate ratios.

Δ 7/4 and Δ 8/4 do not correlate well with $^{207}Pb/^{204}Pb$ and $^{208}Pb/^{204}Pb$ in the southern Atlantic. High Δ 7/4 and $^{207}Pb/^{204}Pb$ ratios occur together at the "anomalous" segment at 50°S and intermediate Δ 7/4 and relatively high $^{207}Pb/^{204}Pb$ ratios coexist at one point NE of Ascension (ca.7°S) and two points in the close vicinity of the Bouvet and Meteor hotspots. The Δ 8/4 pattern in the southern Atlantic correlates very well with the one visible in Δ 7/4 with only the intensities of the various peaks differing stronger. The lowest values for both Δ 7/4 and Δ 8/4 are occurring near the transform boundaries of the Romanche FZ close to the equator and from Ascension southwards between 10°S and 30°S. Unlike the other hotspots of the region the Ascension hotspot influences the Δ 7/4 and 8/4 if at all towards negative values. The main differences between the two Δ indexes are the maximum NE of Ascension (ca.7°S) which has the highest Δ 8/4 in the region (>100) while only having intermediate Δ 7/4 values and the "anomalous" segment at 50°S which has a Δ 8/4 signature that extends much further north towards the Tristan hotspot while it fades out. Over all the Δ 7/4 and 8/4 indexes show only punctual correlation with hotspots and indicate variations that are caused by other factors.

The Sr isotope signal resembles the one visible in Δ 8/4 and 7/4 and south of the Tristan hotspot it shows a distribution of minima and maxima similar to $^{207}Pb/^{204}Pb$ and $^{208}Pb/^{204}Pb$. The highest $^{87}Sr/^{86}Sr$ values in the southern Atlantic are found between 45°S and 50°S with the maximum at 50°S. The Areas closer to hotspots do not show such strong signs of enrichment with the Tristan and Bouvet/ Meteor hotspots having weaker maxima in their vicinities. Ascension even is part of an area ranging from 0°S to 30°S that shows relatively homogeneously low $^{87}Sr/^{86}Sr$ ratios with some of the lowest values of the region being close to the hotspot.

The Sm-Nd systematics of the area reflects the same pattern as the Sr isotopes and Δ 7/4 but with a reversed polarity. The lowest $^{143}Nd/^{144}Nd$ values are indicating the strongest enrichment at 50°S and lesser enrichment by the Tristan, Bouvet and Meteor hotspots.

The $^{176}Hf/^{177}Hf$ ratio (and subsequently εHf) shows a pattern similar to $^{143}Nd/^{144}Nd$. While the highest ratios are present near the equator and Ascension and the lowest ratios at 50°S intermediate ratios occur near hotspots. The particularly low ratios at 50°S may indicate the presence of a garnet rich source mantle that held back Lu.

In the southern Atlantic $^{187}Os/^{188}Os$ ratios are only available for two points very close to 50°S. Having ratios of ca. 0.133 and 0.154 they are unusually dissimilar and possibly indicate at strong small scale heterogeneity.

REE signal:
The La/Sm and the Ce/Sm ratio as LREE/IREE ratios show an identical pattern with the highest values occurring at 15°S. This regional maximum may be related to en of the nearby hotpots (most likely Ascension). Weaker peaks indicating lesser degrees of enrichment are found near the Ascension, the Bouvet and the Meteor hotspots as well as at 50°S (as the isotope anomaly). The low ratios near the Tristan hotspot can possibly be explained by the plume induced higher degree of melting. The areas less affected by hotspots show some variation that may indicate mantle inhomogeneity.

The LREE/HREE ratios Ce/Yb and La/Yb show exactly the same pattern as the LREE/IREE ratios (with the difference of having much higher values for the local peak at 15°E on the SWIR).

The IREE/HREE ratios Gd/Yb (and Gd/Lu) in the southern Atlantic roughly echo the pattern of the LREE/IREE and the LREE/HREE ratios, but with less pronounced maxima and minima. In addition to the maxima at 15°S, 50°S, near the Ascension, the Bouvet and the Meteor hotspots IREE/HREE ratios have a maximum near the Tristan hotspot. The inhomogeneities in the areas further away from hotspots show the same variation pattern as visible in the LREE/IREE and the LREE/HREE ratios.

Central Indian Ridge and Red Sea Rift

Isotope signal:
$^{207}Pb/^{204}Pb$ and $^{208}Pb/^{204}Pb$ show a strong correlation in most of the region with deviations only in the northern half of the Red Sea and one locality near the Rodrigues triple junction in the southernmost part of the CIR. In these localities high $^{207}Pb/^{204}Pb$ ratios coexist with rather low $^{208}Pb/^{204}Pb$ ratios analogue to the "anomalies" in the southern Atlantic. The lowest $^{207}Pb/^{204}Pb$ and $^{208}Pb/^{204}Pb$ ratios can be found on the northern CIR at 9°N indicating a locally depleted mantle. Additionally very low

$^{208}Pb/^{204}Pb$ ratios can be found close to the triple junction on the southernmost CIR. High $^{207}Pb/^{204}Pb$ and $^{208}Pb/^{204}Pb$ ratios are present close to the Afar Hotspot and on a short segment at 17°S. On top of that, high $^{207}Pb/^{204}Pb$ that are not accompanied by high $^{208}Pb/^{204}Pb$ ratios occur in the northern portion of the Red Sea and on one point on the southernmost CIR. The remaining areas further away from hotspots show small scale variation of intermediate ratios.

Δ 7/4 and Δ 8/4 do not correlate well with $^{207}Pb/^{204}Pb$ and $^{208}Pb/^{204}Pb$ except for the fact that their high values indicate enrichment in the immediate surroundings of the Afar plume and at 16°S. Apart from that high Δ 7/4 and $^{207P}b/^{204}Pb$ ratios occur together in the northern part of the Red Sea and near the Rodrigues triple junction at the southern end of the CIR. Except for the northern Red Sea Area which has low Δ 8/4 and high Δ 7/4 the Δ indexes correlate, with only the intensities of the various peaks differing. The lowest values for Δ 7/4 occur in the Gulf of Aden, an area where Δ 7/4 is considerably lower than in the rest of the region when compared to coexisting $^{207}Pb/^{204}Pb$. The minimal values for Δ 8/4 are occurring in the northern and central Red Sea and at ca 6°N coexisting with intermediate $^{208}Pb/^{204}Pb$ ratios. As in the southern Atlantic Δ 7/4 and Δ 8/4 indexes show only punctual correlation with hotspots and indicate variations that are caused by other factors such as possibly the presence of continental lithosphere.

The Sr isotope signal of the CIR resembles the $^{208}Pb/^{204}Pb$ signal more than those of the other isotopes. The highest $^{87}/^{86}$ Sr values occur near the Afar hotspot. High ratios are also present at 16°S and in the northernmost Red Sea. Low ratios indicate relative depletion (or dilution) in the central Red Sea and the northern CIR (especially 5°N to 10°N).

The $^{143}Nd/^{144}Nd$ ratio shows the same pattern as the Sr isotopes and Δ 7/4 but with a reversed polarity. The lowest $^{143}Nd/^{144}$ Nd values indicate the strongest enrichment near the Afar hotspot and at 16°S.

The $^{176}Hf/^{177}Hf$ data in the area is too sparse for interpretation. The highest values occur near the Rodrigues triple junction.

The $^{187}Os/^{188}Os$ ratios of the region do not correlate to any other geochemical tracer (although the low sampling density might simply not show it). Data is only available south of the equator. The highest ratios (0.144 – 0.1452) occur at 4°S and 20°S, while intermediate values (0.135-0.14) occur between 4°S and 20°S as well as near the Rodrigues triple junction at 26°S. Low ratios (0.128) can be found at ca. 2°S.

REE signal:
The La/Sm and the Ce/Sm ratio as LREE/IREE ratios show an identical pattern with the highest values situated north and east of the Afar hotspot (Ce/Yb = 10 -26; La/Yb = 5 – 14.5). In this area the pattern resembles the distribution of the $^{87}Sr/^{88}Sr$ ratios. Apart from the Area influenced by the Afar plume

and one location with intermediate values at 20°S the whole CIR and Red Sea MORB shows remarkably homogeneous low LREE/IREE ratios (Ce/Yb = 0 – 5; La/Yb = 0 – 2).

The LREE/HREE ratios Ce/Yb and La/Yb show exactly the same pattern as the LREE/IREE ratios (with the difference of having much higher values for the local peak at 15°E on the SWIR).

The IREE/HREE ratio Gd/Yb has their regional maxima in the Afar area and slightly north and east thereof as do the LREE/IREE and the LREE/HREE ratios. In addition further maxima occur in the northernmost Red Sea (27°N), at 5°N and at 18-20°S. The additional maxima on the CIR are relatively far away from hotspots and may be correlated to the presence of continental lithosphere (Mauritia/ Indian ocean/Thetis rifting?)? .
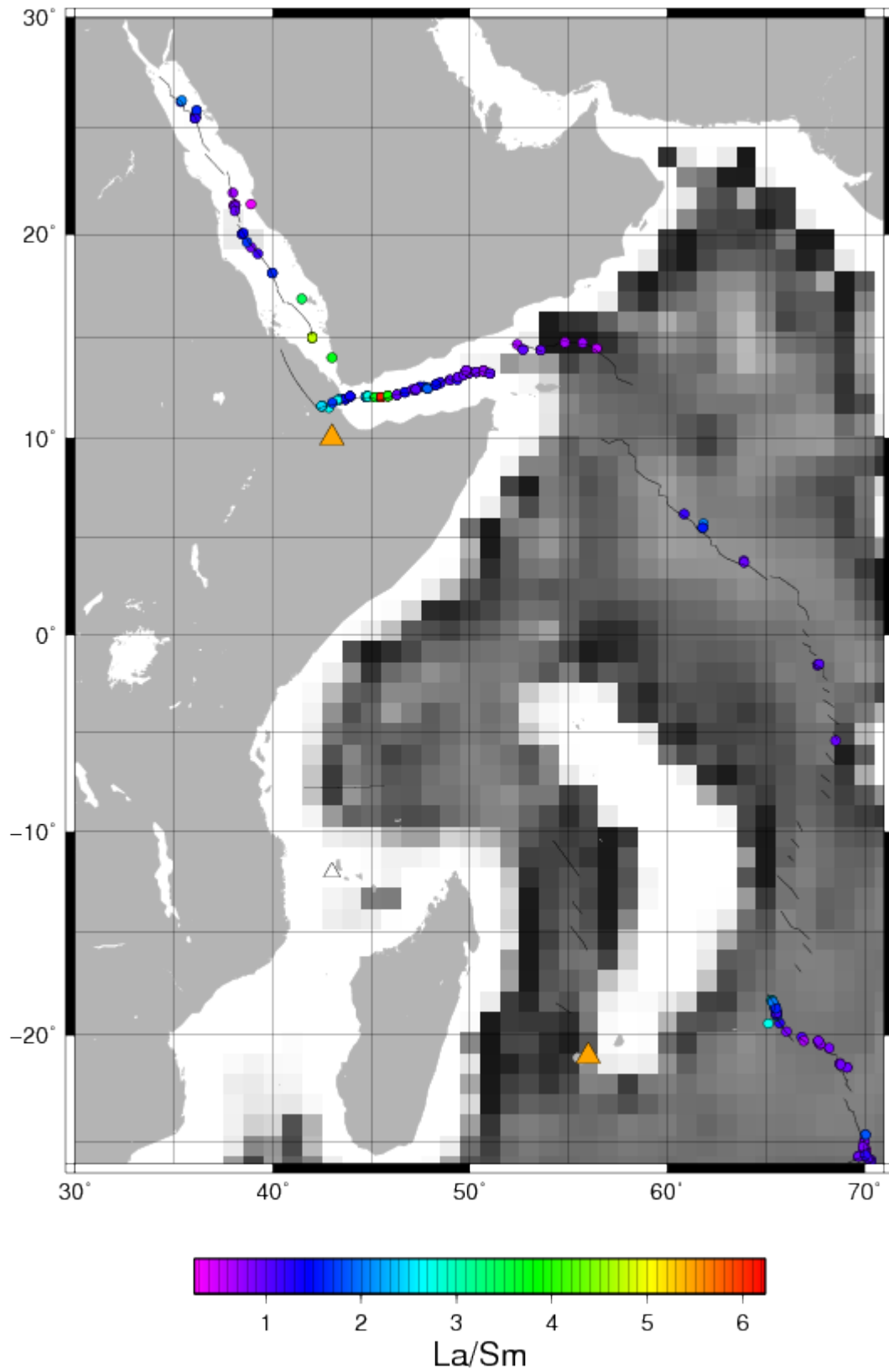
Figure A 3: Map of the Central Indian Ridge area, as well as the Gulf of Aden and the Red Sea with sampled localities with La/Sm data marked by colored circles and oceanic crustal thickness (CRUST1) on a scale from 0 km (black) to 10 km and above (white). Other details according to figure 2.

South-West Indian Ridge

Isotope signal:

The $^{207}Pb/^{204}Pb$ and $^{208}Pb/^{204}Pb$ isotopic signals of the SWIR are showing the same pattern. For both ratios the highest values occur in the easternmost segments (0°E – 20°E) mostly in the vicinities of the Bouvet and the Meteor hotspot while the lowest values are from a segment in the east between 60°E/30°S and 57°E/32°S. Between 20°E and 30°E there is a drop of the ratio accompanied by a local thickening of the crust followed to the east by a peak with a high ratio (27°E; $^{208}Pb/^{204}Pb$=38.4?). The eastern part of the ridge (E of 30°E) in general has lower ratios than the western part and the sub-regional variation forms local maxima at 38-40°E, 42°E, 45-52°E and east of 63°E towards the Rodrigues triple junction while minima occur at 32°E, 41°E, 43°E and most significantly 57-60°E. The maxima are most likely related to the proximity of the Marion, Crozet and possibly Kerguelen hotspots and potentially also to the presence of a continental fragment attached to Madagascar at 45-52°E.

Δ 7/4 and Δ 8/4 do not follow the pattern of $^{207}Pb/^{204}Pb$ and $^{208}Pb/^{204}Pb$ although they also have their highest values in similar regions generally in proximity to the hotpots. The Δ values show similar patterns when viewed along the ridge with the main difference apart from differing magnitudes of the minima and maxima being the fact that Δ 7/4 shows low values in the northeast (57°E – 70°E) while Δ 8/4 has intermediate values. Sub-regional maxima of both Δ values are present in the immediate vicinity of the Bouvet hotspot to the west of the highest $^{207}Pb/^{204}Pb$ and $^{208}Pb/^{204}Pb$ ratios and at 27°E (corresponding with the $^{207}Pb/^{204}Pb$ and $^{208}Pb/^{204}Pb$ peak). These maxima have the highest Δ 7/4 values of the region. The sub-regional maxima further east occur at 41°E and 45°E. These maxima are more pronounced in Δ 8/4 than Δ 7/4 with the regional maximum of Δ 8/4 being at 41°E. In the easternmost segments (east of 60°E) Δ 8/4 shows further minor maxima with intermediate values that are comparable in magnitude with the maxima in the Western part of the ridge. Δ 7/4 in this area is continuously low to very low.

The Sr isotope signal shows the highest $^{87}Sr/^{86}Sr$ values at 41°E and has lesser maxima close to the Bouvet hotspot and at 27°E giving it a strong resemblance to the pattern formed by Δ 7/4.

The Sm-Nd exactly mirrors the Sr isotopes but with reversed polarity.

The $^{176}Hf/^{177}Hf$ ratio is generally low to intermediate in the western part of the SEIR (West of 30°E) while it is generally high in the eastern part. The regional maximum occurs at 45°E. Sub-regional variation adds to this pattern a minor maximum with intermediate-high values at 22 -25°E and minima at 41°E and 55°E. This pattern roughly resembles the one visible in $^{208}Pb/^{204}Pb$ but with reversed polarity. In total the Hf isotope pattern does not show clear correlation with any other isotope system

or the presence of hotspots. The Hf isotope pattern is most likely the result of variation in the upper mantle with possibly higher amounts of garnet present at low ^{176}Hf/^{177}Hf ratios.

187Os/188Os data is only available for the part of the ridge from 40°E to 50°E. The westernmost section of this part of the SWIR (ca. 41°E) contains the highest ^{187}Os/^{188}Os ratios of the global MORB dataset with ^{187}Os/^{188}Os=0.334. The rest of the samples of the SWIR fit well in the array of 0.12 to 0.15 that is common for the rest of the MORs.

REE signal:
The LREE/IREE ratios La/Sm and the Ce/Sm show an identical pattern with the highest values occurring between 3°E and 5°E directly west of the Bouvet hotspot, at 15°E and at 37°E near the Marion hotspot. The lowest ratios occur at 50°E and other locations with very low rations are to be found at 5°E, 23°E, between 50 and 60°E and near the Rodrigues triple junction at ca. 70°E. This pattern does not correlate with any of the isotope systems, although it has a peak distribution very similar to ^{207}Pb/^{204}Pb and ^{208}PB/^{204}Pb in the western part of the ridge (west of 30°E). There are maxima near hotspots that indicate enrichment. The high ratios near 15°E are not near a hotspot and may represent mantle inhomogeneity.

The LREE/HREE ratios Ce/Yb and La/Yb show exactly the same pattern as the LREE/IREE ratios.

The garnet sensitive IREE/HREE ratio Gd/Yb shows a pattern roughly similar to the one shown by the LREE/IREE ratio. The highest ratios occur at 3°E near the Bouvet hotspot, at ca 15°E and at 41°E while the lowest ratios occur at 6°E. Further minima of the IREE/HREE ratios occur at 50°E and les significantly at 27°E, 48°E, around 60°E and at the Rodrigues triple junction at 70°E. The IREE/HREE ratios seem to be less influenced by the presence of hotspots that the other discussed systems, although most of the extreme ratios occur in areas potentially influenced by hotspots. High ratios indicating a mantle source that is rich in garnet can be found near hotspots and at 15°E.

The enrichment tracer CaO/Al2O3 indicates enrichment in the areas close to hotspots between 0°E and 11°E, between 30°E and 40°E and between 41°E and 51°E and at the triple junction near 70°E. On top of that CaO/Al2O3 indicates enrichment at 57°E and slight enrichment between 17°E and 23°E. Depletion is indicated between 12 and 14°E, between 60 and 69°E and less prominently at 40°E.
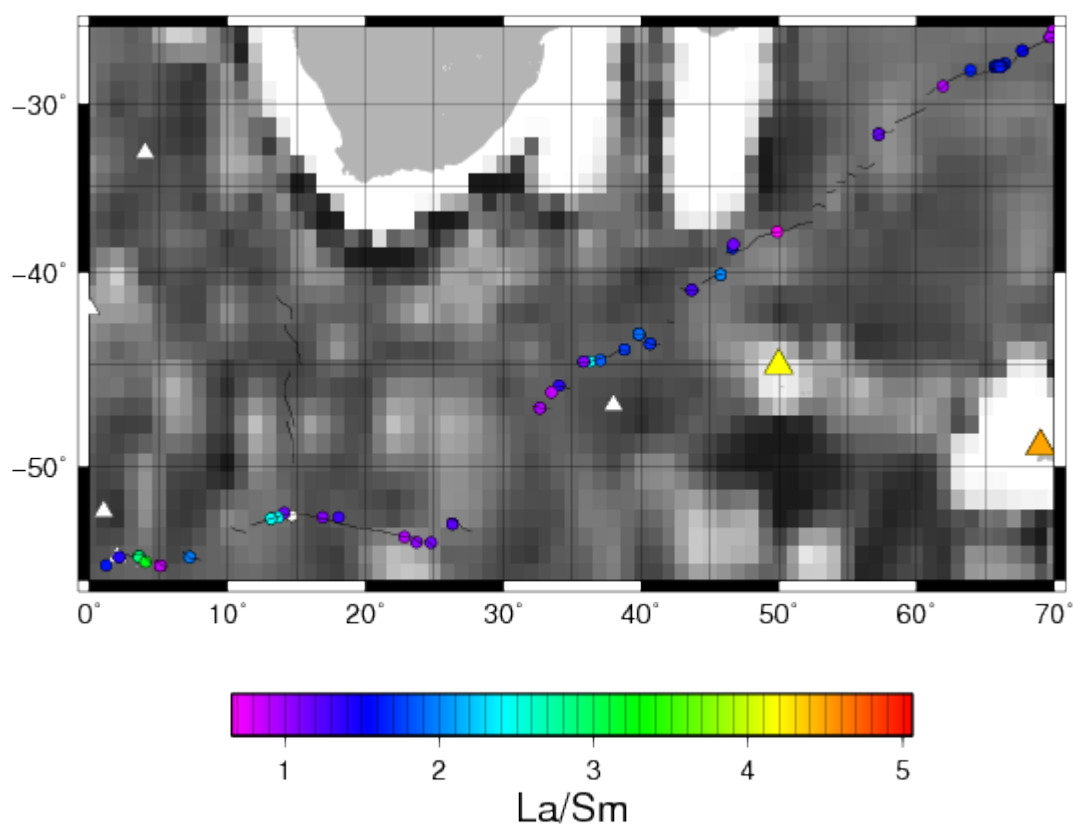
Figure A 4: Map of the South West Indian Ridge area with sampled localities with La/Sm data marked by colored circles and oceanic crustal thickness (CRUST1) on a scale from 0 km (black) to 10 km and above (white). Other details according to figure 2.

South-east-Indian Ridge (SEIR)

Isotope signal:

$^{207}Pb/^{204}Pb$ and $^{208}Pb/^{204}Pb$ in the SEIR are relatively well correlated with the spatial patterns showing minima and maxima at identical locations. The major differences are the intensities of the maxima and minima. The $^{207}Pb/^{204}Pb$ signal shows fewer and more spatially constrained strong maxima and minima than $^{208}Pb/^{204}Pb$. The main maxima in both ratios occur at ca. 79°E near the Kerguelen and Amsterdam-St. Paul hotspots and at ca. 135°E. Less pronounced sub-regional maxima occur at 95°E and between 105°E and 108°E. The remaining areas show small scale variation of low to intermediate ratios with roughly matching $^{207}Pb/^{204}Pb$ and $^{208}Pb/^{204}Pb$ patterns. $^{207}Pb/^{204}Pb$ ratios in these areas show very pronounced minima at 118°E and 126°E and smaller scale variation of intermediate and low ratios apart from that. The $^{208}Pb/^{204}Pb$ ratios, with the lowest values occurring at ca. 72°E, between 90°E and 95°E, between 95°E and 100°E, at 117°E and around 135°E, additionally show minima that extend over larger areas.

Δ 7/4 and Δ 8/4 of the SEIR are similar to each other in the same way as $^{207}Pb/^{204}Pb$ and $^{208}Pb/^{204}Pb$, with Δ 8/4 showing more pronounced low values over large areas. The regional Δ 7/4 and Δ 8/4 patterns share the main feature of the maximum at 79°E near the Kerguelen and Amsterdam-St. Paul hotspots with the Pb isotope ratios, but do not correlate with them for the rest of the region. In some smaller areas such as between 90°E and 100°E there is rather an anticorrelation. Both Δ indexes have a secondary maximum between 115°E and 118°E which is close but not identical to the maximum between 105°E and 108°E seen in the Pb isotope ratios. The lowest values for both Δ 7/4 and Δ 8/4 can be found on the easternmost SEIR to the east of 125°E, i.e. the Australian-Antarctic Discordancy (AAD). Strong mismatches between Δ 7/4 and Δ 8/4 occur between 90°E and 95°E and at 135°E where high Δ 7/4 and low Δ 8/4 values coexist. Similar constellations with high Δ 7/4 and intermediate Δ 8/4 values coexisting occur in the northwestern segments of the SEIR at 75°E/29°S and 78°E/35°S.

The Sr isotope signal shows one major peak with high ratios at 79°E near the Kerguelen and Amsterdam-St. Paul hotspots and thus resembles the one visible in Δ 8/4 and 7/4. Apart from this the $^{87}Sr/^{86}Sr$ ratios do not correlate with any of the Pb isotope patterns. The highest $^{87}Sr/^{86}Sr$ values in the region occur at 79°E near a hotspot, while the second highest ratios are found at 130°E in a unique location far away from hotspots. In accordance with the Δ Pb values the lowest $^{87}Sr/^{86}Sr$ ratios can be found east of 125°E (with the exception of aforementioned high ratio at 130°E). In the remaining areas the Sr isotope pattern describes small scale variation of relatively low values. This variation pattern resembles the one of Δ 8/4 in the central SEIR between 85°E and 100°E, while apart from this it is independent from the other isotopes.

The Sm-Nd systematics of the area reflects the same pattern as the Sr isotopes but with a reversed polarity with the lowest $^{143}Nd/^{144}Nd$ values indicating the strongest regional enrichment at 79°E. East of 125°E the "anticorrelation"/reversed correlation does not apply as clearly as in the rest of the region and in the regions discussed before. This segment east of the AAD generally has high $^{143}Nd/^{144}Nd$ ratios, but between 124°E and 126°E the situation is more complex: Extremely high ratios (0.51324) occur here very close to intermediate ratios.

The $^{176}Hf/^{177}Hf$ data of the SEIR does not cover the central SEIR between 80°E and 115°E. The existing data shows a pattern similar to $^{143}Nd/^{144}Nd$. The highest ratios are present at around 126°E and the lowest ratios at 79°E. Apart from these extreme values the ratios in the eastern part of the ridge are generally lower than those in the western part. The low ratios at 79°S may indicate the presence of a garnet rich source mantle in the Kerguelen plume while the high ratios around 126°E possibly hint at a depleted mantle source (possibly subcontinental or sub-oceanic-crust?) or very shallow melting of slowly rising peridotites.

Re-Os data is only available for the SEIR west of 80°E. The ^{187}Os/^{188}Os ratios close to the Amsterdam St.Paul hotspot (78°E) are slightly higher (ca. 0.16) than those at the Rodrigues triple junction (70°E; ^{187}Os/^{188}Os=0.135-0.14).

REE signal:

Unlike in all other regions the La/Sm and the Ce/Sm ratios of the SEIR do not show an identical pattern. The La/Sm ratio along the SEIR has one distinct maximum (>3) at 106°E, and further secondary maxima (>2) near the Amsterdam-St. Paul hotspot (79°E), at 96°E, at 105°E, at 108°E and at 121°E. Very low ratios (<1) are predominant in wide areas in between the maxima: Between 70°E and 76°E, between 78°E and 92°E, between 97°E and 98°E, between 108°E and 111°E and between 125°E and 140°E. Intermediate values (1-2) are most commonly occurring in the central SEIR between 96°E and 125°E. The low ratios in widespread areas combined with locally occurring higher ratios hint at mantle inhomogeneity with a generally depleted mantle that is locally enriched. The Ce/Sm ratio along the ridge shows a somewhat different pattern, but tells a similar story. The highest Ce/Sm ratios (>5) occur near the Amsterdam-St. Paul hotspot (79°E), at 96°E, at 108°E and at 121°E. Very low ratios (<3) occur near the Rodrigues triple junction (72°E), south of the Amsterdam-St. Paul hotspot (79°E/41°S), at 89°E, at 103°E, at 108°E and at between 125°E and 133°E. Intermediate ratios (3-4) are predominant in the central part of the SEIR between 90°E and 125°E, although they are highly variable on a small scale (ca. 1°) and are intermingled with several points of high and low ratios.

The LREE/HREE ratios Ce/Yb and La/Yb show almost exactly the same pattern as the LREE/IREE ratio Ce/Sm with the difference of having different relative amplitudes for the diverse maxima and minima.

The Gd/Yb ratio in the SEIR area has relatively high (>1.5) values at 73°E, near the Amsterdam-St. Paul hotspot (79°E/39°S), between 118°E and 125°E and at 136°E. Low ratios (<1.5) indicating a potentially garnet rich source mantle are present at 72°E, north of the Amsterdam-St. Paul hotspot (79°E) between 28°S and 37°S, south of the Amsterdam-St. Paul hotspot (79°E/40°S), at 116°E, between 125°E and 136°E and at 138°E. Although the central SEIR between 80°E and 115°E is not covered the IREE/HREE ratio Gd/Yb shows a pattern that roughly resembles the other REE ratios or the reversed ^{143}Hf/^{144}Hf pattern and somehow also the Pb isotope patterns. The inhomogeneities in the areas further away from hotspots show the same variation pattern as visible in the LREE/IREE and the LREE/HREE ratios.

CaO/Al2O3 as tracer of enrichment does not indicate a particularly high degree of enrichment close to the Amsterdam-St. Paul hotspot. The most extreme values occur independent from hotspots with the highest ratios being measured at 92°E, 97°E, 103°E and 133°E, and the lowest ratios being measured

110

at 96°E, 101°E and 124°E to 126°E. The overall pattern indicates a complex sequence of inhomogeneities in the source and/or the melting behavior at a scale of 1 to 10 degrees.
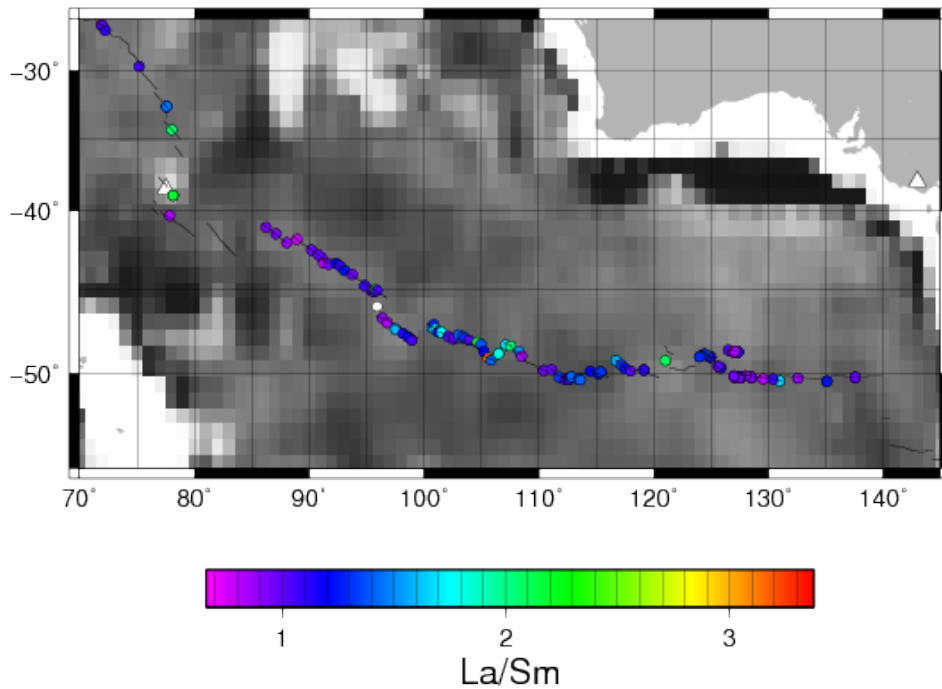

Figure A 5: Map of the South East Indian Ridge area with sampled localities with La/Sm data marked by colored circles and oceanic crustal thickness (CRUST1) on a scale from 0 km (black) to 10 km and above (white). Other details according to figure 2.

East pacific Rise

Isotope signal:
The ^{207}Pb/^{204}Pb and ^{208}Pb/^{204}Pb isotopic signals of the EPR are showing similar patterns. For both ratios the locations of sub-regional and local maxima and minima occur in identical locations although their amplitudes are vastly differing. ^{207}Pb/^{204}Pb shows maxima near the Louisville hotspot at ca. 140°W/55°S, near the Easter hotspot (ca. 110°W – 117°W; 25°S – 35°S), at 115°W/14°S, at 106°W/8°N and at 108°W/23°N near the Socorro hotspot. The most pronounced minima are situated at the eastern edge of the Easter microplate (116°W/26°S), between 17°S and 14°S, and between 14°S and 10°S. The ^{208}Pb/^{204}Pb signal shows much more locally constrained maxima near the Louisville hotspot at ca. 140°W/55°S, near the Easter hotspot (ca. 112°W – 117°W; 25°S – 28°S) and near the Socorro hotspot (108°W/23°N). The most significant minima occur at around 133°W/55°S, at the western edge of the Easter microplate (116°W/26°S) and between 17°S and 10°S. The remaining areas show variations of intermediate and low ratios that are in the order of 5° in scale.

Δ 7/4 and Δ 8/4 do not follow the pattern of $^{207}Pb/^{204}$Pb and $^{208}Pb/^{204}$Pb. The Δ values also show differing patterns along the EPR. The highest Δ 7/4 values at the eastern edge of the Easter microplate (116°W/26°S), at 115°W/14°S and at 108°W/23°N near the Socorro hotspot correspond to points with high 207Pb/204Pb. When viewed along the ridge with the main difference apart from differing magnitudes of the minima and maxima being the fact that Δ 7/4 shows low values in the northeast (57°E – 70°E) while Δ 8/4 has intermediate values. Sub-regional maxima of both Δ values are present in the immediate vicinity of the Bouvet hotspot to the west of the highest $^{207}Pb/^{204}$Pb and $^{208}Pb/^{204}$Pb ratios and at 27°E (corresponding with the $^{207}Pb/^{204}$Pb and $^{208}Pb/^{204}$Pb peak). These maxima have the highest Δ 7/4 values of the region. The sub-regional maxima further east occur at 41°E and 45°E. These maxima are more pronounced in Δ 8/4 than Δ 7/4 with the regional maximum of Δ 8/4 being at 41°E. In the easternmost segments (east of 60°E) Δ 8/4 shows further minor maxima with intermediate values that are comparable in magnitude with the maxima in the Western part of the ridge. Δ 7/4 in this area is continuously low to very low.

The Sr isotope signal shows the highest $^{87}Sr/^{86}$Sr values near the Louisville hotspot (ca. 140°W/55°S) and has lesser maxima near the Socorro hotspot (108°W/23°N), near the Socorro hotspot (108°W/23°N), near the Easter hotspot (ca. 112°W – 117°W; 25°S – 28°S) and at 106°W/8°N. Very low ratios (<0.7025) can be found most areas not in the vicinities of hotspots (SW EPR (W of 170°W), S of Lousville (ca. 140 – 142°W/57°S), E of Louisville (115-130°W/52-58°S), central EPR 20°S – 35°S except for areas influenced by the Easter hotspot, 11°S -17°S, 3°N – 3°S and most points between 9°N and17°N. The overall $^{87}Sr/^{86}$Sr pattern of the EPR resembles the pattern of 208Pb/204Pb with tightly defined peaks near the hotspots and at 106°W/8°N as well as with minor variation correlatedly occurring in the same areas.

$^{143}Nd/^{144}$Nd almost exactly mirrors the Sr isotopes but with reversed polarity. The main difference is that the Socorro hotspot does not show a significant $^{143}Nd/^{144}$Nd signature.

As there is no Hf isotope data available for the southern EPR south of 30°S only the central and northern EPR can be discussed. The $^{176}Hf/^{177}$Hf ratios are highest in several individual locations to the west and northwest of the Easter hotspot (EPR between 10°S and 27°S, i.e. 116°W/26°S) while they are lowest at 106°W/8°N. Further less extreme low values occur on the eastern margin of the Easter microplate. This pattern resembles the one visible in $^{208}Pb/^{204}$Pb but with reversed polarity. In total the Hf isotope pattern does not show clear correlation with any other isotope system. The Hf isotope pattern is most likely the result of variation in the upper mantle with possibly higher amounts of garnet present at low $^{176}Hf/^{177}$Hf ratios, for example near the Easter plume. Low $^{176}Hf/^{177}$Hf ratios in the EPR are correlated with enrichment.

^{187}Os/^{188}Os data is only available for few localities on of the EPR north of the Easter micro plate. The ^{187}Os/^{188}Os ratios vary between 0.127 and 0.141 with the highest ratios occurring at ca. 13°N and the lowest ratios being present close to the Galapagos Triple Junction (2°N). North of the Easter microplate (15°N-20°N) intermediate ratios (0.132-0.134) occur. At the far northern end of the EPR (21°N) low (ca. 0.13) and intermediate (ca. 0.136) values coexist.

REE signal:

The LREE/IREE ratios La/Sm and the Ce/Sm show an identical pattern with the high values occurring close to the Louisville hotspot (140°E/55°S), close to the Easter hotspot (ca. 112°W – 117°W; 25°S – 28°S), at around 8°S and at 8-10°N. Low ratios occur in most other areas of the EPR north of 35°S. This pattern does not correlate with any of the isotope systems, although it has a peak distribution very similar to ^{208}Pb/^{204}Pb in most parts of the ridge. There are maxima near hotspots (although some are very minor, and the one near Socorro is not significant) that indicate enrichment. The high ratios at 8-10°S and at 8-10°N may represent mantle inhomogeneity.

The LREE/HREE ratios Ce/Yb and La/Yb show exactly the same pattern as the LREE/IREE ratios but with slight differences in the intensities of the peaks.

The garnet sensitive IREE/HREE ratio Gd/Yb shows a pattern roughly similar to the one shown by the LREE/IREE ratios. The highest ratios occur close to the Easter hotspot, but more south than the enrichment indicated by other tracers. High ratios indicating a mantle source that is rich in garnet can be found near hotspots (26°S – 32°S and 22°N), between 37°S and 40°S, at 13°S and at 8-10°N. Low ratios occur at the NE margin of the Easter microplate and north of it (20°S -25°S), near the Juan Fernandez triple junction (2°N), and near the Socorro hotspot (22°N).
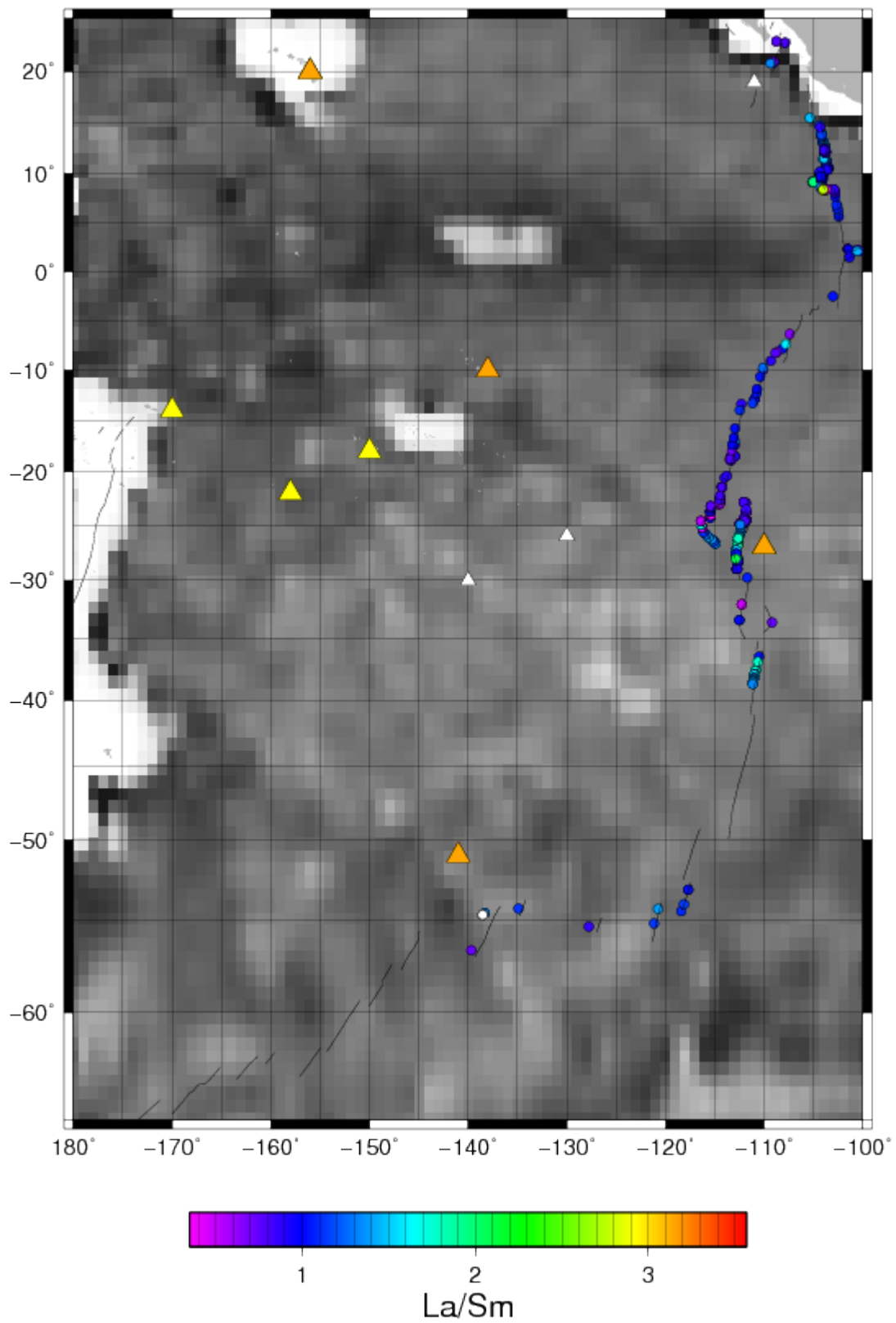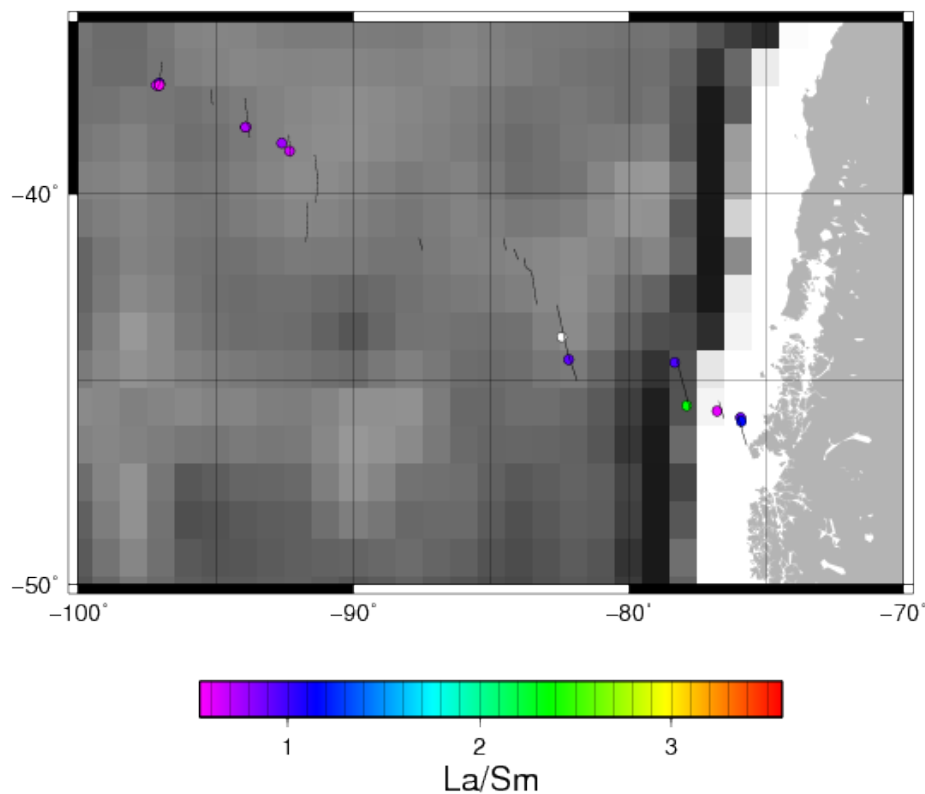
Figure A 6: Map of the East Pacific Rise area with sampled localities with La/Sm data marked by colored circles and oceanic crustal thickness (CRUST1) on a scale from 0 km (black) to 10 km and above (white). Other details according to figure 2.

114

Chile Ridge

Isotope signal:

The $^{207}Pb/^{204}Pb$ and $^{208}Pb/^{204}Pb$ isotopic signals of the Chile Ridge form very similar patterns along the ridge. Both ratios show the highest values ($^{207}Pb/^{204}Pb > 15.65$; $^{208}Pb/^{204}Pb > 39$) at 78°W and a less pronounced maximum at 82°W ($^{207}Pb/^{204}Pb > 15.64$; $^{208}Pb/^{204}Pb > 38.3$). The lowest ratios ($^{207}Pb/^{204}Pb < 15.5$; 208Pb/204 Pb < 37.7) occur between 82 and 83°W and at 77°W. In the western part of the ridge (90°W – 100°W), at 82.5°W, between 78 and 79°W and in the easternmost segment (77 – 78°W) intermediate to low ratios occur. The maxima indicating enrichment are most likely related to variation in the upper mantle or a low degree of melting.

The Δ 7/4 values of the Chile ridge have their relative sub-regional maxima and minima in identical locations as the $^{207}Pb/^{204}Pb$ ratios. The intensities of them differ, so that the highest Δ 7/4 values can be found 82°W while the highest $^{207}Pb/^{204}Pb$ ratios occur at 78°W. Δ 8/4 shows much larger deviation in the relative intensities of the maxima and minima than Δ 7/4 when compared to $^{207}Pb/^{204}Pb$ and $^{208}Pb/^{204}Pb$ although they still occur in the same regions. The highest Δ 8/4 values can be found at 82.5°W and 77°W where they coexist with intermediate to low Δ 7/4, $^{207}Pb/^{204}Pb$ and $^{208}Pb/^{204}Pb$. The lowest Δ 8/4 values of the region occur in the westernmost segments (90°W-100°W) and coexist with intermediate to low Δ 7/4, $^{207}Pb/^{204}Pb$ and $^{208}Pb/^{204}Pb$.

The Sr isotope signal echoes the patterns formed by Δ 7/4, $^{207}Pb/^{204}Pb$ and $^{208}Pb/^{204P}b$ with the highest ratios occurring at 78°W. The most notable differences are the stronger pronounced peaks at 82.5°W and 76°W.

143Nd/144Nd exactly mirrors the reversed pattern of 87Sr/86Sr (with the exception of the 76°W maximum), Δ 7/4, $^{207}Pb/^{204}Pb$ and $^{208}Pb/^{204}Pb$.

No $^{176}Hf/^{177}$ Hf data is available for the region.

No Re-Os isotope data exists for this ridge.

REE signal:

The sampling density of the REE data is thinner than for most of the isotope data.

The LREE/IREE ratios La/Sm and the Ce/Sm show an identical pattern resembling the ones formed by Δ 7/4, 207Pb/204Pb and 208Pb/204Pb. The highest ratios occur at 78°W and a second less intense peak occurs at 82.5°W while the lowest ratios occur between 91°W and 92°W and at 77°W.

The LREE/HREE ratios Ce/Yb and La/Yb show the same pattern as the LREE/IREE ratios. The only difference is that the maximum at 82.5°W is more pronounced than the one at 78°W.

The garnet sensitive IREE/HREE ratio Gd/Yb shows a different pattern. The highest ratios indicating garnet in the source can be found close to the subduction zone (76 – 78°W), while the lowest ratios occur at 82.5°W.

The enrichment tracer CaO/Al2O3 has a regional variation between 0.6 and 0.84. The distribution varies on a small scale (<1°) with high and low values occurring in very close locations. The highest ratios are found at 78 – 78.5°W and the lowest at 82 and 82.5°W. The pattern does not seem systematic.

Figure A 7: Map of the Chile Ridge area with sampled localities with La/Sm data marked by colored circles and oceanic crustal thickness (CRUST1) on a scale from 0 km (black) to 10 km and above (white). Other details according to figure 2.

Galapagos Ridge

Isotope signal:
The $^{207}Pb/^{204}Pb$ and $^{208}Pb/^{204}Pb$ isotopic signals of the Galapagos Ridge show identical patterns varying only slightly in the relative magnitudes of some peaks. The highest ratios ($^{207}Pb/^{204}Pb$=15.56-15.63; $^{208}Pb/^{204}Pb$=38.6-39) of the region occur close to the Galapagos hotspot (89°W – 94°W). The lowest ratios ($^{207}Pb/^{204}Pb$=15-15.5; $^{208}Pb/^{204}Pb$=37.6-38) of the region occur in the part of the ridge

furthest away from the Galapagos hotspot (89°W – 94°W). Minor peaks with intermediate values can be found at 98°W, at 95°W – 96°W and 86°W – 87°W.

The Δ 7/4 and Δ 8/4 values show a very similar pattern when compared to the $^{207}Pb/^{204}Pb$ and $^{208}Pb/^{204}Pb$ isotopic signals. High values extend further west for Δ 8/4 (Δ 8/4: 90 – 98°W; Δ 7/4: 90 – 93°W) than for $^{207}Pb/^{204}Pb$ and $^{208}Pb/^{204}Pb$. The highest values for both Δ 7/4 (5-6.6) and Δ 8/4 (25-36) occur directly north of the Galapagos hotspot and the crustal thickening related to it (91 – 92.5°W). Further lesser maxima for Δ 7/4 and Δ 8/4 can be found at 97-98°W (more pronounced in Δ 8/4; Δ 7/4=4; Δ 8/4=ca. 30) and at 86-87°W (more pronounced in Δ 7/4; Δ 7/4=ca. 5; Δ 8/4=ca. 10-13). The lowest values (more pronounced in Δ 7/4; Δ 7/4 = 0 - -1.5; Δ 8/4 =10 - -12) occur furthest away from the Galapagos hotspot west of 100°W and east of 84°W. Lesser minima occur at 95.5°W, at ca. 88°W and at 85-86°W. At 97°W a minimum only visible in the Δ 7/4 signature coexists with relatively high Δ 8/4.

Untypically the Sr isotope signal does not follow the patterns formed by Δ 7/4, $^{207}Pb/^{204}Pb$ and $^{208}Pb/^{204}Pb$. The $^{87}Sr/^{86}Sr$ ratios of the whole area are uniformly at 0.7024-0.703 with the exception of a few locations near 96°W that show ratios of 0.708 – 0.7083. The high Sr ratios coexist with a minor maximum in $^{207}Pb/^{204}Pb$, $^{208}Pb/^{204}Pb$, Δ 7/4 and Δ 8/4.

$^{143}Nd/^{144}Nd$ mirrors the reversed pattern of $^{207}Pb/^{204}Pb$, $^{208}Pb/^{204}Pb$, Δ 7/4 and Δ 8/4. Deviations from the Pb isotope signal occur at 88-89°W where relatively high $^{207}Pb/^{204}Pb$ ratios coexist with intermediately high $^{143}Nd/^{144}Nd$ as well as low $^{207}Pb/^{204}Pb$ ratios coexist with intermediate $^{143}Nd/^{144}Nd$. On top of that at 85°W intermediate $^{143}Nd/^{144}Nd$ ratios and low $^{207}Pb/^{204}Pb$.

The $^{176}Hf/^{177}Hf$ ratios of the region form a pattern very similar to $^{143}Nd/^{144}Nd$. The major differences are that $^{176}Hf/^{177}Hf$ is consistently very low west of 95.5°W while $^{143}Nd/^{144}Nd$ varies between very low and intermediate ratios, as well as the intermediate $^{176}Hf/^{177}Hf$ ratio at 83°W that coexists with high $^{143}Nd/^{144}Nd$.

Only Re-Os isotope data from very close NW of the Galapagos hotspot is available. The ratios found there are within the "usual" array.

REE signal:
The sampling density of the REE data is thinner than for most of the isotope data.

The LREE/IREE ratios La/Sm and the Ce/Sm show an identical pattern resembling the ones formed by Δ 7/4, $^{207}Pb/^{204}Pb$ and $^{208}Pb/^{204}Pb$. The highest ratios occur at 78°W and a second less intense peak occurs at 82.5°W while the lowest ratios occur between 91°W and 92°W and at 77°W.

The LREE/HREE ratios Ce/Yb and La/Yb show the same pattern as the LREE/IREE ratios.

The garnet sensitive IREE/HREE ratio Gd/Yb shows a slightly different pattern.

The enrichment tracer CaO/Al2O3 has a regional variation between 0.6 and 0.84. The distribution varies on a small scale (<1°) with high and low values occurring in very close locations. The highest ratios are found at 78 – 78.5°W and the lowest at 82 and 82.5°W. The pattern does not seem systematic.
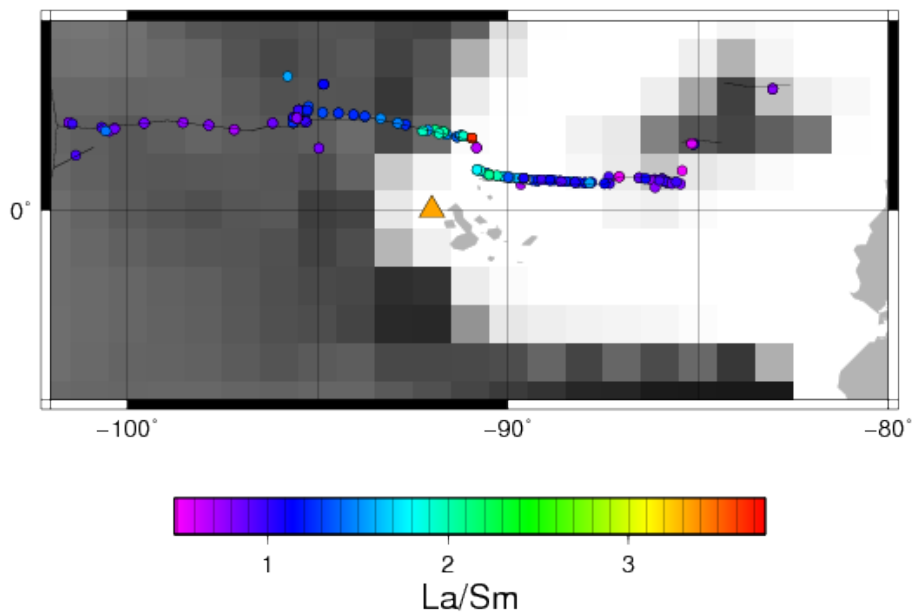

Figure A 8: Map of the Galapagos Ridge area with sampled localities with La/Sm data marked by colored circles and oceanic crustal thickness (CRUST1) on a scale from 0 km (black) to 10 km and above (white). Other details according to figure 2.

Juan de Fuca Ridge

Isotope signal:
The $^{207}Pb/^{204}Pb$ and $^{208}Pb/^{204}Pb$ isotopic signals of the Ridge form very similar patterns along the ridge. Higher values occur mostly in the northern half of the ridge (N of the Cobb hotspot), while low ratios dominate the southern half. Both ratios show the highest values (207Pb/204Pb > 15.5; $^{208}Pb/^{204P}b$ > 38.2) at 40.5-41°N, at 46°N directly north of the Cobb hotspot, at ca. 48°N and at ca. 50°N. The lowest ratios ($^{207}Pb/^{204}Pb$ < 15.45; $^{208}Pb/^{204}Pb$ < 37.7) occur in the southern half of the ridge at ca. 42.5°N and at 44°N. Small scale variation occurs at the scale of ca. 1°. The $^{207}Pb/^{204P}b$ and $^{208}Pb/^{204}Pb$ patterns deviate only at around 48°N where $^{208}Pb/^{204}Pb$ has "anomalous" low values.

The Δ 7/4 values of the region have their relative sub-regional maxima and minima in identical locations as the $^{207}Pb/^{204}Pb$ ratios and there is a clear correlation for most of the ridge. The intensities

118

of them differ most significantly in the northern half of the ridge where the minima are more pronounced in Δ 7/4 (i.e. 47°N, 48°N). Δ 8/4 shows much larger deviation from the patterns of $^{207}Pb/^{204}Pb$ and $^{208}Pb/^{204}Pb$, especially north of the Cobb hotspot. The highest Δ 8/4 values occur in the southernmost part of the ridge at ca. at 40.5-41.5°N. The locations of high values in Δ 7/4, $^{207}Pb/^{204}Pb$ and $^{208}Pb/^{204}Pb$ further north coexist with intermediate to low Δ 8/4 (0 – 15).

The Sr isotope signal of the Juan de Fuca ridge does not reflect the patterns formed by Δ 7/4, $^{207}Pb/^{204}Pb$ and $^{208}Pb/^{204}Pb$. Although in the southern part of the ridge (south of Cobb hotspot) there is some similarity to the Pb isotopic signals with the highest $^{87}Sr/^{86}Sr$ ratios (0.7026 -0.7029) occurring between 40°N and 42°N in identical locations as the maxima in the Pb isotope signatures. An additional intermediate peak occurs near 45°N. Further north only low to intermediate $^{87}Sr/^{86}Sr$ ratios (0.7023 – 0.70255) can be found. These are not at all correlateable with Δ 7/4, $^{207}Pb/^{204}Pb$ and $^{208}Pb/^{204}Pb$ and only roughly with Δ 8/4.

Atypically $^{143}Nd/^{144}Nd$ does not match the reversed pattern of $^{87}Sr/^{86}Sr$. It rather resembles the reversed signature of $^{208}Pb/^{204}Pb$, particularly in the southern half of the ridge.

No $^{176}Hf/^{177}Hf$ data is available for the region.

No Re-Os isotope data exists for this ridge.

REE signal:
The sampling density of the REE data is thinner than for most of the isotope data.

The LREE/IREE ratios La/Sm and the Ce/Sm show a pattern resembling the ones formed by Δ 7/4, $^{207}Pb/^{204}Pb$ and $^{208}Pb/^{204}Pb$ in the northern (north of 48°N) and southern parts of the ridge (south of 45°N). Accordingly the highest ratios occur at at 40.5-41°N and at ca. 50°N, while low ratios predominate between 41°N and 45°N. In the central part of the ridge closer to the Cobb hotspot (45°N – 48°N) the LREE/IREE ratios are low while the isotope ratios are high.

The LREE/HREE ratios Ce/Yb and La/Yb show the same pattern as the LREE/IREE ratios. Slight differences occur in the intensities of the maxima and minima.

The garnet sensitive IREE/HREE ratio Gd/Yb shows a similar pattern, although like the Pb isotopes it also has a maximum in the central part of the ridge closer to the hotspot. Differently from the isotope signal this maximum occurs south of the hotspot (44°N – 45°N) rather than north of it.

The enrichment tracer CaO/Al_2O_3 has a regional variation between 0.58 and 0.92. The pattern formed shows high ratios at 44°N – 45°N and in the northern and southern segments of the near to, but not exactly on the places where other tracers indicate enrichment. Particularly high ratios occur in the

northernmost segment (49 – 51°N) alongside intermediate ratios. The lowest ratios of the region are to be found at ca. 44°N and 48°N. Furthermore low ratios are predominant in most of the ridge except for the northernmost part (N of 48°N).
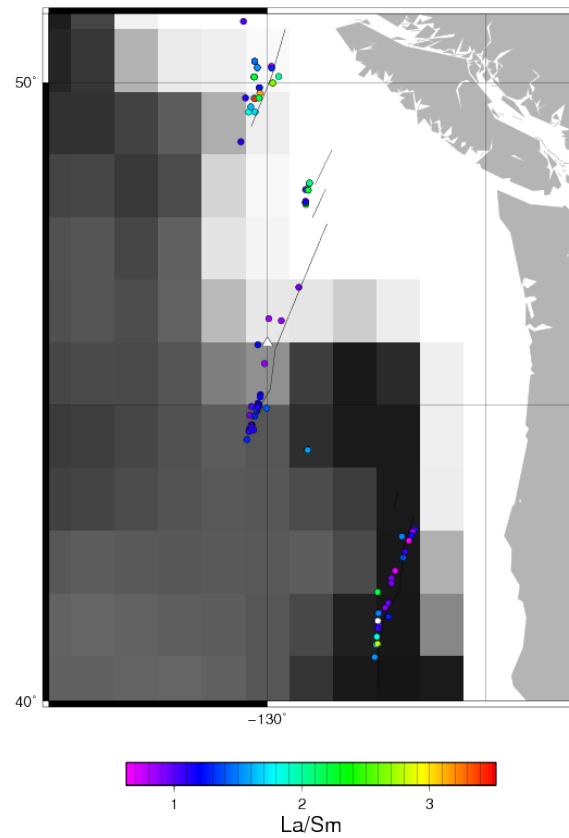

Figure A 9: Map of the Juan de Fuca Ridge area with sampled localities with La/Sm data marked by colored circles and oceanic crustal thickness (CRUST1) on a scale from 0 km (black) to 10 km and above (white). Other details according to figure 2.

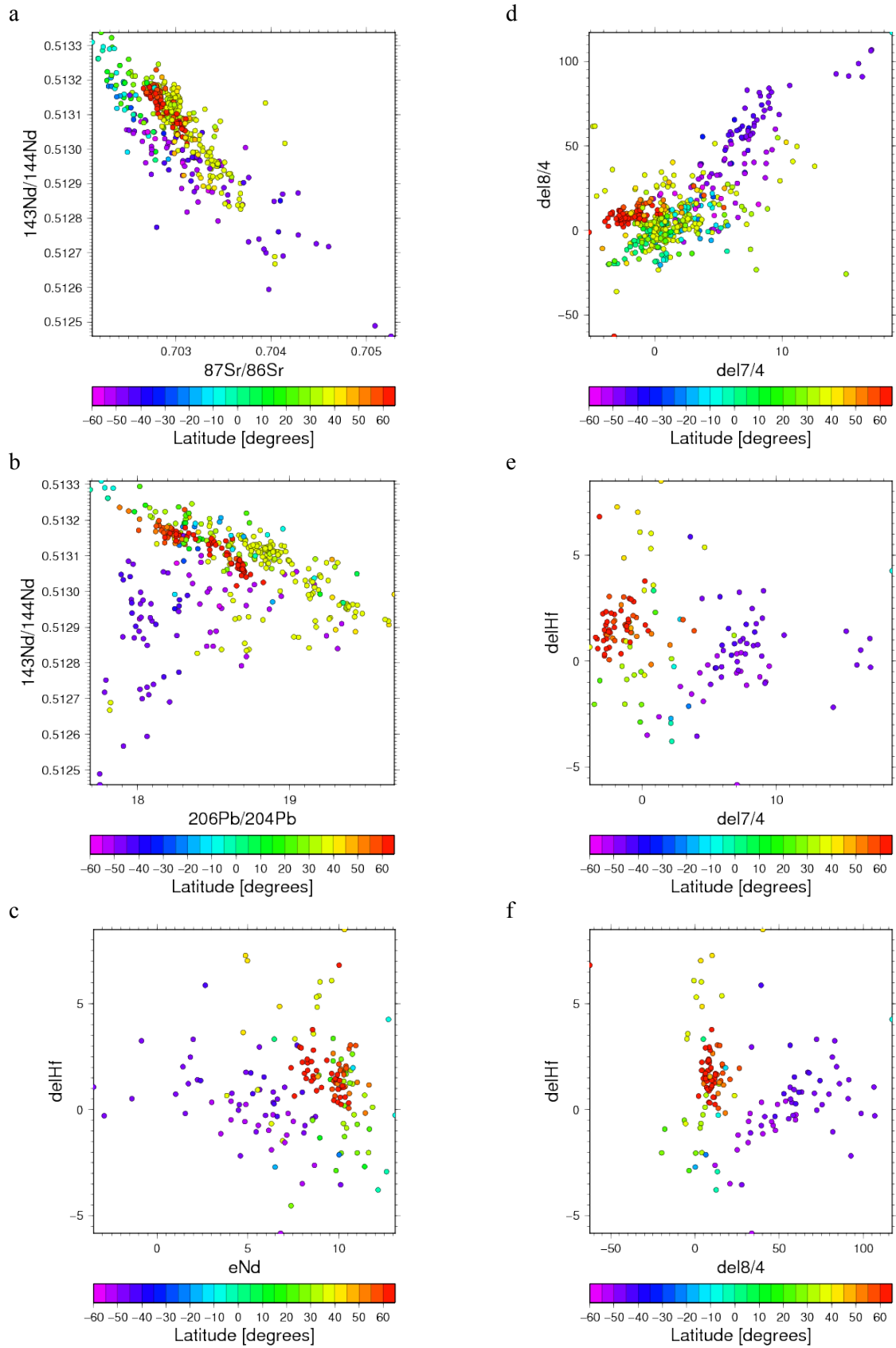**Appendix 2: Selected xy-plots for the Atlantic region, 65°N-60°S**

Figure A 10: (a) $^{143}Nd/^{144}Nd$-$^{87}Sr/^{86}Sr$, (b) $^{143}Nd/^{144}Nd$-$^{206}Pb/^{204P}b$, (c) $\Delta\varepsilon Hf$-εNd, (d) $\Delta 8/4$-$\Delta 7/4$ (e) $\Delta\varepsilon Hf$-$\Delta 8/4$ and (f) $\Delta\varepsilon Hf$- $\Delta 8/4$ plots for MORB of the Mid-Atlantic Ridge south of Iceland.

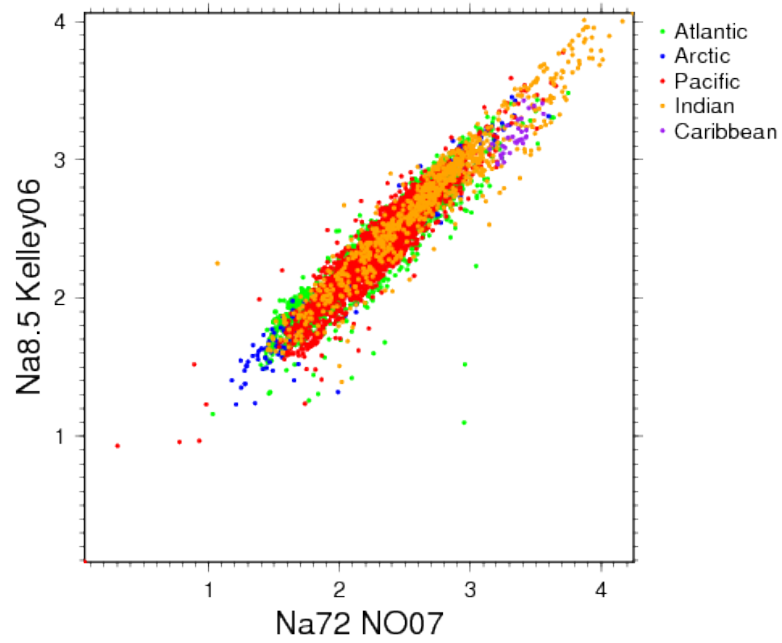# Appendix 3: Comparison of Na72 and Na8.5

Figure A 11: Na72-Na8.5 plot of the global MORB data. Both fractionation correction methods are producing similar and well correlated results. Na8.5 is biased to slightly higher values as it does not completely correct to a primitive mantle composition.